Title

Study of surface enhanced resonant Raman spectroscopy of chromophores on unaggregated plasmonically active nanoparticles / Surface-enhanced Raman study of the interaction of the PEDOT:PSS and P3HT/PCBM components of organic polymer solar cells with p...

Permalink

https://escholarship.org/uc/item/2648d9ps

Author

Stavytska-Barba, Marina Valeriyivna

Publication Date

2012-05-02

Peer reviewed|Thesis/dissertation

UNIVERSITY OF CALIFORNIA, MERCED

I. Study of Surface Enhanced Resonant Raman Spectroscopy of Chromophores on
Unaggregated Plasmonically Active Nanoparticles

II. Surface-Enhanced Raman Study of the Interaction of the PEDOT:PSS and
P3HT/PCBM Components of Organic Polymer Solar Cells
with Plasmonically Active Nanoparticles

A dissertation submitted in partial satisfaction of the
requirements for the degree Doctor of Philosophy

in

Physics and Chemistry

by

Marina Valeriyivna Stavytska-Barba

Committee in charge:

      Professor Jay Sharping, Chair
      Professor Anne Myers Kelley
      Professor Tao Ye
      Professor Jin Zhong Zhang

2012

This dissertation by Marina V. Stavytska-Barba is accepted in its present form
by the Department of Chemistry as satisfying the
dissertation requirement for the degree of Doctor of Philosophy.

Date_____   _____
                                        Anne Myers Kelley, Advisor

Date_____   _____
                                        Jay Sharping, Chair

Date_____   _____
                                        Tao Ye

Date_____   _____
                                        Jin Zhong Zhang

Date_____   _____
                                        Samuel J. Traina, Graduate Division Dean

University of California, Merced

2012

to Nicky

Table of Contents

Project 1: Study of Surface Enhanced Resonant Raman Spectroscopy of Chromophores on Unaggregated Plasmonically Active Nanoparticles

Project 2: Surface-Enhanced Raman Study of the Interaction of the PEDOT:PSS and P3HT/PCBM Components of Organic Polymer Solar Cells with Plasmonically Active Nanoparticles

List of Figures

Project 2: Surface-Enhanced Raman Study of the Interaction of the

PEDOT:PSS and P3HT/PCBM Components of Organic Polymer Solar Cells

List of Tables

Preface

The foundation for this work is surface enhanced Raman spectroscopy fundamentals of which are described in the following chapters. Briefly, in Raman spectroscopy, as well as in the infrared spectroscopy, energy absorbed by a molecule goes into exciting molecular vibrations. Different molecules are likely to have different types of vibrations, resulting in different Raman and infrared spectra. Oftentimes, Raman and infrared spectra are complimentary: depending on types of the molecules, a specific vibration might show up on Raman spectrum or on infrared spectrum. One can use Raman, infrared or both spectra in attempt to identify a substance.

Some molecules might not be very good infrared or Raman scatterers, resulting in very low intensity or unobservable spectra. However, placing these molecules next to metallic surfaces with nanofeatures might improve their Raman spectrum (Surface Enhanced Raman Spectroscopy, SERS) or infrared spectrum (surface enhanced infrared absorption, SEIRA). Great signal enhancements are achieved from incorporation of nano-rough metallic surfaces making these techniques very sensitive.

This SERS sensitivity makes it very useful for detection of miniscule amounts or substances; some examples of current and potential SERS utilization are given below. Detection of 1ppm highly toxic cyanide in water supplies was achieved.[1-4] A route of detection trace amounts of highly explosive TNT (2,4,6-trinitrotoluene) was proposed by taking TNT, which is not a very good Raman scatterer, and then adding

aldehyde to it to make stilbene; stilbene is SERS active, and even trace amounts of stilbene produce SERS spectra.[5, 6] Other possible areas of use for SERS that could be developed can include detection of drugs in abusers' systems, detection of mutated genes or detection of diseases, etc.

In the first part of this work, theory of SERS is developed; the goal of the first project is to study surface enhanced Raman scattering enhancement mechanism using molecules attached to unaggregated silver or gold nanoparticles. In the second part of this work, all of the theory developed in the first project is applied to study organic polymer solar cells in which metallic nanoparticles are incorporated.

References

(1) Kellogg, D. S.; Pemberton, J. E. Effects of Solution Conditions on the Surface-Enhanced Raman Scattering of Cyanide Species at Silver Electrodes. *J. Phys. Chem.* **1987**, *91*, 1120.

(2) Billman J., Kovacs G., Otto A. *Surf. Sci.* **1980**, *92*, 153.

(3) Murray, C.; Bodoff, S. Depolarization Effects in Raman-Scattering from Monolayers on Surfaces - the Classical Microscopic Local Field. *Phys. Rev. Lett.* **1984**, *52*, 2273-2276.

(4) Wagner, G. W.; Yang, Y. -. Rapid Nucleophilic/Oxidative Decontamination of Chemical Warfare Agents. *Industrial And Engineering Chemistry Research* **2002**, *41*, 1925-1928.

(5) McHugh, C. J.; Keir, R.; Graham, D.; Smith, W. E. Selective Functionalisation of

    TNT for Sensitive Detection by SERRS. *Chemical Communications* **2002**, *2002*,

    580-581.

(6) McHugh, C. J.; Kennedy, A. R.; Smith, W. E.; Graham, D. TNT Stilbene

Derivatives as SERRS Active Species. *Analyst* **2007**, *132*, 986-988.

Acknowledgments

I am truly grateful to Professor Anne Myers Kelley who has been my advisor through my years in UC Merced. This dissertation would have not been possible without her. I am not only grateful for the opportunity to be in her group, and the access to the state of the art instruments, but also for being a true mentor. She has been, and still is, one of the greatest instructors in the classroom conveying knowledge effortlessly, in a most organized and gifted fashion. Equally important, she stimulated me to explore the nooks and crannies of my graduated research without giving the answers, but instead teaching me the tools of how to get to the correct sources. For all of the enthusiasm for the subject developed in me and for the encouragement, I am thankful to Professor Kelley. Another thing that I am thankful for is the atmosphere in the lab-- Professor Kelley is the most understanding of others, of their differences and the situations students can find themselves in.

I would also like to thank Weinan Leng who helped me learn how to use the instruments in the lab, for his patience during that process and for becoming a good friend in the meanwhile. I would like to thank Professor David S. Ginger from University of Washington and two members of his group at that time, Abhishek Kulkarni and Michael Salvador, for the collaboration and preparation of samples containing silver nanoprisms. Additionally, I would like to thank Mike Dunlap for his assistance in obtaining TEM images of the metal nanoparticles at the UC Merced Imaging and Microscopy Facility. I acknowledge the Donors of the American Chemical Society Petroleum Research Fund for their support of this research.

Vita

ACADEMIC HISTORY

University of California, Merced, Merced, CA.	*2006-present*
Graduate program: Physics and Chemistry.	
Working towards Doctor of Philosophy.	
Advisor: Prof. Anne Myers Kelley.	
California State University Stanislaus, Turlock, CA.	*2004- 2006*
Bachelor of Science in Chemistry, Magna Cum Laude.	
Merced College, Merced, CA.	*2001- 2004*
Associate of Science in Chemistry, honors graduate.	
East Ukrainian National University, Lugansk, Ukraine.	*2000- 2009*
Bachelor in Applied Mathematics.	

WORK EXPERIENCE

Adjunct Instructor, Columbia College.	*2012- present*
Adjunct Instructor, Merced College.	*2011- present*
Teaching Fellow, UC Merced.	*2008- 2011*
Graduate Student Researcher, UC Merced.	*2007-2011*
Teaching Assistant, UC Merced.	*2006- 2008*
Instructional Student Assistant in Unit 11, CSU Stanislaus.	*2004- 2006*
Tutor, Tutoring Center, Merced College.	*2001- 2004*

PUBLICATIONS AND PRESENTATIONS

- Stavytska-Barba, M.; Salvador, M.; Kulkarni, A.; Ginger, D. and Kelley, A. M., *J. Phys. Chem. C*, **2011,** 115, 20788.
- Stavytska-Barba, M.; Kelley, A. M. presentation at *58th annual Western Spectroscopy Conference*, January 19-21, 2011, Asilomar, CA.
- Stavytska-Barba, M.; Kelley, A. M., presentation at *CLEO/QELS*, May 16, 2010, San Jose, CA.
- Stavytska-Barba, M.; Kelley, A. M., *J. Phys. Chem. C, ***2010***, 114*, 6822-6830.
- Stavytska-Barba, M.; Kelley, A. M., presentation at *239th ACS National Meeting*, March 21-25, 2010, San Francisco, CA.
- Stavytska-Barba, M.; Kelley, A. M., presentation at *57th annual Western Spectroscopy Conference*, February 3-5, 2010, Asilomar, CA.

HONORS AND AWARDS

- ✓ Outsdanding Adjunct Faculty of the 2011-2012 Year in Merced College.
- ✓ Magna Cum Laude honors graduate from CSU Stanislaus.
- ✓ 2005 Undergaduate Award in Analytical Chemistry, American Chemical Society.
- ✓ Dean's List, CSU Stanislaus, Fall 2004.
- ✓ The Outstanding Student for the 2003-2004 Year in Chemistry, Merced College.
- ✓ Honors List in Merced College.

Abstract

The first part of this manuscript deals with fundamental theories behind surface enhanced resonant Raman spectroscopy (SERRS). Optical absorption, resonant Raman and surface enhanced Raman spectra of chromophores bound to small isolated spherical gold or silver nanoparticles in colloidal solutions are collected, presented and SERRS excitation profiles are constructed. The goal of this project is to devise a chromophore-nanoparticle system such that chromophores bind to the nanoparticles but do not aggregate them. The spectra of such a system are analyzed to give clues about two enhancement mechanisms of SERRS-- a chemical enhancement mechanism and an electromagnetic one.

In the second part of this manuscript, influences of metal nanoparticles on components of an organic polymer solar cell based on poly(3-hexylthiophene)/ (6,6)-phenyl-C_{61}-butyric acid methyl ester active layer and poly(3,4-ethylenedioxy-thiophene):polystyrene-sulfonate supporting layer are studied. Different kinds of metal nanoparticles, such as silver and gold nanospheres, silver and gold nano-sputtered films, and silver nanoprisms, are incorporated in different geometries around the organic polymer layers and resulting extinction and surface enhanced Raman spectra are studied to give clues of possible solar efficiency enhancement mechanisms achieved by the nanoparticle incorporation.

Project 1:

Study of Surface Enhanced Resonant Raman

Spectroscopy of Chromophores on Unaggregated

Plasmonically Active Nanoparticles

1 Theory and Background

1.1 Linear Absorption and Fluorescence

In linear absorption, ultraviolet and visible (UV-Vis) spectroscopy, and in linear emission, fluorescence spectroscopy, electronic transitions between the different vibrational energy levels are possible for each electronic state (Figure 1-1).

UV-Vis Absorbance   **Fluorescence**
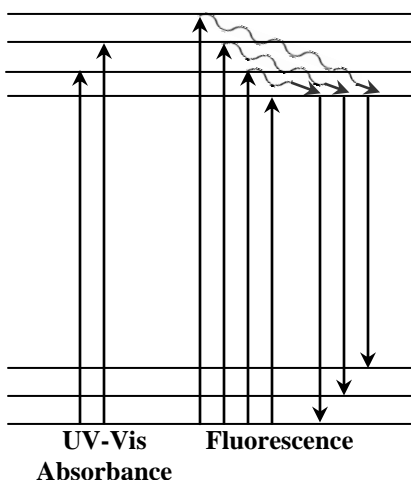
Figure 1-1. Jablonski diagram of UV-Vis and Fluorescence spectroscopies.

Vibronic analysis of linear absorption and emission spectra can be used as the most direct way to determine the structural changes that happen during the excitation. However, vibronic structure linewidths can be very broadened, obscured and not distinguishable in linear absorption and emission spectra because:

- often excited state lifetimes are so short that no oscillations in frequency are observed, which is termed homogeneous broadening; thus the vibronic structure would not be seen;

- the spectrum can be a combination of slightly different spectra resulting from either slightly different conformations of the studied molecule or, in the condensed phase, from interactions of the molecule of interest with solvents, termed inhomogeneous broadening; overlaps of the vibronic structures can make them indistinguishable;

- at the same time the molecule can be oscillating along many vibrational modes in the spectral region of interest, termed spectral congestion, obscuring the vibronic structure.

In the cases when vibrational fine structure is not well resolved in linear absorption and emission electronic spectra, different spectroscopic techniques need to be employed to study molecular vibrational structures.

1.2 Infrared Spectroscopy and Raman Spectroscopy
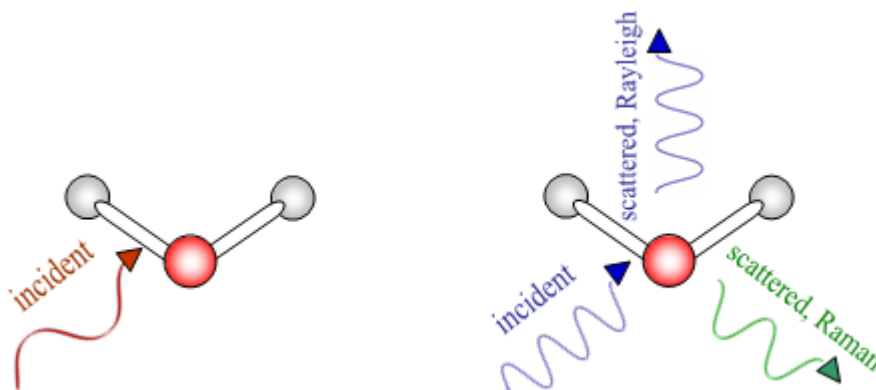
Figure 1-2. A. In infrared spectroscopy light is absorbed by a molecule and is later dissipated as heat through collisions. B. Raman spectroscopy can be described as a collision between a photon and the molecule with the incoming light being scattered by a molecule.
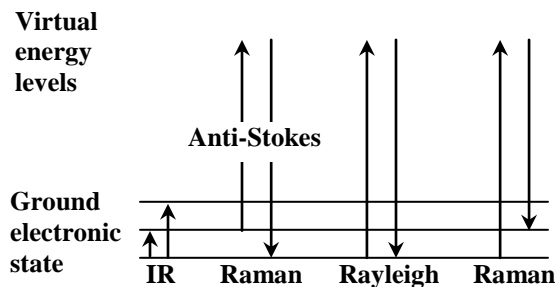
Figure 1-3. Jablonski diagram of IR, Raman and Rayleigh spectroscopies.

When electromagnetic radiation is incident on a molecule, the light can be reflected, absorbed/emitted and scattered. In infrared (IR) spectroscopy, a molecule absorbs energy needed for a vibrational transition, and the energy is later dissipated as heat through collisions (Figure 1-2 A and Figure 1-3). Raman spectroscopy is also a vibrational type of spectroscopy, that is energy acquired by a molecule can go into exciting a molecular vibration; however, the incoming light is scattered with phase memory (Figure 1-2 B and Figure 1-3), not absorbed as in IR spectroscopy. Therefore, Raman spectroscopy is a two photon process and can be described as a collision between a photon and the molecule. IR and Raman spectroscopies have different selection rules, and one often can see different modes in Raman versus IR spectra. Scattered photons can be either of the same energy as the incident radiation (Rayleigh elastic scattering, a predominant pathway), of higher energy (Anti-Stokes Raman inelastic scattering) or of lower energy (Stokes Raman inelastic scattering) (Figure 1-3). The difference in incident light and scattered light energies, which is termed Raman shift, corresponds to the vibrational frequency of a molecule that is being irradiated. Raman vibrational spectra are usually presented as Stokes intensity versus Raman shift: intensities of the Raman lines contain information about the

polarizabilities of molecules and Raman shifts of these lines contain information about the frequencies of the molecular vibrations.

From Figure 1-3 one can see that both IR and Raman spectroscopies can be used to study ground state vibrational structures; in addition, the resonance Raman type of Raman spectroscopy can be used to probe excited state vibrational structure. In Resonance Raman spectroscopy the excitation energy is chosen so that it intercepts the excited electronic state (Figure 1-4). In cases where linear absorption and emission are diffuse instead of being resolved and when excited states are short-lived, which results in weak fluorescence, relatively simple to conduct resonance Raman spectroscopy[1, 2, 3, 4] can be used.
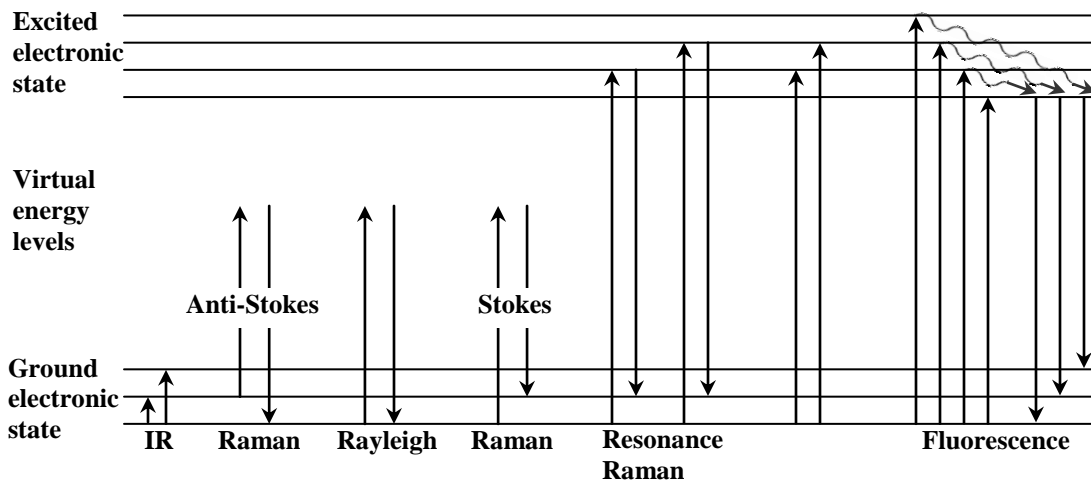
Figure 1-4. Jablonski diagram comparing IR, Raman, Rayleigh, Resonance Raman, UV-Vis and Fluorescence spectroscopies.

1.3 Theory of Raman, Resonant Raman and Absorption Spectroscopies:

1.3.1 Classical Treatment of Raman Spectroscopy
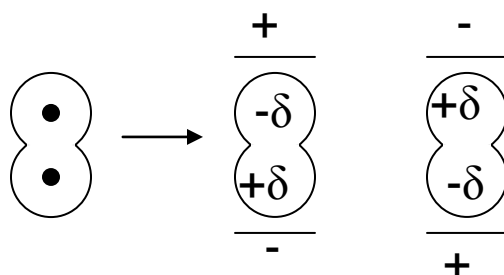
Figure 1-5. Induced dipole moment on the molecule with application of the electric field.

When a molecule, which is much smaller than a wavelength of light, is placed in an electric field (laser beam) with a fluctuating electric field strength (Figure 1-5), the electric field creates charge separation and generates an induced dipole moment on the molecule[6]:

$$\mu = \mu_0 + \alpha E \qquad (1\text{-}1)$$

where μ_0 is the equilibrium value of the dipole moment, also called permanent dipole moment; α is a Raman polarizability or a relative tendency of a charge distribution, like the electron cloud of an atom or a molecule, to be distorted from its normal shape by an external electric field. α is a second-rank tensor and is a 3×3 matrix in a Cartesian coordinates. Therefore, equation (1-1) should be rewritten:

$$
\begin{pmatrix} \mu_x \\ \mu_y \\ \mu_z \end{pmatrix} = \mu_0 + \begin{pmatrix} \alpha_{xx} & \alpha_{xy} & \alpha_{xz} \\ \alpha_{yx} & \alpha_{yy} & \alpha_{yz} \\ \alpha_{zx} & \alpha_{zy} & \alpha_{zz} \end{pmatrix} \begin{pmatrix} E_x \\ E_y \\ E_z \end{pmatrix}
$$

(1-2)

For example, α_{xz} is polarizability in the x direction induced by an electric field in the z direction. Polarizability tensor can be approximated by a Taylor series expansion:

$$
\alpha = \alpha_0 + \left(\frac{\partial \alpha}{\partial x} \right)_0 x + \frac{1}{2} \left(\frac{\partial^2 \alpha}{\partial x^2} \right)_0 x^2 + \frac{1}{6} \left(\frac{\partial^3 \alpha}{\partial x^3} \right)_0 x^3 + ...
$$

(1-3)

Where α_0 is polarizability at equilibrium, and $\left(\dfrac{\partial \alpha}{\partial x} \right)_0$ is a change in polarizability along vibrational coordinates due to bending or stretching/compression.

For a transition to be possible, a transition dipole matrix element must not equal zero:

$$
\langle f | \hat{\mu} | i \rangle \neq 0
$$

(1-4)

Incorporating equations (1-1) and (1-3) into equation (1-4):

$$
\langle f | \hat{\mu} | i \rangle = \langle f | \mu_0 + \alpha E | i \rangle =
$$

$$
= \left\langle f \left| \mu_0 + \left[\alpha_0 + \left(\frac{\partial \alpha}{\partial x} \right)_0 x + \frac{1}{2} \left(\frac{\partial^2 \alpha}{\partial x^2} \right)_0 x^2 + \frac{1}{6} \left(\frac{\partial^3 \alpha}{\partial x^3} \right)_0 x^3 + ... \right] E \right| i \right\rangle \approx
$$

(1-5)

$$
\approx \left\langle f \left| \mu_0 + \left[\alpha_0 + \left(\frac{\partial \alpha}{\partial x} \right)_0 x \right] E \right| i \right\rangle = \langle f | \mu_0 | i \rangle + \langle f | \alpha_0 E | i \rangle + \left\langle f \left| \left(\frac{\partial \alpha}{\partial x} \right)_0 x E \right| i \right\rangle =
$$

$$
= 0 + 0 + \left(\frac{\partial \alpha}{\partial x} \right)_0 E \langle f | x | i \rangle = \left(\frac{\partial \alpha}{\partial x} \right)_0 E \langle f | x | i \rangle
$$

Therefore $\left(\dfrac{\partial \alpha}{\partial x} \right)_0 \neq 0$ for a transition to occur; in other words, **only those vibrations associated with polarizability change of the molecule during the vibration are**

Raman active (where for infrared vibrational spectroscopy the requirement is that the dipole moment of the molecule must change). Also since transition means that final and initial states are different or $\langle f | i \rangle = 0$, then necessarily $\langle f | x | i \rangle \neq 0$. From the last statement selection rules of $\Delta v = \pm 1$ for a harmonic oscillator and $\Delta v = \pm 1, \pm 2, \pm 3, \pm 4, ...$ for an anharmonic oscillator can be derived[7]. Intensity of a Raman transition is proportional to the $\left| \frac{\partial \alpha}{\partial x} \right|^2$.

1.3.2 Sum-Over-States Picture of Raman, Resonant Raman and Absorption Spectroscopies

1.3.2.1 Raman Spectroscopy

Sum-over-states picture of spectroscopy can be used to model frequency domain spectra. In general, a cross section of a single molecule with randomly-averaged orientation corresponds to an effective area in which a molecule will interact with every involved photon. For a linear optical process, the cross section relates radiated power to incident photon flux. The total radiated power from a Raman transition from state $|I>$ to state $|F>$, $P_{I \to F}$ (photons·sec^{-1}), integrated over all polarizations in all directions (over the solid angle 4π) and assuming randomly oriented scatterers, is[8]:

$$P_{I \to F} = I \sigma_{I \to F}(w_L) \tag{1-7}$$

where I is the incident photon flux (photons·area^{-1}·sec^{-1}); $\sigma_{I \to F}(w_L)$ is the integrated Raman cross section (area) for an isolated molecule as a function of the excitation frequency, w_L, which includes scattering in all directions. Thus, a Raman cross section provides a measure of the efficiency or magnitude of the optical process. [9] Integrated Raman cross section can be expressed in terms of Raman polarizability[8]:

$$\sigma_{I \to F}(w_L) = \frac{8\pi w_S^3 w_L}{9c^4} \sum_{\rho\lambda} \left| \left(\alpha_{\rho\lambda} \right)_{I \to F} \right|^2 \qquad \textbf{(1-8)}$$

where ρ and λ are any two of the x, y, or z directions in the molecule fixed coordinate system; w_S is the scattered photon energy; $\left(\alpha_{\rho\lambda} \right)_{I \to F}$ is an element of the transition polarizability tensor caused by $I \to V \to F$ transition. If the total radiated power from a Raman transition and the incident photon flux are defined in terms of energy, not photons, then $w_S^3 w_L$ can be written as w_S^4.[10]

With the use of the second order time-dependent perturbation theory, the Kramers-Heisenberg-Dirac (KHD) sum-over-states equation for polarizability can be derived. Initially, the equation was derived by analogy to the classical dispersion theory by Kramers and Heisenbers[11]; Dirac derived it later with the use of second-order perturbation theory[12]:

$$\left(\alpha_{\rho\lambda} \right)_{I \to F} = \frac{1}{\hbar} \sum_V \left[\frac{\langle F | \mu_\lambda | V \rangle \langle V | \mu_\rho | I \rangle}{w_{VF} + w_L} + \frac{\langle F | \mu_\lambda | V \rangle \langle V | \mu_\lambda | I \rangle}{w_{VI} - w_L} \right] \qquad \textbf{(1-9)}$$

Before applied energy interacts with a molecule, the molecule starts in the state $|I>$, a vibrational level in the ground electronic state. Incident electromagnetic radiation advances the molecule to the state $|V>$, an entire manifold or a superposition of all excited states. Incident photon energy does not have to exactly correspond to the

intermediate state energies because the system exists in the intermediate state for a finite time. Since no measurement of the system is made during this step, contributions from all intermediate states have to be summed. Later spontaneous scattering returns the molecule to the state |F >, a different vibrational level in the ground electronic state. μ_ρ is a vector component of the transition dipole operator.

Equation (1-9) does not account for finite lifetimes and, therefore, energy widths of the states, instead of E_V, writing $E_V - i\hbar\Gamma_V$ would be more correct, where $i\Gamma_V$ is the damping constant responsible for the lifetime broadening (Γ_V is the homogeneous band width of the Vth state). Equation (1-9) becomes:

$$\left(\alpha_{\rho\lambda}\right)_{I\to F} = \frac{1}{\hbar}\sum_V\left[\frac{\langle F|\mu_\lambda|V\rangle\langle V|\mu_\rho|I\rangle}{w_{VF} + w_L - i\Gamma_V} + \frac{\langle F|\mu_\lambda|V\rangle\langle V|\mu_\lambda|I\rangle}{w_{VI} - w_L - i\Gamma_V}\right] \qquad \textit{(1-10)}$$

In ordinary Raman scattering, the incident radiation frequency is chosen to be much smaller than the frequency required for the transition from a ground electronic state to an excited electronic state (see Figure 1-3). In Resonant Raman scattering, the incident radiation approaches the frequency required for the transition from the ground electronic state to the excited one, which makes the denominator in the second term of the equation (1-10) very small, which in turn makes the second term, called the "resonant" term, very large in comparison to the first, "nonresonant", term.

1.3.2.2 Resonant Raman Spectroscopy

Resonant Raman scattering happens when the excitation energy is chosen so that it intercepts the excited electronic state. If we would like to choose the incident

energy to be close to an electronic transition, then we can judge that from the optical absorption spectra. Therefore, on resonance, a specific electronic state makes the dominant contribution to the resonant Raman polarizability and the vibrational levels of this transition dominate the sum. Since resonant excited state vibrational levels are dominant, the dynamics of the resonant excited state can be probed.[2, 13, 14] On resonance, intensities of the Raman lines contain information about the excited state molecules[15] and Raman shifts of these lines contain information about the frequencies of the ground state vibrational modes.

To simplify integrated Raman cross section and polarizability expressions, following approximations are usually made while talking about Resonance Raman spectroscopy: dipole approximation, Born-Oppenheimer approximation, Condon approximation, single state approximation and homogeneous linewidth approximation.

Dipole Approximation

The size of a molecule is much smaller than the wavelength of light; therefore, interaction of a molecule with electromagnetic radiation can be described by an electric dipole, two opposite charges oscillating.

Born-Oppenheimer Approximation

Compared to the fast moving electrons, the heavy nuclei are considered stationary in the Born-Oppenheimer approximation, so that nuclei and electron coordinates are separable.[16] The electronic transition probability can be computed at a stationary nuclear position; the total wavefunction can be presented as a product of nuclear and electronic wavefunctions; electronic wavefunctions can be solved at

different nuclear configurations; vibronic wavefunctions can be separated into a product of vibrational and electronic states. The matrix elements in equation 2-9 become, for example:

$$\langle V|\mu_\rho|F\rangle = \langle v|\langle e|\mu_\rho|g\rangle|f\rangle = \langle v|M_\rho(Q)|f\rangle \qquad \textbf{\textit{(1-11)}}$$

where $|e>$ is the excited and $|g>$ is the ground electronic states, and $|v>$ and $|f>$ are the vibrational levels in excited and ground electronic states correspondingly; $M_\rho(Q)$ is the electronic transition length matrix element, and it is a function of Q, the multi-dimensional nuclear coordinate (since the electronic states parametrically depend on the nuclear coordinates).

Condon Approximation

To begin with, electron transition moment, $M_\rho(Q)$, can be expanded as a Taylor series around the Q_0, the ground state equilibrium nuclear geometry:

$$M_\rho(Q) = M_\rho(Q_0) + \left(\frac{\partial M_\rho}{\partial Q}\right)_0 Q + \dots \qquad \textbf{\textit{(1-12)}}$$

The Condon approximation assumes that the magnitude of the transition length at Q_0, the ground-state equilibrium geometry, is much larger than the change of transition moment over the range of Q, therefore, $M_\rho(Q) \approx M_\rho(Q_0)$.[17]
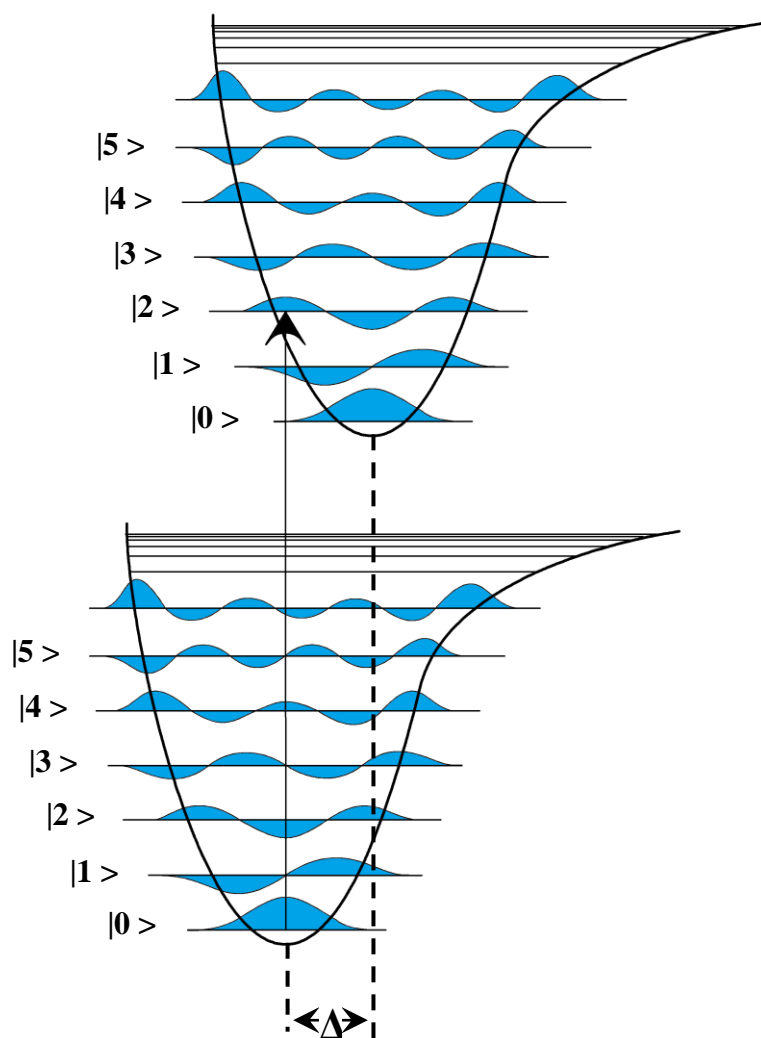
Figure 1-6. Morse potentials that demonstrate Franck–Condon principle. |0>→|2 > transition is favored in the potential wells shown here. Δ is the displacement between the potential wells.

Single State Approximation

Since laser frequency approaches the electronic transition frequency, the second, "resonant", term in the sum over states in the equation (1-10) is dominant and the first, "nonresonant", term can be dropped.[18] A coordinate system can be chosen so that the transition moment is nonzero only along one of the axes, then, in the equation (1-10), the sum over the ρ and λ can be eradicated.

Homogeneous Linewidth Approximation

Γ can also be assumed to be the same for all vibrational levels of the excited electronic state and represents the total homogeneous linewidth from lifetime contributions and dephasing.

Separable Harmonic System Approximation

Evaluation of multidimensional Frank-Condon factors, such as $<i|v>$ or vertical transitions in Figure 1-6, can be quite complicated. Multidimensional separable harmonic approximation assumes that both ground-state and excited-state potential surfaces are harmonic, and their only difference is in equilibrium positions (Figure 1-7). Potential wells are displaced by an amount Δ and have a characteristic frequency. Potential surfaces' vibrational frequencies and normal coordinates are the same. This way, N vibrational modes are represented by a compilation of N independent harmonic oscillator pairs; and multidimensional Frank-Condon factors become products of one-dimensional overlaps:

$$\langle v|i \rangle = \prod_{j=1}^{N} \langle v_j | i_j \rangle \qquad \textit{(1-13)}$$
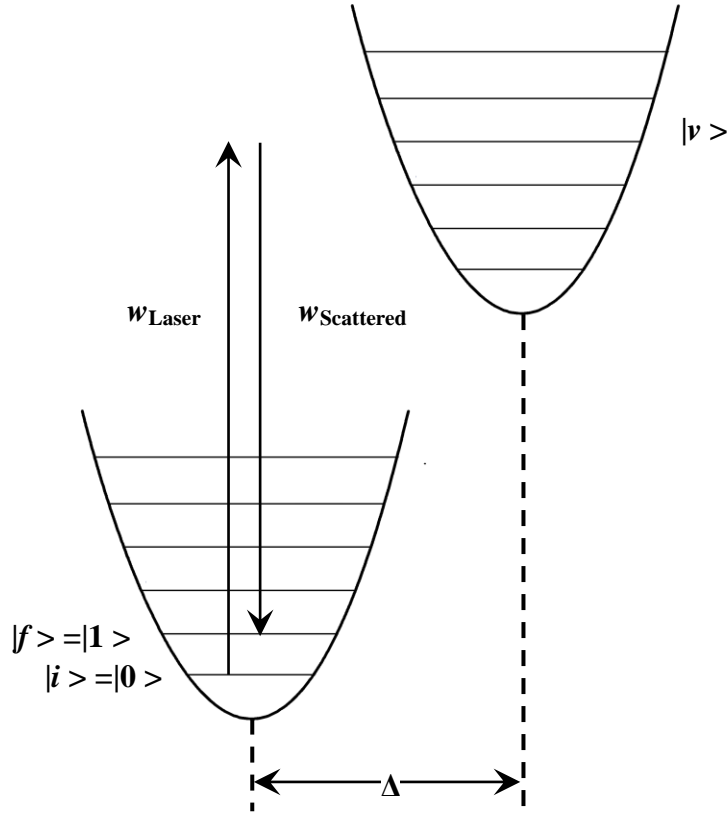
Figure 1-7. Separable harmonic system representation of resonant Raman

scattering.

With the use of approximations described above, resonant Raman polarizability expression is simplified to:

$$\alpha_{i\to f} = \frac{1}{\hbar}M^2\sum_v \frac{\langle f|v\rangle\langle v|i\rangle}{w_{vi} - w_L - i\Gamma}$$

(1-14)

And an integrated Raman cross section becomes:

$$\sigma_{i\to f} = \frac{8\pi w_S^3 w_L M^4}{9\hbar^2 c^4}\left|\sum_v \frac{\langle f|v\rangle\langle v|i\rangle}{w_{vi} - w_L - i\Gamma}\right|^2$$

(1-15)

1.3.2.3 Absorption Spectroscopy

At the same level of theory and approximation, optical absorption cross section is given by:[19]

$$\sigma_A = \frac{4\pi^2 w_L M^2}{3\hbar^2 cn} \sum_v \frac{\Gamma}{\pi} \frac{\left|\langle v|i\rangle\right|^2}{\left(w_{vi} - w_L\right)^2 + \Gamma^2} \qquad (1\text{-}16)$$

here, n is the refractive index of the solution. Molar absorptivity, ε, is related to σ by:

$$\sigma = 2.303 \times 10^{19} \frac{\varepsilon}{N_A} \qquad (1\text{-}17)$$

where N_A is the Avogadro's number.

If we multiply the numerator and the denominator of integrated Raman cross section equation (1-15) by $w_{vi} - w_L - i\Gamma$, then we would get:

$$\sigma_{i \to f} = \frac{8\pi w_S^3 w_L M^4}{9\hbar^2 c^4} \left| \sum_v \frac{\langle f|v\rangle\langle v|i\rangle}{\left(w_{vi} - w_L\right)^2 + \Gamma^2} \cdot \left(w_{vi} - w_L + i\Gamma\right) \right|^2 \qquad (1\text{-}18)$$

Comparing equations (1-16), (1-17) and (1-18), the real part of the resonance Raman cross section becomes smaller with the increase of the homogeneous linewidth, but absorption spectrum broadens with the increase of the homogeneous linewidth, which contributes to absorption spectrum being diffuse. Homogeneous linewidth can be calculated from absolute cross sections obtained by resonance Raman spectroscopy. Later, homogeneous linewidth, as well excited-state parameters obtained from fitting Raman intensities, can be used for fitting the absorption to the experimental absorption.

1.3.3 Time-Dependent Picture of Resonant Raman and Absorption Spectroscopies

1.3.3.1 Resonant Raman Spectroscopy

Calculations for large molecules in the frequency domain picture based on sum-over-states route are very cumbersome, if not impossible: only transitions to one electronic state are assumed; and a large number of vibrational levels need to be used for calculation of the Raman cross section in frequency domain expression.[20] Time domain form can be much easier to evaluate for larger molecules and/or for more than one resonant electronic state, for thermal distribution of initial states, for non-Condon effect, and for more complicated than harmonic oscillator potential energy surfaces.[14, 21] Additionally, in a time dependent picture it is much easier to visualize the resonance Raman process than in the frequency domain picture. The time domain result can be later Fourier transformed into the frequency domain.

The time-dependent formalism can be derived from scratch using the second-order time-dependent perturbation theory.[22] Alternatively, a more simplified derivation method starts from sum-over-states equation. In particular if we want to derive a time domain equation for a resonant Raman scattering cross section with the same levels of approximations that we have used for equation (1-15) , than we can start with modifications to the (1-15) equation directly. The denominator of the modulus squared (Raman amplitude) in equation (1-15) can be written as a half-Fourier transform:[2, 14, 21]

$$\sigma_{i \to f} = \frac{8\pi w_S^3 w_L M^4}{9\hbar^2 c^4} \left| \frac{i}{\hbar} \int_0^\infty \sum_v \langle f|v \rangle \langle v|i \rangle e^{-i(w_{vi}-w_L-i\Gamma)t} \, dt \right|^2 \qquad \textbf{\textit{(1-19)}}$$

Recalling that $w_{vi} = w_v - w_i$,

$$\sigma_{i \to f} = \frac{8\pi w_S^3 w_L M^4}{9\hbar^2 c^4} \left| \frac{i}{\hbar} \int_0^\infty \sum_v \langle f|v \rangle \langle v|i \rangle e^{i(w_L+w_i)t-\Gamma t} e^{-iw_v t} \, dt \right|^2 \qquad \textbf{\textit{(1-20)}}$$

Considering the excited state vibrational motion Hamiltonian, $\langle v|e^{-iw_v t} = \langle v|e^{-iHt/\hbar}$, we

get:

$$\sigma_{i \to f} = \frac{8\pi w_S^3 w_L M^4}{9\hbar^2 c^4} \left| \frac{i}{\hbar} \int_0^\infty \sum_v \langle f|v \rangle \langle v|e^{-iw_v t}|i \rangle e^{i(w_L+w_i)t-\Gamma t} \, dt \right|^2 \qquad \textbf{\textit{(1-21)}}$$

Now if we consider $e^{-iHt/\hbar}$ propagator -or- $e^{-iHt/\hbar}|i \rangle = |i(t) \rangle$, and use the closure

relation, $\sum_v |v \rangle \langle v| = 1$, the Raman cross section becomes:

$$\sigma_{i \to f} = \frac{8\pi w_S^3 w_L M^4}{9\hbar^6 c^4} \left| \int_0^\infty \langle f|i(t) \rangle e^{i(w_L+w_i)t-\Gamma t} \, dt \right|^2 \qquad \textbf{\textit{(1-22)}}$$

In the frequency domain equation there was no effective way to incorporate more than homogeneous broadening into the damping constant, Γ. Homogeneous broadening arises from mechanisms that broaden the spectrum of a single molecule, such as lifetime broadening, where inhomogeneous broadening arises from ensemble effects. Inhomogeneous broadening is particularly significant in the condensed phase where molecules may be starting out in different quantum states due to somewhat different environments or due to thermal excitation of low-lying vibrational levels.[23] Therefore, in addition to the described above modifications of Raman cross section, it is important to redefine the damping constant to $g(t)$, a function that encompasses

both: the lifetime decay and solvent-induced pure dephasing only (inhomogeneous broadening is still not included here).[1, 24] Subsequently, an equation for resonance Raman cross section becomes:

$$\sigma_{i \to f} = \frac{8\pi w_S^3 w_L M^4}{9\hbar^6 c^4} \left| \int_0^\infty \langle f | i(t) \rangle e^{i(w_L + w_i)t - g(t)} dt \right|^2 \qquad \text{(1-23)}$$
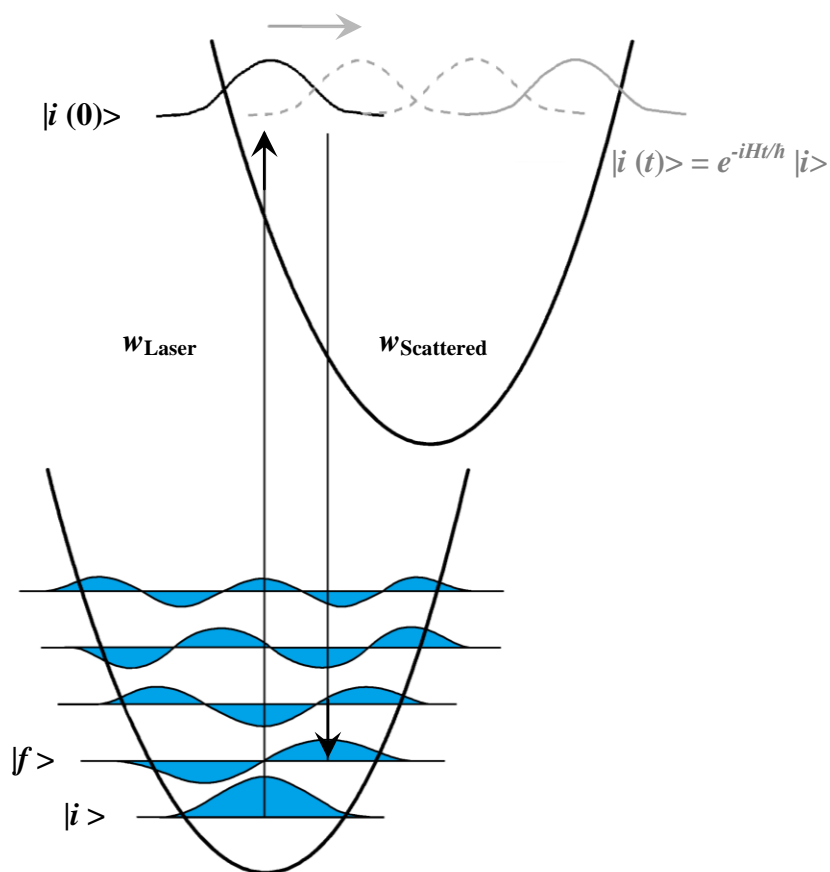
Figure 1-8. Time-dependent picture of resonant Raman scattering and absorption; in gray: wavepacket dynamics along the excited state potential surface.

Equation (1-23) can be schematically interpreted by the Figure 1-8, which gives a better and more intuitive insight into the processes involved in resonant Raman scattering than the interpretation of the frequency domain resonance Raman cross section expression. However, both cross section equations, in the time domain and in the frequency domain, are mathematically equivalent and correspond to the same process, under the same conditions and at the same level of approximation. Even though time dependence appears in the equation (1-23), it is important to note that this equation does not depict a time-resolved resonant Raman experiment, instead, the (1-23) equation describes a steady-state scattering with electromagnetic radiation irradiating the molecules for a long time.

Looking at equation (1-23) and Figure 1-8, the system starts out in a vibrational eigenstate $|i>$ of the ground electronic level. At time zero, electronic transition moment interacts with the irradiating electromagnetic field, and a vertical transition to the excited electronic surface takes place. At this point the vibrational state $|i>$ at the excited electronic surface is under the influence of the excited state Hamiltonian, and it is not an eigenstate of this Hamiltonian. Therefore, the wavefunction $|i>$ starts propagating with time. The Raman cross section is determined from the overlap of this propagating wavepacket $|i(t)>$ and the final state $|f>$. At time zero this overlap is zero, then the overlap increases while the wavepacket moves and overlaps with the lobe of the final state, until it moves away from the lobe and there is no overlap again, then on the return trip the propagating wavefunction starts to overlap with the final state again, and so on. Square of the half-Fourier transform of the overlap damped by the $g(t)$ is proportional to the Raman cross

section; and the resulting spectrum of Raman cross section versus excitation frequency is an excitation profile, reflecting dependence of each Raman transition on incident laser frequency. Raman intensities are governed by the <f |i (t)> overlap: if ground and excited surfaces are not very displaced, then i (t)> will never move far enough to achieve good <f |i (t)> overlap, and then the intensity would be low.[23]

1.3.3.2 Absorption Spectroscopy

To get to the time-dependent expression for the absorption cross section, the denominator in equation (1-16) is replaced by a full Fourier transform and similar manipulations are performed to get to[25]:

$$\sigma_A = \frac{4\pi w_L M^2}{6\hbar^2 cn} \int_{-\infty}^{\infty} \langle i | i(t) \rangle e^{i(w_L + w_i)t - g(t)} dt \qquad (1\text{-}24)$$

Equation (1-24) for absorption cross section in the time dependent picture can also be very nicely visualized with Figure 1-8. Electronic transition moment interacts with the irradiating electromagnetic field causing a vertical transition to the excited electronic surface. Now, vibrational state $|i>$ is at the excited electronic surface and is under the influence of the excited state Hamiltonian. The wavefunction $|i>$ starts propagating with time. The absorption cross section is determined from the overlap of the propagating wavepacket |i (t)> and itself at time zero, the initial state $|i>$. At time zero this overlap is unity, then the overlap decreases to zero while the wavepacket moves away, then on the return trip the propagating wavefunction starts to overlap with the final state again. Square of the Fourier transform of the overlap damped by the *g(t)* is proportional to the absorption cross section. The result is the absorption

spectrum, cross section versus excitation frequency. Absorption spectrum shape depends on the $<i\ |i\ (t)>$ overlap: if ground and excited surfaces are more displaced, the faster the overlap decreases as the $|i\ (t)>$ propagates at the excited electronic surface, then the overall envelope of the absorption spectrum is more broad.[23]

1.4 Surface Enhanced Raman Spectroscopy

The term Surface enhanced Raman scattering (SERS) implies that the enhancement of the signal comes from the surface that influences the nearby molecules. Molecules are usually adsorbed to coinage metal nanoparticles or coinage rough metallic surfaces having nanoscale features.[26]

1.4.1 Plasmon Resonance
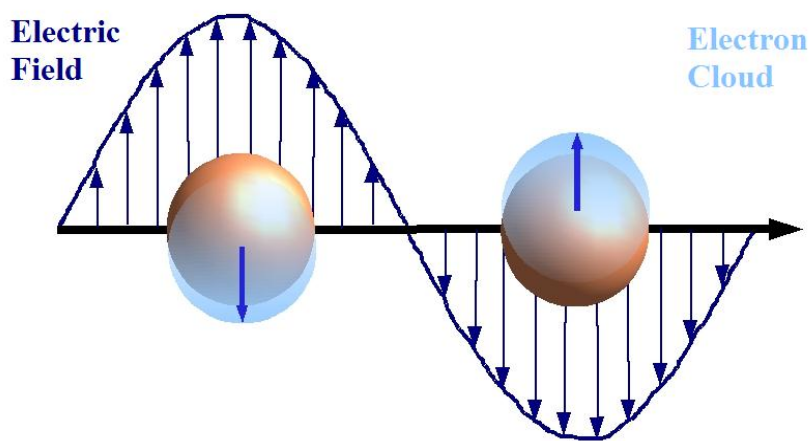
Figure 1-9. Nanoparticle surface plasmon resonance in an incident electromagnetic field; nanoparticle size is over-exaggerated.

Valence electrons in metals are essentially free, and can be visualized as a conduction electron sea that behaves like a gas of free particles inside the metal-- electron gas. In other words, metals can be seen as plasma, a medium with the same concentrations of negative charges (conduction electrons) and positive charges (ion cores), with at least one kind of charges being mobile. Incoming electromagnetic wave will interact with those mobile electrons since the electrons can move in response to the oscillating electrical field. The collective motion of the conduction electrons is termed a plasmon[26-28] and it occurs at resonant frequencies that are dependent on the complex dielectric function of the metal, its surface, size and shape[29]. Plasmons similar to phonons, vibrational waves of atoms or molecules in condensed matter, have a wavevector and a momentum. In bulk, propagating surface plasmons can be visualized as waves on the surface of the material. Photon interactions with surface plasmons in bulk are non-radiative due to energy and momentum conservation requirement (plasmons carry more momentum). Rough or nano features on a metal relax the momentum conservation requirement and the plasmon becomes radiative due to scattering.[30] As shown in Figure 1-9 when electromagnetic radiation is incident on nanoparticles, particle plasmons can be visualized as coherent oscillations of the electron clouds with respect to the driving electric field on individual particles with dipole and higher multiple transition moments. When nanoparticles are smaller than the wavelength of the incoming electromagnetic radiation, dipole transition moment is significant. For most of the metals plasmon lifetimes are short and energy dissipates as heat. Coinage/noble metals like gold, silver or copper have sufficient lifetimes to support plasmon

resonance resulting in scattering instead of heating; and coinage metals dipolar plasmon frequencies are such that that those metals have large internal fields[31], so each nanoparticle's dipole radiates its own field to a few nanometers. The electromagnetic field near each nanoparticle is a superposition of the incident electromagnetic radiation and the electromagnetic radiation due to the dipole on each particle. As a result, in certain areas around the nanoparticles the near field is enhanced and in other areas, it is reduced[32, 33]; therefore, each nanoparticle acts as a nanoantenna, concentrating electromagnetic radiation in some regions around itself.[34, 32, 35] The distinctive property of gold, silver and copper complex dielectric functions is that their plasmon frequencies lie within the visible spectrum.

1.4.2 Chemical and Electromagnetic Origins of SERS

Raman scattering and plasmon resonance discussed up to this point can be summarized as follows. Raman scattering of a molecule in terms of electromagnetic radiation depends on Raman polarizability of the molecule and on electromagnetic field E that is acting upon that molecule, Equation (1-25). The absorption of light by nanostructures creates strong local electric fields at locations of adsorbed molecules and, therefore, affects the local electric field near the molecules and the optical properties of the adsorbate. This is the basis for the Surface Enhanced Raman Scattering. Two mechanisms for SERS signal enhancement are theoretically possible and both come from Equation (1-25): chemical and electromagnetic ones.

$$E_{Raman} \propto \alpha_{Raman} E$$
(1-25)

Chemical enhancement mechanism is based on the change in polarizability of a molecule adsorbed on a metal nanoparticle, that results either from a charge transfer or bond formation of the metal and adsorbate.[39, 40, 41] For example, during a charge transfer, an electron in the metal conduction band can get excited to an empty state, and then a charge transfer can occur between the metal and the molecule. The electronic state involved is a virtual state given by the mixing of a molecule non-bonding state and any metal state.[42] This would change the polarizability of a molecule. Then the electron would decay back to the conduction band. Also for resonant molecules molecular dipole should interact with the nanoparticle dipole, changing molecular polarizability.

The electromagnetic enhancement mechanism involves change in the electromagnetic field. The incoming electromagnetic radiation interacts with small nanoparticles to create the surface plasmons. Types and sizes of nanoparticles are selected to be able to support surface plasmon resonance, as evidenced by a strong absorption in the UV-Vis spectrum of the metal; in fact, at the resonant frequency the absorption is much stronger than the absorption due to electronic transitions in solids (per-atom basis) or molecules. When a molecule is adsorbed on the metal surface, the stored energy in surface plasmon resonance may be transferred by means of dipole-dipole interaction from the metal nanoparticle (higher multipoles can be ignored for nanoparticles much smaller than the wavelength of light) to the molecule if the electronic resonance of the molecule is close enough to the metal one.[43] Therefore, the optical absorptions of metal nanoparticles and molecules under investigation should ideally somewhat overlap. Then the molecule not only interacts with an

incoming electromagnetic field, but also this field is changed by the nanoparticle and the molecule experiences an enhanced field.

Not considering molecule-nanoparticle dipole-dipole interactions and without carrying out the tensor products appropriately, it is possible to attain a simplified but easy to visualize description of the electric field enhancement factor averaged around each nanoparticle. Enhanced electromagnetic field averaged over the nanoparticle surface can be written as:

$$\langle E_{Enhanced} \rangle \propto N(w_L) E_L \qquad (1\text{-}26)$$

where $N(w_L)$ is a local near field enhancement factor averaged over a surface of the nanoparticle, and E_L is the incident laser field. Local near field enhancement factor depends on the incident laser frequency due to a position of a plasmon resonance of a nanoparticle. With this in mind, Equation (1-25) can be rewritten:

$$E_{Raman} \propto \alpha_{Raman} N(w_L) E_L \qquad (1\text{-}27)$$

where electromagnetic field E that is acting upon the molecule was replaced by the enhanced electromagnetic field averaged over the nanoparticle surface, $\langle E_{Enhanced} \rangle$.

In addition, Raman scattering from the molecule interacts with nanoparticles as well, and the scattered radiation will get enhanced yet again by a local near field enhancement factor over a surface of the nanoparticles at a Raman scattered frequency, $N(w_S)$. Raman scattering enhanced by the nanoparticle can than be expressed as:

$$E_{SERS} \propto \alpha_{Raman} N(w_L)N(w_S)E_L \qquad \textit{(1-28)}$$

Rewriting the above for total radiated power from a Raman transition or intensity using Equations (1-7) and (1-8) and omitting the prefactor:

$$I_{SERS} \propto |\alpha_{Raman}|^2 |N(w_L)|^2 |N(w_S)|^2 I_L \qquad \textit{(1-29)}$$

For the bands with very small Stokes shifts $N(w_L) = N(w_S) = N(w)$ and therefore the intensity of Raman scattering depends on the local near field enhancement factor to the fourth power.

Average SERS enhancement factor, $\langle F \rangle$, can be defined as the ratio of the Raman intensity enhanced by the nanoparticle presence to the unenhanced Raman intensity from the same molecule:

$$\langle F \rangle \approx \frac{|\alpha_{Raman\,Enhanced}|^2}{|\alpha_{Raman\,Unenhanced}|^2} |N(w_L)|^2 |N(w_S)|^2 \qquad \textit{(1-30)}$$

Again, assuming that the molecular polarizability is mostly unchanged, or assuming that chemical enhancement mechanism is negligible, we can define average SERS electromagnetic enhancement factor $\langle F_{EM} \rangle$:

$$\langle F_{EM} \rangle \approx |N(w_L)|^2 |N(w_S)|^2 \qquad \textit{(1-31)}$$

With regards to spherical nanoparticles the following assumptions can be made: dependence of local near field enhancement factor averaged over a surface of the nanoparticle, N, on incident light frequency, (w_L), and on Raman scattering frequency, (w_S), can be decoupled; and nanoparticle extinction profile is analogues to

local near field enhancement factor spectral profile, $A(w)$.[44] Average SERS electromagnetic enhancement factor can than be determined as either a function of incident light frequency or Raman scattering frequency:[45]

$$\langle F_{EM} \rangle \approx G\, A(w_L) A(w_S) \qquad\qquad (1\text{-}32)$$

where G is a substrate's geometric constant.

The above equation works for very large enhancement factors, however, it does not take into consideration that if there is no enhancement, than the enhancement factor needs to be one (unity):

$$\langle F_{EM} \rangle \approx G\, A(w_L) A(w_S) + 1 \qquad\qquad (1\text{-}33)$$

If one wishes to construct SERS enhancement profiles from extinction spectra, then simplified and picturesque model outlined in this section often times would suffice. Kerker has developed a more thorough and accurate equation for the average SERS electromagnetic enhancement factor;[46] however, when used, the equation gave almost exactly the same results, so it is not used as often as Equation (1-32). If one wishes to use theory to construct absorption spectrum or Raman excitation profiles quantitatively or more qualitatively, complex computational methods should be used, such as computational electrodynamics methods,[47-49] or electronic-structure methods[50, 51].

1.4.3 Hot Spots and Aggregated Metal Particles

When two nanoparticles come in close proximities, their dipoles are expected to interact. Using the two-sphere model for the nanoparticles of such aggregates, new

features in electromagnetic field around particles appear and there is a huge enhancement amplification.[52, 35, 53, 54, 55]
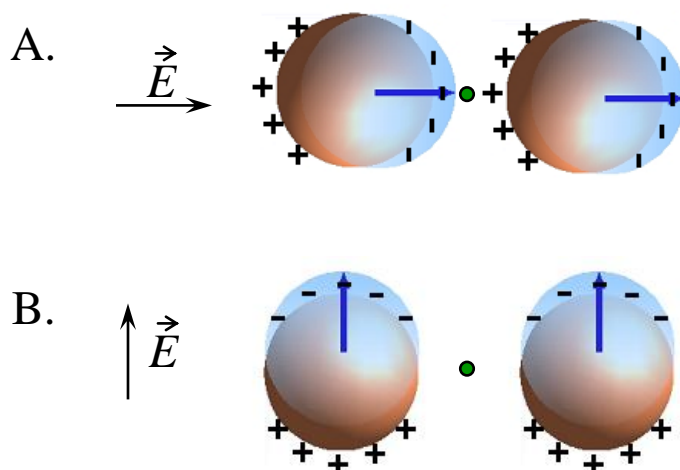
Figure 1-10. Surface plasmon resonance of two adjacent nanoparticles in an incident electromagnetic field; nanoparticles' size is over-exaggerated.

In a simple pictorial model, Figure 1-10, if two spherical nanoparticles, each much smaller than the wavelength of light, are brought together and a molecule is inserted in between the nanoparticles, then the molecule would feel different effective fields due to oscillations of the electron clouds depending on polarization of incoming light. If electric field is along the axis between two nanoparticles (Figure 1-10 A.), then oscillations of the electron clouds on the two nanoparticles would create an electron rich region on one nanoparticle next to an electron depleted region on the other nanoparticle. The molecule inserted in between the nanoparticles would not only be subjected to the incoming radiation, radiation on each nanoparticle, but also a

capacitive field from the two nanoparticles. In addition coherent interaction of induced dipoles on the nanoparticles would increase the field sensed by the molecule. If the nanoparticles are brought closer and closer together (infinitely small for the nanoparticle aggregates), the field sensed by the molecule would be much much larger than the incident electromagnetic field. On the other hand, if electric field is polarized perpendicular to the nanoparticle axis (Figure 1-10 A.), induced dipoles on the nanoparticles would still interact; however, dipoles on the nanoparticles would face the same direction and opposite charges on the nanoparticles would be further apart resulting in a smaller capacitive field. Regions of the aggregates that correspond to great amplification of the incoming electromagnetic field are termed "hot spots". Very nice calculations of electromagnetic fields around the nanoparticle aggregates were recently simulated by Käll at all and Schatz at al.[32, 33, 56]

1.4.4 Surface Enhanced Resonant Raman Spectroscopy

Up to this point resonant Raman spectroscopy and surface enhanced Raman spectroscopy were discussed. Oftentimes molecules that are studied with the use of SERS are electronically resonant themselves; this is termed surface enhanced resonant Raman spectroscopy (SERRS). Only recently few computational methods have become available accounting for the resonance, both on the molecule and on the nanoparticle and their interactions. [57, 51, 58]

One of the most thorough treatments is presented by Corni and Tomasi.[58] It starts with intensity given by Equation (1-29) and polarizability given by Equation (1-10). Polarizability accounts for molecular details and for the adsorption of the molecules to the nanoparticles but not for the formation of chemical bonds between the molecule and the nanoparticle and not for possible charge-transfers (ergo, it accounts for the physisorption and not for the chemisorption). A nanoparticle is treated as a continuous body with just electric response properties. A chromophore is treated with Hartree-Fock or with density functional theory. Electrostatic interaction between a molecule, a nanoparticle and a solvent are considered only. Therefore the molecule is not treated as a point dipole, but since no chemisorption is and charge transfer is considered, the signal enhancement account for electromagnetic enhancement mechanism only.

Jensen, Autschbach and Schatz have used a thorough method that can be used for describing electromagnetic enhancement of resonant molecules with surfaces that can support plasmon resonance without serious approximations.[51] In short, in calculation of induced polarization of the molecule, finite lifetimes of metal nanoparticle excited states are incorporated.[58] To carry out the computations, time-dependent density functional theory is used.

A particularly elegant method that qualitatively models electromagnetically enhanced spectra of SERRS and of "surface enhanced" extinction was presented by Kelley.[57] Both molecule and metal have dipoles associated with them. Density matrix theory is used for developing coupling between a molecule's transition dipole and a continuum of large transitions on a metal nanosphere.[58]

2 Motivation and Goals

One of the reasons why the proposed electromagnetic mechanism of surface enhanced resonance Raman scattering dominated the literature is that when nanoparticles aggregate, the SERRS intensity is enormously increased. This can be best explained by electromagnetic mechanism and a creation of "hot spots" with greatly increased fields in between aggregated nanoparticles. Since people were intrigued with such an enormous enhancement (Raman enhancements of $\sim 10^{10}$ were reported,[59] exceeding enhancement by perceivably unaggregated particles by six orders of magnitude) or because they wanted to use SERRS to detect minuscule amounts of analytes, a majority did not take into account influences of chemical enhancement mechanism.

The relationship between resonance enhanced Raman scattering and optical absorption is well understood as discussed in sections 1.3.2 and 1.3.3; however, collection of optical absorption spectra of molecules bound to SERS-active substrates was neglected until Franzen et al in 2002.[60] Franzen used absorption spectroscopy to find complementary information to SERS as an aid for getting an insight into the nature of the enhancement. For each chromophore, absorption spectra of the molecules on nanoparticles were collected and absorption spectra of the nanoparticles alone were also collected; the two were subtracted from one another and "difference" spectrum was created. Two types of molecules were observed. One type of molecules was likely to chemisorb to the nanoparticle surface and to have mixing of molecular orbitals with those of the metal (have a chemical enhancement mechanism); most of

them did not show the change of their linear absorption in presence of nanoparticles ("difference" spectra were the same as spectra of chromophores alone). However some molecules adsorbed to nanoparticles that were not expected to have chemical enhancement, and, therefore, which were expected to show only electromagnetic enhancement, showed a decrease in the absorption spectra of the molecules in the presence of nanoparticles. In other words, absorption spectra of dyes on nanospheres were weaker than the additive absorptions of dye and absorption of nanoparticles. This perturbation of electronic transitions should also affect SERRS profiles in ways that are not predicted by a simple proposed electromagnetic mechanism.

Similar disparity of "difference" and chromophore alone spectra were observed by others even when molecule-nanoparticle direct wavefunction overlap was supposed to be small.[61-65] Kelley has developed a model of coupling of molecule and nanoparticle transition moments that seems to qualitatively reproduce "interference" features of "difference" absorption spectra and spectra of chromophores alone.[66] This model was later expanded to model changes of extinction spectra upon addition of nanoparticles for more chromophores and for expected changes for Raman processes.[57]

However, there still have been very few studies of optical absorption spectra of molecules adsorbed to metal nanoparticles and study of their SERRS spectra.[61, 62, 67-72] More than that, there appears to be no studies of electronically resonant chromophores and nanoparticles looking at optical absorption, SERRS and resonant Raman spectra concurrently under identical conditions. **Therefore, the goal of this study is to measure optical absorption spectra (difference spectra) and SERRS**

enhancements for several electronically resonant chromophores bound to small, isolated, spherical gold and silver nanoparticles in colloidal solution.

Absorption spectra of nanoparticles alone, nanoparticles with chromophores and chromophores alone need to be collected. Resonant Raman spectra of chromophores and SERRS of chromophores with gold nanoparticles need to be collected as well. In ordinary resonance Raman, the resonance enhancement depends on the properties of the resonant electronic state and there is a close relationship between the optical absorption and the resonance Raman profile. Standard theories of SERS assume that the absorption spectrum of the chromophore is not perturbed by binding to the metal and that the Raman enhancement due to the metal and to the chromophore's resonance is simply multiplicative. A more "molecular" theory of SERRS points out that the chromophore's and the metal's electronic transitions should be coupled, producing perturbations in the absorption spectrum and non-multiplicity in the enhancement factors. If there is a contribution to SERS from "chemical" enhancement, i.e. the formation of new charge-transfer states, this should also perturb the absorption spectrum as well. So both spectra are needed to evaluate these competing mechanisms. If our collected spectra could be described by the model of coupling between a molecule's transition dipole and a continuum of large transitions on a metal nanosphere,[57] then electromagnetic enhancement of SERRS is dominant for the chromophore-nanoparticle system. If perturbation of the spectra can not be described by this model, then probably chemical enhancement mechanism is at play.

Ideally, chromophores need to be not only electronically resonant, but their absorption spectrum and nanoparticle's extinction need to somewhat overlap. The

interesting coupling between metal and chromophore electronic transitions should be significant only when both absorb in the same general spectral region. Ideally chromophores that can be soluble in water are preferred, since water-soluble nanoparticles are best characterized.

Small nanoparticles, 10 - 15 nm, are desirable since they are much easier to model theoretically as they are closer to a point dipole. Also, the ratio of surface area to volume is larger for smaller particles, and we do not want the chromophores to be so close together on the surface that the chromophore-chromophore interactions perturb their spectra, so we want only a small fraction of the available surface to be covered. A large nanoparticle with small fractional surface coverage will have such a large ratio of metal absorbance to chromophore absorbance that the chromophore contribution will be immeasurably small.

Aggregation needs to be avoided since it is known to greatly increase SERS enhancements. Unfortunately, the local electric field (under the electromagnetic theory) depends very strongly on the precise geometry of the aggregate and where on the aggregate the chromophore is bound. Aggregated samples will consist of a mixture of many different and unknown aggregate geometries which are impossible to model. For the same reasons, spherical nanoparticles need to be used: all positions on a sphere are equivalent, so if we use spheres the only degree of freedom we don't necessarily know is the orientation of the chromophore relative to the nanosphere (i.e. tangential, perpendicular, or something in between). Otherwise we would have to deal with the fact that different locations on the particle have different enhancements, and also likely have different but unknown binding affinities.

Dealing with aggregation could be cumbersome, but working with chromophores and nanoparticles in solution is essential; nanoparticles grown or deposited on a solid substrate would not work for our study due to the two outlined above reasons. First, the presence of the substrate makes different locations on the nanoparticle very different—i.e. right next to the substrate is different from the opposite side of the substrate. This problem is even worse if the nanoparticles are close enough together that they interact with one another. Second, if the nanoparticles are far enough apart that they don't interact, and the surface coverage with chromophores is low, the absorbance due to the chromophores will be too tiny (<0.001) to be measurable and the chromophore absorbance is one of the key components in the study.

3 Experimental and Computational Methods

3.1 Sample Preparation

3.1.1 Aqueous Citrate Reduced Silver and Gold Nanospheres

Aqueous solutions of silver and gold nanospheres were synthesized using sodium citrate reduction method.[73] Citrate acts not only as a reducing agent, but also it creates a loosely attached negatively charged ionic shell around each nanoparticle, therefore preventing nanoparticles from aggregation under the strong van der Waals

interactions. Things that affect the protective ionic layer may irreversibly aggregate/coalesce the particles together into larger clumps.

For preparation of silver nanospheres, 9 mg of $AgNO_3$ was dissolved in 50 mL of 40ºC nanopure water and heated with very vigorous stirring. At boiling, 1.5 mL of 1% sodium citrate solution was added rapidly. The solution was refluxed for 90 minutes with continuous vigorous stirring. Resulting brownish aqueous silver nanoparticle solution contained silver nanospheres with diameters of 46 ± 11 nm as judged from transmission electron microscopy (TEM) images and an absorption maximum of 416 nm.
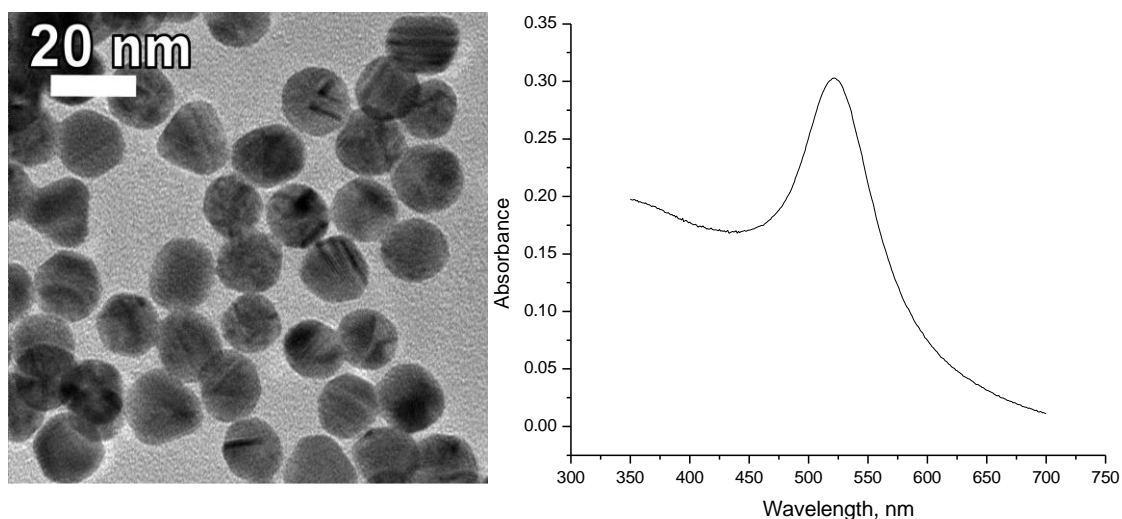
Figure 3-1. A transmission electron microscopy image and an absorption spectrum of citrate reduced gold nanoparticles.

For preparation of gold nanospheres the procedure was the same as above, except that 5 mg of $HAuCl_4 \cdot 3H_2O$ was added to 50 mL of nanopure water and 3 mL of citrate were added later. Resulting wine-colored aqueous gold nanoparticle solution contained gold nanospheres with diameters of 15 ± 2 nm as judged from

TEM images and an absorption maximum of 519 nm (Figure 3-1). Diameters of gold nanospheres should correspond to the absorption maxima: 8.9 nm corresponds to 517 nm absorption maximum; 14.8 nm to 520 nm; 21.7 nm to 521 nm; and 48.3 nm to 533 nm.[74]

3.1.2 Transferring Citrate Reduced Nanospheres into Other Solvents and Solvent Mixtures

Citrate reduced gold nanoparticles in 50 % ethanol and 50 % water mixture.

1 mL of ethanol was mixed with 1 mL of aqueous citrate reduced gold colloid. After 12 hours there was no visible change in the solution mixture. UV-Vis showed appearance of peak at a red tail part of the gold absorption spectrum indicative of some aggregation. Centrifugation at 3,300 rpm caused complete aggregation of nanoparticles leaving clear supernatant.

Citrate reduced gold nanoparticles in methanol

Citrate reduced particles in water were centrifuged down at 14,000 rpm for 30 minutes at 20 °C. The supernatant was discarded and the gold nanoparticle pellet was resuspended in MeOH.

Citrate reduced gold nanoparticles in 50 % methanol and 50 % water mixture.

1 mL of methanol was mixed with 1 mL of aqueous citrate reduced gold colloid. After 12 hours there was no visible change in the solution mixture. After centrifugation at 3,300 rpm UV-Vis spectra did not have a peak at the red tail end that is present for aggregated samples.

<u>Alkanethiol protected gold nanoparticles in ethanol.</u>

Attempt to transfer gold nanoparticles from aqueous solution into ethanol was made by replacing citrate ions with alkanethiols. Replacement of citrate ions with alkanethiols is thought to result in formation of a largely covalent with some ionic character Au-S bond.[75] Aqueous colloidal gold nanosphere solution was centrifuged down at 14,000 rpm for 30 minutes at 20°C; supernatant consisting of excess water and excess citrate ions was discarded. Amount of the alkanethiol needed to cover gold surface was calculated from head area of alkanethiol and surface area of nanoparticles knowing the average diameter of nanospheres, and amount of nanospheres present from extinction coefficient for the size of gold nanospheres. Different amounts (corresponding to fractions of a monolayer all the way to a few monolayers on a nanoparticle) of alkanethiol in ethanol were added to samples of centrifuged down gold nanoparticles. Absorption spectra were taken to judge the condition of the gold nanoparticles by looking at shapes of the spectra and absorption maximums.

6-mercaptohexanol was used to replace citrate ions. However, after 19 hours, the solution turned purple, and the resulting absorption maximum of gold nanoparticles was significantly red shifted which is usually indicative of nanoparticle aggregation. Possibly, six carbon long mercaptohexanol is too short to stabilize the gold nanoparticles. Prepared in the same manner, 11-mercaptodecanol capped nanoparticles also showed signs of aggregation.

3.1.3 Organoamine-Protected Gold Nanoparticles in Organic Solvents

Osterloh method was used.[76] Briefly, $HAuCl_4 \cdot 3H_2O$ and oleylamine (9-octadecenylamine) were refluxed in toluene for 2 hours. Then methanol was added to precipitate the particles, and later washed with methanol two more times. Nanospheres were dried to a black powder. When needed nanoparticles were resuspended in chloroform or toluene. Absorption spectrum showed that there were some aggregates formed, but most of nanospheres were not aggregated. Attempt to centrifuge down aggregated nanoparticles at 3,300 rpm leaving unaggregated still suspended in the solution did not pay off, the absorption spectra still indicated aggregate presence.

3.1.4 Using Various Dye Molecules in Search for a "Perfect" Nanoparticle-Adsorbate Combination

3.1.4.1 DANS-thiol

Dialkylaminonitrostilbene-thiol (DANS-thiol) was graciously provided by Mireille Blanchard-Desche. DANS-thiol is soluble in methanol among other solvents. Gold nanoparticles were transferred from water to MeOH as discussed above. The nanoparticle concentration was ~8.1 x 10^{-9} M based on $\varepsilon = 6.15$ x 10^7 M^{-1} cm^{-1} for 10 nm diameter particles in water (absorption spectrum of gold nanoparticles in water

was measured and then it was assumed that all gold nanoparticles were resuspended in methanol).[77] For chromophores to occupy 10% of the possible sites on 10 nm gold nanoparticles, so that chromophore-chromophore interactions are fairly minimal if the chromophores are randomly distributed, (there are 1948 binding sites per 10 nm particle calculated from information Blanchard-Desche group's paper[72]), calculated chromophore concentration had to be ~1.6 x 10^{-6} M based on the absorbance of ~0.05 at 430 nm and ε = 32131 M^{-1} cm^{-1} in toluene. Chromophore-nanoparticle solutions with different chromophore concentrations were centrifuged down at 14,000 rpm for 30 minutes at 20°C. Supernatant of each solution was collected to measure absorption spectrum and to therefore find out how much unbound DANS-thiol was left in the supernatant. Absorption and Raman spectra were taken of the nanoparticles alone, chromophore alone, and of nanoparticles with the chromophore.

Since gold nanoparticles did not show aggregation in 50:50 water and methanol solvent, the above experiments were repeated in the 50:50 methanol and water mixed solvent. DANS-thiol in methanol was added to citrate reduced gold or silver colloids in 1 to 1 volume ratios.

DANS-thiol is also soluble in chloroform and toluene. Organoamine-protected gold nanoparticles were resuspended in either chloroform or toluene and a similar set of experiments was performed as with citrate reduced nanoparticles described above.

3.1.4.2 Wu176

α-perfluoraryl-dicyanovinyl containing chromophore, Wu176, came from Alex K. Y. Jen and C. H. Wang. It was checked to be weakly water soluble. Wu176

was added to aqueous citrate reduced gold nanoparticles in different amounts approximately needed for 10 % coverage of binding cites on gold nanoparticles. Chromophore-nanoparticle solution was centrifuged down at 14,000 rpm for 30 minutes at 20°C; supernatant was collected to measure absorption spectrum and to, therefore, find out how much unbound Wu176 was left in the supernatant. Absorption and Raman spectra were taken of the nanoparticles alone, chromophore alone, and of nanoparticles with the chromophore.

3.1.4.3 JM

Julolidine malononitrile (JM) was obtained from Mireille Blanchard-Desche. JM is very slightly water soluble, so the procedure of adding JM to aqueous citrate reduced gold nanoparticles was similar to Wu176 procedure. Since JM absorption spectrum changed dramatically upon addition to gold colloid, pH of the JM and gold colloid solution was adjusted higher and lower, but the JM absorption spectrum still changed. Purging the JM and gold colloid solution with nitrogen gas did not help keep JM species the same. Amberlite, an ion-exchange polymer, was used to trap some of the excess citrate ions in attempt to prevent JM from changing to no avail.

3.1.4.4 DA+

4-N, N-bis(6''- (N, N, N- trimethylammonium) - hexyl) amino-4'-nitrostilbene dibromide (DA+) from Gui Bazan is water soluble and was added to aqueous citrate

reduced gold nanoparticles in the same fashion as Wu176. DA+ addition aggregated the nanoparticles.

3.1.4.5 Sy41

Indoline dimethine-malononitrile (Sy41) from Frank Wurthner is also water soluble. The procedure of adding Sy41 to aqueous citrate reduced gold nanoparticles the same as for Wu176. However, after the centrifugation, supernatant contained all of Sy41 indicating that Sy41 did not adsorb to gold nanoparticles at all. Addition of Amberlite to remove excess citrate ions did not seem to help.

3.1.4.6 FITC

Fluorescein isothiocyanate (FITC) is commercially available and it is also water soluble. Again, the procedure of adding FITC to aqueous citrate reduced gold nanoparticles the same as for Wu176. As for FITC, judging from the absorption spectrum, the supernatant contained 2/3 of the initial FITC concentrations. Amberlite did not help to increase FITC adsorption gold nanoparticles. Also in absorption spectrum of FITC that is absorbed to gold nanoparticles another peak appeared at about 600 nm. Raman spectra of FITC and gold nanoparticles did not show any FITC peaks.

3.1.4.7 CV

Crystal violet (CV) is water soluble. It was added to aqueous citrate reduced gold nanoparticles in different amounts approximately needed for 10 % coverage of binding cites on gold nanoparticles. Chromophore-nanoparticle solution was centrifuged down at 14,000 rpm for 30 minutes at 20°C. Absorption spectra of the supernatant were taken to see at which point all of the CV was bound to the nanoparticles and, therefore, when none of the CV was left in the supernatant. Since an absorption spectrum of CV and gold nanoparticles, with CV concentration corresponding to 100 % gold coverage, showed signs of nanoparticle aggregation, then a study to see what CV concentrations causes nanoparticle aggregation was conducted. Solutions of the chromophore and gold with CV concentration corresponding to 24-73 % gold surface coverage were prepared and absorption spectra and Raman spectra were taken to check for aggregation. CV concentration corresponding to 23- 65 % gold surface coverage did not show aggregation, and, therefore, only corresponding 0.2 to 0.5 μM CV solution (based on ε = 112,000 M^{-1} cm^{-1} at 590.5 nm, in water[78]) and 0.2 to 0.5 μM CV solution with gold colloid were prepared for taking Raman and SERS spectra as a function of excitation wavelength and for taking corresponding absorption spectra.

3.2 Absorption Measurement

Optical absorption spectra were obtained on a Cary 50 UV-Vis spectrophotometer in 1 cm path length quartz cuvettes.

44

3.3 Raman Measurement

3.3.1 Raman Experimental Setup

The experimental setup used to obtain Raman spectra is shown in Figure 3-3. Excitation wavelengths were chosen to intercept absorption spectra of the dyes (see Figure 3-2 for a CV example). As an excitation source the following lasers can be used depending on which wavelength of light needs to be generated: a Coherent Innova 90C-5 argon-ion laser, Melles Griot helium-neon lasers and an argon-ion-pumped continuous-wave dye laser (Coherent model 599 standing wave dye laser) operating with Rhodamine 6G in ethylene glycol. Generation of the needed excitation wavelengths is summarized in Table 3-1.

Table 3-1 Generation of excitation wavelengths

Wavelength, nm	Source
543.5, 594.1, 611.9, 632.8	Helium–Neon lasers
351.1, 363.8, 457.9, 465.8, 476.5, 488.0, 496.5, 501.7, 514.5	Argon-ion laser
565-640	Tunable dye laser

The lasers were operated so that the beam of no more than 4 mW was generated to prevent the sample from photoalteration, a degradation caused by the incident light such as local heating and depletion of the ground state population. The

excitation wavelength was separated from other lines with a use of a Pellin-Broca prism that does not cause as much intensity loss as a diffraction grating does, and the unwarranted lines were blocked by metal sheets and by an iris diaphragm.
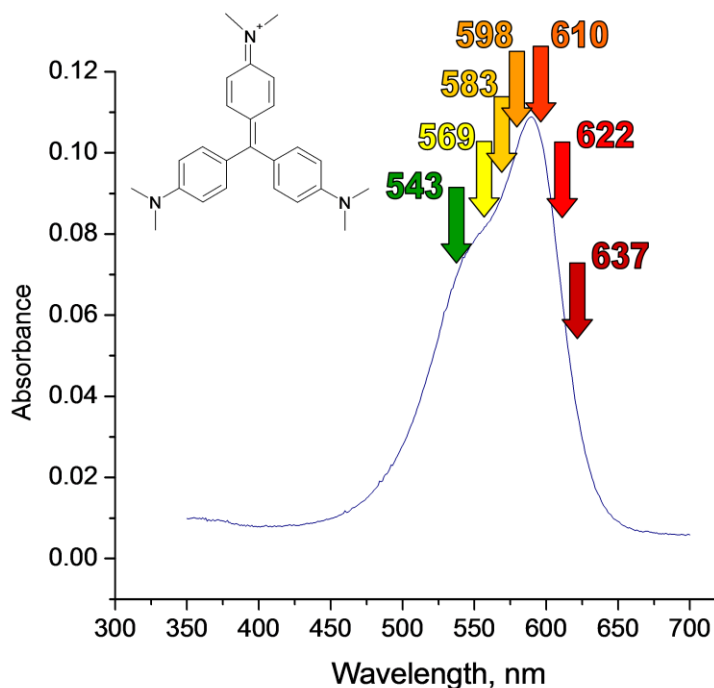
Figure 3-2. Relationship of excitation wavelengths to the CV absorption spectrum.

For lasers that generate only low power (e.g. He-Ne), laser line was passed through an adjustable polarization rotator and then through a polarizer in an attempt to maximize the excitation light while choosing only one appropriate polarization as shown in Figure 3-4. If laser power was already sufficient, then only a polarizer was used.
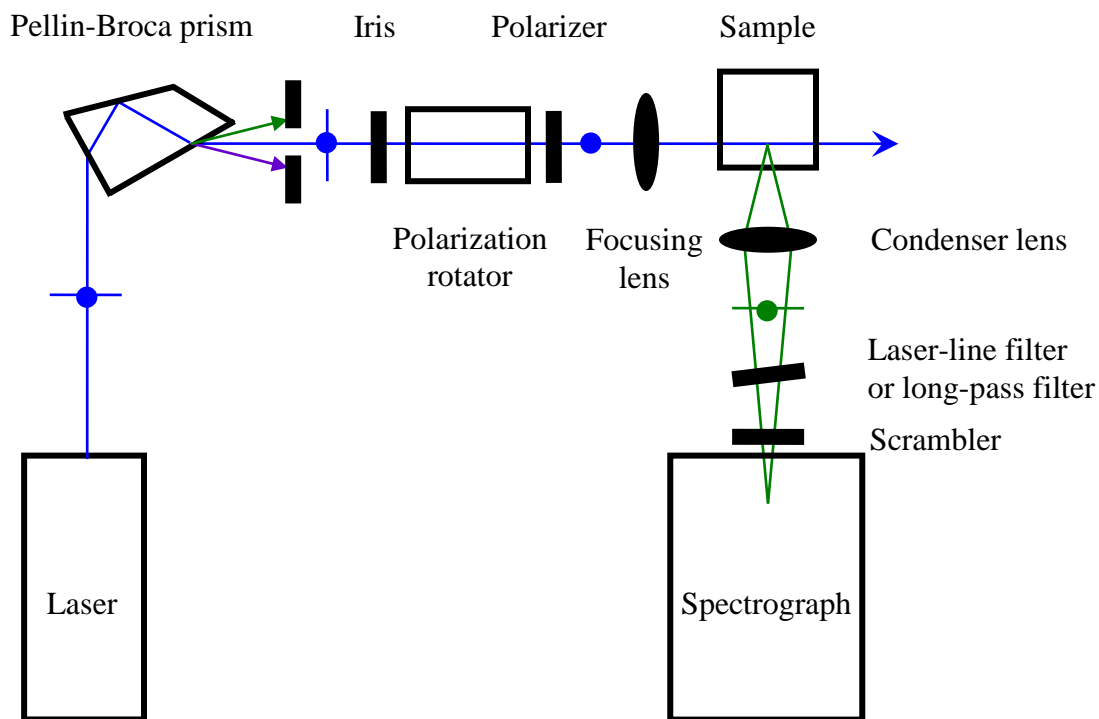
Figure 3-3. Schematic diagram of experimental system for collecting Raman

spectra.

For the detection, a macro-sampling system was used[79]. A 20 mm focal length lens focused the excitation light onto the cuvette with a sample in either 90° scattering geometry or in 45° backscattering geometry shown in Figure 3-4. Both of the geometries result in a majority of laser light being directed away from the detector while collecting Raman scattering. The scattered light is then passed through a condenser lens to focus the light onto the detector. Before reaching the detector the scattered light is either passed through a notch filter so as to filter out the excitation light or through a long-pass filter to let red-shifted scattered light only through. Also before reaching the detector the scattered light is passed through a polarization scrambler to randomize the scattered light polarization since different Raman lines

have different depolarization ratios and, therefore, they are not transmitted through a spectrograph with equal efficiencies.

The 90^0 scattering geometry   A backscattering geometry
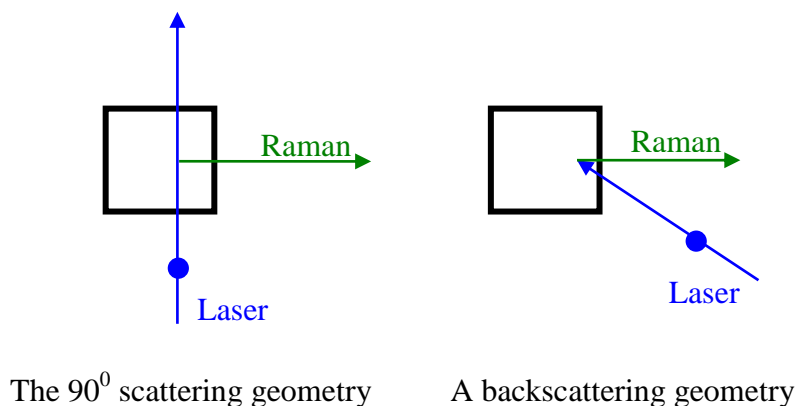
Figure 3-4. Schematic diagram of 90° and 45° scattering geometries in Raman spectroscopy.

The Raman scattering was dispersed with either of two spectrographs. One was a Spex 1877E 0.6 m triple spectrograph with a Spex Spectrum One liquid nitrogen-cooled charge-coupled device detector (CCD). The slit width at the entrance to the spectrograph stage was 200 μm, giving a spectral resolution of about 15–20 cm^{-1}, depending on the wavelength of the excitation laser. The other was a Spex 500M 0.5 m single spectrograph, with a Roper Scientific Spec 10:100B liquid nitrogen cooled, back-illuminated CCD. At the chosen slit widths, spectral resolution was about 7–14 cm^{-1} depending on the excitation wavelength. An advantage of a triple spectrograph is that it allows very efficient rejection of the laser beam at a cost of a lower throughput of scattering. On the other hand, even though it is harder to eliminate laser light from the single spectrograph, it provides more than 50% quantum efficiency from 400-850 nm.

For samples having low scattering intensity, integration of up to 5 minutes was performed and 4 to 16 spectral accumulations were collected to achieve decent signal to noise ratio. Corresponding amount of dark scans was collected. Spectra of cyclohexane was taken at each excitation wavelength and for each detection wavelength (it is nearly impossible to set Spex 500M spectrograph stage to the same detection wavelength every time). To correct spectra for detector sensitivity at each detection wavelength, a spectrum of an Optronic Laboratories 245C tungsten−halogen lamp was taken by bouncing the lamp light off a plate coated with $BaSO_4$ powder, which is a good diffuse scatterer, arranged in a similar manner as the sample.

3.3.2 Processing and Corrections to the Experimental Data

During Raman spectral accumulation charged subatomic particles called cosmic rays may impact the CCD. Cosmic rays reaching the detector mostly consist of hydrogen and helium nuclei. When these particles hit the CCD, they impact just a few pixels, causing a very sharp and narrow peak of high intensity in the spectrum that is unrelated to the Raman signal of an analyte. If cosmic rays were visible in each spectrum, they were manually removed in Microcal Origin. Sets of spectra were averaged out and a corresponding amount of dark scans was subtracted. The frequency axis was calibrated for each detection wavelength using known cyclohexane lines and experimental cyclohexane spectrum at that detection window

(Figure 3-5). Cyclohexane Raman shifts for frequency calibrations were established by the American Society for Testing and Materials (ASTM E 1840), At each detection window intensities were corrected for the wavelength dependent detector sensitivity using experimental and known spectra from the tungsten−halogen lamp (known lamp spectrum was provided by the lamp manufacturer).
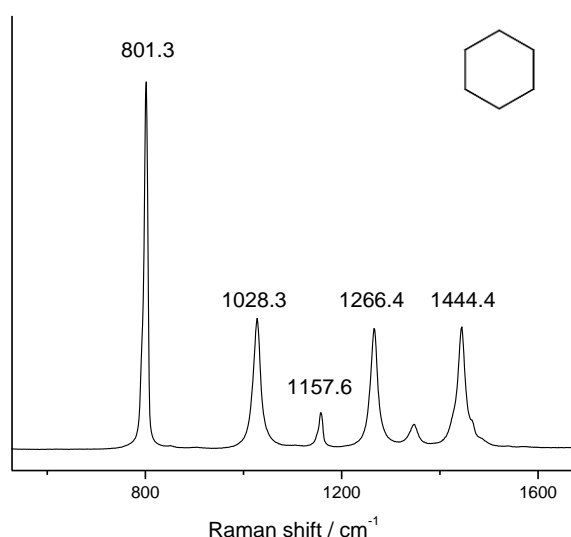
Figure 3-5. Known lines of cyclohexane used for calibration of the frequency axis.

Since the scattered light passes through a solution of chromophores or through a solution of chromophores and metal nanoparticles, different Raman lines are attenuated due to wavelength dependent light reabsorption by the solutions. Intensities had to be corrected for reabsorption. Using the Beer's law, it is straightforward to account for the reabsorption in a 90° scattering geometry knowing the absorption spectrum of the sample and the scattered light's path length through the sample on the way to the detector.

The reabsorption in a backscattering geometry is calculated using the following correction: [80]

$$I_{true} = I_{meas} \frac{\left\{[1+(A_S/A_L)\cos\theta](A_S/A_L)\cos\theta\right\}^{1/2}}{\tan^{-1}\left\{[A_S\cos\theta/(2A_L+2A_S\cos\theta)]^{1/2}\tan\alpha\right\}} \qquad (3\text{-}1)$$

where A_S and A_L are the sample's absorbances at the scattered and laser wavelengths, respectively, α is the half-angle subtended by the collecting mirror or lens, and θ is the angle between the incident laser direction and the detection direction.

If gently sloping fluorescence background was present it was subtracted using Microcal Origin. Band areas were determined using the Galactic Industries GRAMS/32 curve-fitting algorithm to fit mixed Gaussian/Lorentzian peak profiles.

In sections 1.3.2 and 1.3.3 integrated, or total, Raman cross section was discussed, which includes scattering in all directions. Since this Raman cross section is integrated over all directions, then it requires collection of scattering over all 4π steradians around the sample, which is difficult experimentally. In practice, it is more useful to define a differential Raman cross section for collection of Raman scattering in a specific direction over a small range of solid angles. For example, equation (1-7) can be rewritten to define a differential Raman cross section for a 90° scattering geometry:

$$\frac{dP_{I\rightarrow F}}{d\Omega}(90°) = I\frac{d\sigma_{I\rightarrow F}(w_L)}{d\Omega} \qquad (3\text{-}2)$$

where Ω is the solid angle of collection. Integrated Raman cross section is related to the differential Raman cross section using a Raman depolarization ratio of the particular Raman mode:[81, 82]

$$\sigma_{I \to F}(w_L) = \frac{8\pi}{3} \left(\frac{1+2\rho}{1+\rho} \right) \left(\frac{d\sigma_{I \to F}(w_L)}{d\Omega} \right) \tag{3-3}$$

Oftentimes differential Raman cross section is reported; however, if the need arises, one can setup a relatively simple experiment involving a polarization analyzer to measure the depolarization ratio of the Raman mode, and then one can use equation (3-3) to calculate the integrated, or total, cross section. The Raman depolarization ratio is defined as:

$$\rho = \frac{d\sigma_{I \to F}^{\perp}(w_L)}{d\Omega} \Bigg/ \frac{d\sigma_{I \to F}^{\parallel}(w_L)}{d\Omega} \tag{3-4}$$

where $\dfrac{d\sigma_{I \to F}^{\perp}(w_L)}{d\Omega}$ and $\dfrac{d\sigma_{I \to F}^{\parallel}(w_L)}{d\Omega}$ denote scattered radiation that is polarized perpendicular to the incident light and parallel to the incident light respectively.

Differential cross sections for the chromophores were calculated relative to the known cross sections for the 1035 cm^{-1} Raman line of the internal standard methanol that was added to all of the samples and with use of the following equation:[83]

$$\left(\frac{d\sigma}{d\Omega} \right)_u = \frac{I_u}{I_v} \frac{c_v}{c_u} \left(\frac{d\sigma}{d\Omega} \right)_v \tag{3-5}$$

where u and v denote solute and solvent, respectively, I is the measured integrated band intensity, and c is the concentration. The methanol cross sections were assumed to obey an A-term dependence:

$$\left(\frac{d\sigma}{d\Omega} \right)_u = K v_0 (v_0 - v_v)^3 \left[\frac{\left(v_e^{\;2} + v_0^{\;2} \right)}{\left(v_e^{\;2} - v_0^{\;2} \right)^2} \right]^2 \tag{3-6}$$

where v_0 is the laser excitation wavenumber in cm^{-1}, v_v is the Raman shift of the vibration, v_e is the wavenumber of the resonant state, and K is a prefactor that scales the overall cross sections. The A-term parameters for methanol and the 1035 cm^{-1} Raman line, $v_v = 1035$ cm^{-1}, were obtained from Ref. [83]

4 Results and Discussion

4.1 DANS-thiol
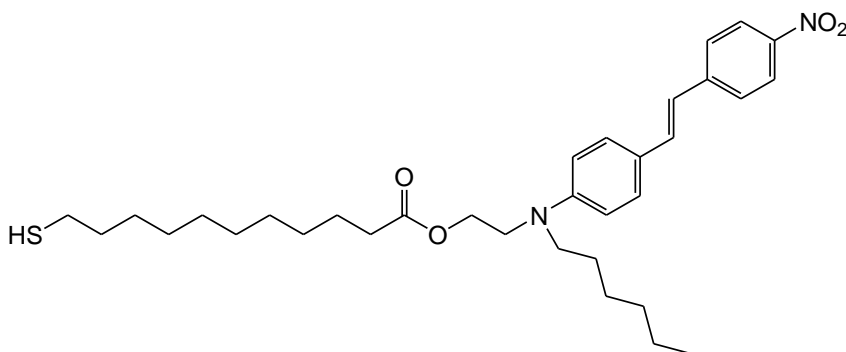
Figure 4-1. DANS-thiol molecule.

DANS-thiol concentration of about 1.6 x 10^{-6} M were chosen so that the chromophores would occupy 10% of the possible sites on gold nanoparticles, that way chromophore-chromophore interactions would be fairly minimal if the chromophores are randomly distributed on the gold nanoparticles as depicted on the schematic illustration (Figure 4-2). As calculated in the adsorption study of the chromophores to nanoparticles discussed below this concentration corresponds to around 20% of possible DANS-thiol coverage of our gold nanoparticles.
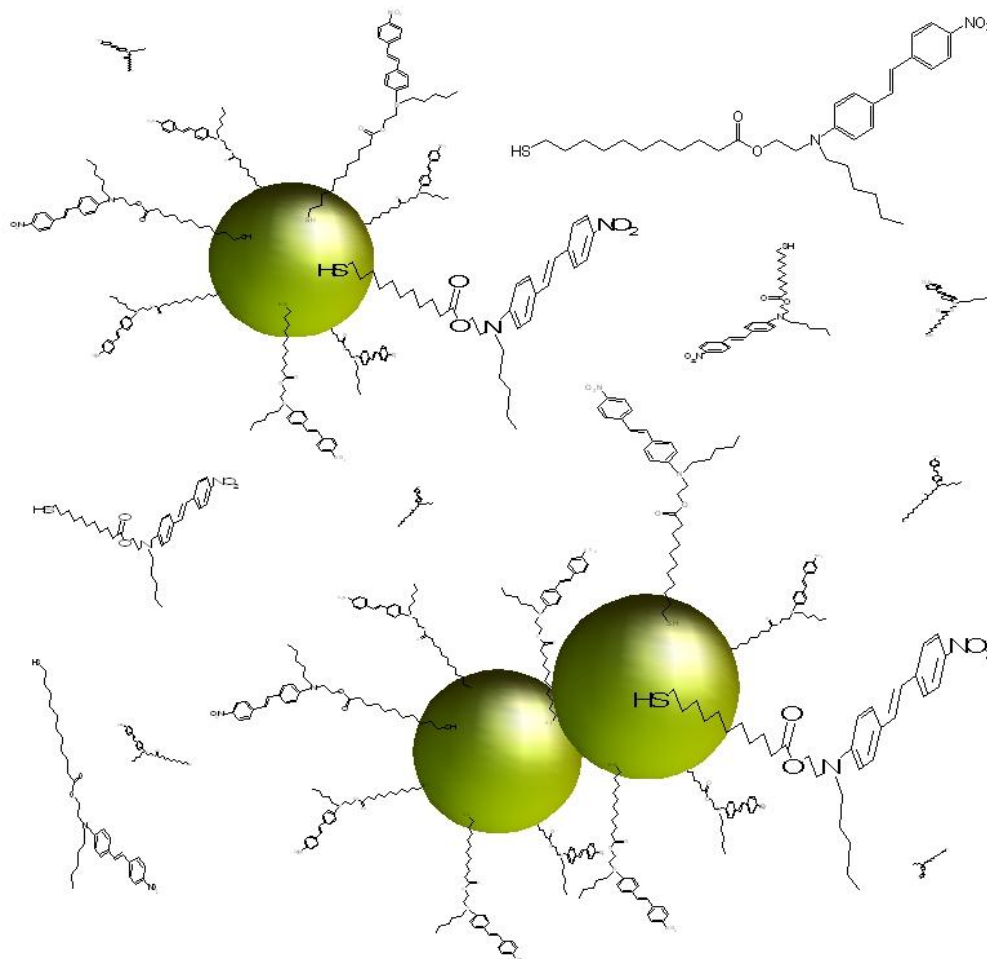
Figure 4-2. Schematic illustration of nanoparticles with DANS-thiol molecules.

4.1.1 Absorption Spectrum and Raman Spectrum

The absorption spectrum of the DANS-thiol/Au system (Figure 4-3 Left) shows a significant shift and broadening of the plasmon resonance to longer wavelengths relative to bare Au. The displayed spectrum has been scaled so that the integrated absorbances (250-850 nm) of Au alone plus DANS alone equal that of Au + DANS. Before scaling, Au + DANS has about 7% greater area than the sum of the two components. This could be an artifact resulting from increased scattering after

binding the chromophore. In any case, whether scaled or unscaled spectra are used, the difference spectrum (Au + DANS minus Au alone) shows a negative-going peak at about 505 nm and a positive peak at about 555 nm. Red-shifting of the plasmon resonance upon binding to analytes, whether or not they are near-resonant with the plasmon absorption, has been observed in other studies [62, 70, 84] but was not seen for the DANS-thiol on alkylthiol-coated Au nanoparticles in toluene.[72] In the difference spectrum, the negative peak at around 505 nm and a positive peak at about 555 nm could be due to dipole interactions of the chromophores and nanoparticles, but they could be also due simply to nanoparticle aggregation and, therefore, shift of nanoparticle absorbance to longer wavelengths.
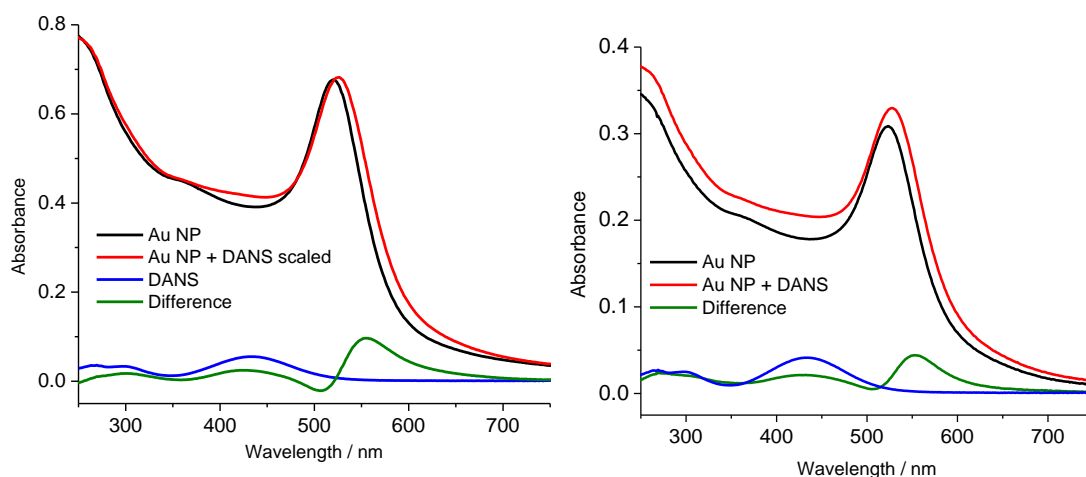
Figure 4-3. Left: Absorption spectra of gold nanoparticles with DANS-thiol, gold nanoparticles alone, the difference of the above two and DANS-thiol alone in MeOH. Right: Absorption spectra of gold nanoparticles with DANS-thiol, gold nanoparticles alone and the difference of the above two in 50:50 MeOH:H$_2$O.
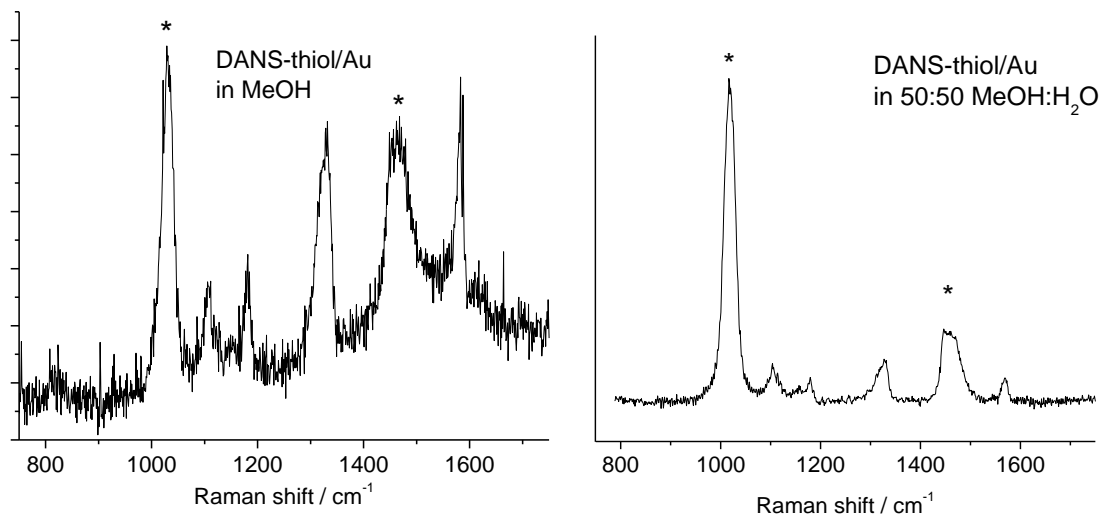
Figure 4-4. Left: Raman spectra of gold nanoparticles with DANS-thiol in MeOH obtained with 543 nm excitation. Right: Raman spectra of gold nanoparticles with DANS-thiol in a 50:50 mixture of MeOH and H_2O obtained with 514 nm excitation.

As collected Raman spectra of gold nanoparticles with DANS-thiol in MeOH, presented in Figure 4-4 Left, were obtained with very weak 543 nm excitation from a He-Ne laser. The spectra are noisy due to weak laser power available from the green He-Ne laser, nevertheless the spectra show peaks at nearly the same frequencies as the strongest peaks of DANS alone[85] (817, 1110, 1188, 1339, and 1585 cm^{-1}). The MeOH peaks are labeled with asterisks. Using the 1035 cm^{-1} methanol peak as an internal standard[83] and assuming its Raman cross section in the Au solution is the same as in pure methanol (see below), we obtain a cross section for the NO_2 stretch of DANS-thiol of 1.6 x 10^{-7} $Å^2$ sr^{-1}.   This is 17 times higher than we previously

measured for DANS-thiol in pure methanol (no nanoparticles) at the *peak* of the excitation profile (at 430 nm).

We did not measure cross sections for DANS-thiol in methanol at wavelengths as long as 543 nm (weak He-Ne has insufficient power to see Raman spectrum of DANS-thiol alone in methanol), but our fits to the excitation profiles[85] allow us to estimate a cross section of 2.9 x 10^{-10} 10^{-8} $Å^2$ sr^{-1} at this wavelength. Therefore, the apparent enhancement factor at 543 nm is about 550. This is not a large enhancement by SERS standards, but we are deliberately trying to work under conditions where we expect the SERS enhancements to be small (unaggregated particles) and also, we hope, calculable.

This method may underestimate the true surface enhancement because it assumes all chromophores are bound to the metal and it ignores surface enhancement of the methanol Raman cross sections. The assumption that nearly all of the DANS-thiol chromophores are bound to the metal is likely to be quite good because –SH groups bind strongly to gold, and it was checked by centrifuging down the nanoparticles and checking the absorption spectrum of the supernatant, which is discussed in more detail in the Adsorption Study section that follows. Neglecting surface enhancement of the methanol solvent, use of methanol solvent as an internal standard may be justified because only a small fraction of the solvent molecules are close to a nanoparticle. The methanol solvent peaks are actually considerably weaker in the gold solutions than in pure methanol, as expected because of the absorption of the incident laser light and scattered light by the nanoparticles.
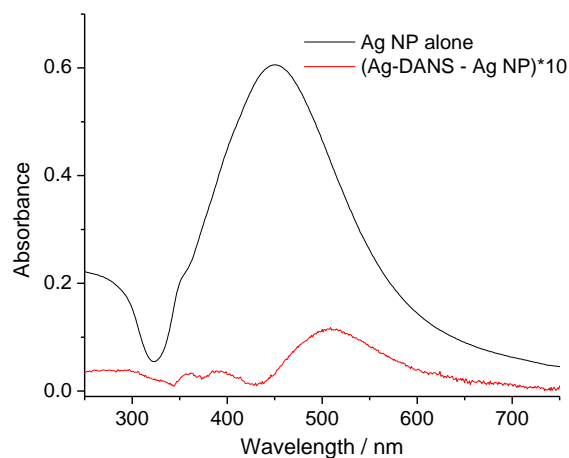
Figure 4-5. Absorption spectra of silver nanoparticles alone and difference of absorption spectra of silver nanoparticles with DANS-thiol and absorption spectra of DANS-thiol alone.

Spectra were also obtained for the DANS-thiol on Au nanoparticles in a 50:50 mixture of MeOH and H_2O. Concentration of gold nanoparticles and DANS-thiol was halved. The absorption spectrum had very similar features (shown in Figure 4-3 Right); however, the negative peak at about 505 nm and a positive peak at about 555 nm are not as large as in samples in pure MeOH solvent. Corrected Raman spectrum of DANS-thiol on gold in a 50:50 mixture of MeOH and H_2O obtained with 514 nm excitation is presented in Figure 4-4 Right. Since methanol to DANS-thiol ratio was held the same as it was in MeOH only solvent, one would expect Raman spectra of DANS-thiol with Au in MeOH would look very similar to Raman spectra of DANS-thiol with Au in 50:50 mixture of MeOH and H_2O (Left versus Right in Figure 4-4), however, DANS-thiol peaks in the mixture of solvents appear much smaller in comparison to MeOH peaks marked by asterisks. This suggests that nanoparticles did

58

aggregate in pure MeOH solvent, which probably resulted in some DANS-thiol molecules being located in hot spots, sites where nanoparticles come together and where adsorbed molecules feel much stronger electric field enhancements by nanoparticles, resulting in more intense SERRS spectrum.

Spectra were also obtained for the DANS-thiol on Ag nanoparticles of estimated diameter ~50 nm, in a 50:50 mixture of MeOH and H_2O. The absorption spectrum also shows slight broadening to the red and a small relative dip near the peak of the DANS absorption, although again there is ambiguity about how to scale the Ag alone and Ag-DANS spectra. The Raman spectra are quite similar to those obtained on Au. The cross section calculated for the 1339 cm^{-1} NO_2 stretch on Ag at 543 nm is 1.6 x 10^{-7} $\mathring{A}^2$ sr^{-1}, identical to that found on Au. This is somewhat surprising given the much bluer plasmon resonance frequency of Ag, although Ag does tend to give stronger SERS enhancements than Au. In addition, strong SERS signal is probably due to aggregation of silver nanoparticles by methanol; larger silver nanoparticles are more prone to aggregation than our gold nanoparticles.
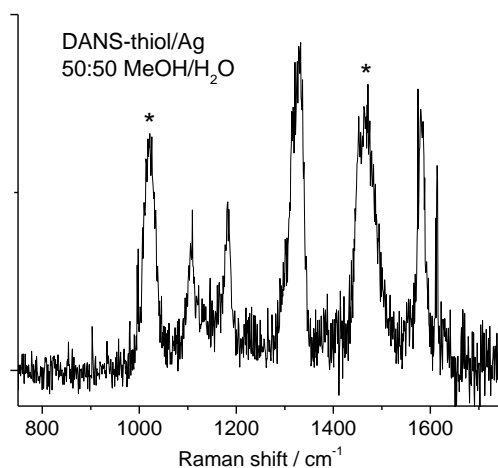
Figure 4-6. Raman spectra of silver nanoparticles with DANS-thiol obtained with

543 nm excitation.

4.1.2 Chromophore to Nanoparticle Adsorption Study

As was mentioned in the experimental section, for DANS-thiol to occupy 10 % of possible binding sites on 10 nm gold nanoparticles, calculated chromophore concentration had to be ~1.6 x 10^{-6} M assuming that all of the DANS-thiol nanoparticles bind tightly to the metal nanoparticles.

The assumption that nearly all of the DANS-thiol chromophores are bound to the metal is likely to be quite good because –SH groups bind strongly to gold, and it can be checked by centrifuging down the nanoparticles-chromophore solution and checking the absorption spectrum of the supernatant. If adsorption of the chromophores is strongly favored, then there should be an upper limit of a chromophore concentration under which no chromophores are present in the supernatant, and above which chromophores appears in the supernatant and can be identified by the absorption spectrum. We assume that this "upper limit" concentration can be equated to 100 % gold coverage. In case of DANS-thiol there was no such clear concentration cut off under which there was no DANS-thiol left in the supernatant.

In this case, we can look at the adsorption process as an equilibrium between adsorbed molecules and chromophore molecules in the solution. Then we can still calculate 100 % gold surface coverage utilizing simple experiments and crude theory[86] we can attempt to calculate an equilibrium constant and an amount of surface sites on our 15 nm gold nanoparticles that DANS-thiol molecules can adsorb to. First of all we need to make following assumptions: DANS-thiol molecules do not interact

with each other in the solution; once DANS-thiol molecules attach to nanoparticles they do not interact with one another; enthalpy of adsorption is independent of nanoparticle surface coverage; and finally an assumption that there is only finite amount of surface sites available where DANS-thiol molecules can adsorb. We can represent adsorption desorption process by the following equilibrium:

$$\text{DANS-thiol} \quad + \quad \text{NP} \quad \underset{k_d}{\overset{k_a}{\rightleftharpoons}} \quad \text{DANS-thiol-NP}$$
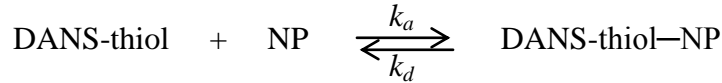
where k_a and k_d are rate constants for adsorption and desorption, respectively. Equilibrium constant is then:

$$K_c = \frac{k_a}{k_d} = \frac{[\text{DANS-thiol-NP}]}{[\text{DANS-thiol}][\text{NP}]} \qquad (4\text{-}1)$$

We can define the concentration of total available sites for DANS-thiol adsorption as σ_0; concentration of adsorbate (or concentration of occupied sites) on the nanoparticle surface can be defined as σ. Then a fraction of occupied sites, θ, would be $\theta = \dfrac{\sigma}{\sigma_0}$. It follows that concentration of empty sites would be $\sigma_0 - \sigma$ or $\sigma_0 - \sigma_0\theta$ or $\sigma_0 - \sigma_0\theta$ or $\sigma_0(1-\theta)$. Rate of desorption can be written as a product of a desorption rate constant and concentration of adsorbate sites on the surface:

$$rate \ of \ desorption = k_d\sigma = k_d\sigma_0\theta \qquad (4\text{-}2)$$

Rate of adsorption can be written as a product of an adsorption rate constant , concentration of empty sites on the surface and concentration of DANS-thiol in bulk:

$$\textit{rate of desorption} = k_a \sigma_0 (1 - \theta)[\text{DANS-thiol}] \qquad\qquad \textit{(4-3)}$$

Rate of adsorption should be equal to rate of desorption at equilibrium, so we can combine equations (4-2) and (4-3). Rearranging and using $K_c = k_a / k_d$, we get:

$$\frac{1}{\sigma} = \frac{1}{\sigma_0 K_c} \frac{1}{[\text{DANS-thiol}]} + \frac{1}{\sigma_0} \qquad\qquad \textit{(4-4)}$$

which looks exactly as a linear equation $y = mx + b$ that we can plot. Therefore y intercept would correspond to $1/\sigma_0$; and K_c could be calculated from the slope.

Solutions of gold nanoparticles with different DANS-thiol concentrations, $[\text{DANS-thiol}]$, were prepared. The solutions were then centrifuged down to create nanoparticle-dye pellets and concentration of DANS-thiol in supernatant was obtained from absorption spectrum of the supernatant. Next concentration of DANS-thiol on nanoparticles, σ, was calculated from concentrations of DANS-thiol in the initial solution and from concentration of left over DANS-thiol in the supernatant.

Absorbance of DANS-thiol alone for what was calculated to be 6 % coverage of gold nanoparticles (8.9 x 10^{-7} M DANS-thiol) in MeOH was 0.0288, absorbance of DANS-thiol left in the supernatant was 0.00634 (shown in Figure 4-7); therefore, most of the DANS-thiol was adsorbed on gold nanoparticles. At about 4.5 x 10^{-7} M DANS-thiol concentration or 3 % gold coverage (absorbance of about 0.14 for DANS-thiol alone) almost all of the chromophore was attached to the nanoparticles and almost nothing was left in the supernatant.
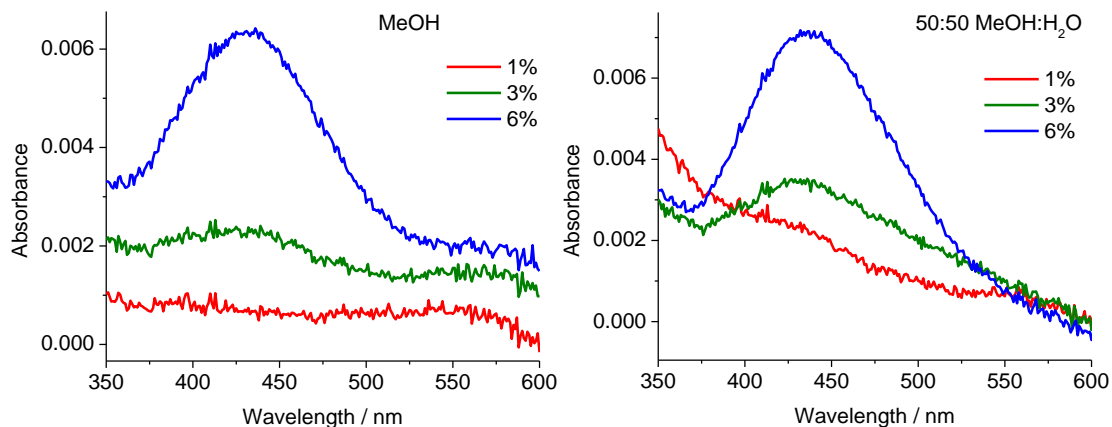
Figure 4-7. Left: Supernatant absorption spectra of gold nanoparticles with DANS-thiol in MeOH with dye concentration corresponding to calculated nanoparticle coverage percentages. Right: The same but for gold nanoparticles with DANS-thiol in 50:50 MeOH:H_2O.

From the $1/\sigma$ versus $1/[\text{DANS-thiol}]$ plots (Figure 4-8) maximum concentrations of DANS-thiol that can be of gold nanoparticles were found to be 3.14 x 10^{-7} M and 4.98 x 10^{-7} M for DANS-thiol and gold nanoparticles in MeOH and in MeOH:H_2O correspondingly. K_c were found to be 62.1 and 23.0 for DANS-thiol and gold nanoparticles in MeOH and in MeOH:H_2O, correspondingly. It is important to point out, in Figure 4-8, absorbances were used instead of concentrations as molarity units on the both sides of the equation (4-4) cancel out anyway. Also a point that corresponds to 1% gold coverage on the plot for MeOH:H_2O (it would have been in the top right) was excluded as an outlier.
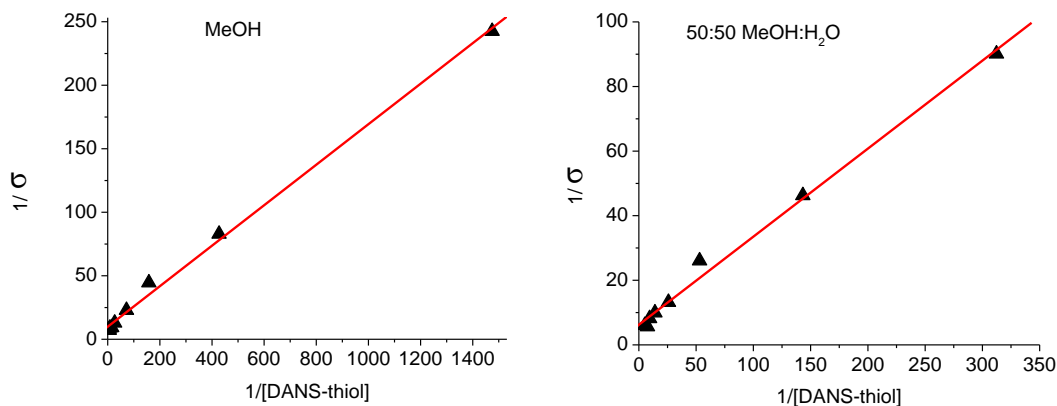
Figure 4-8. 1/σ versus 1/[DANS-thiol] plots.

Certainly there were a lot of approximations, and absorbances measured were very small and, therefore, not very accurate; nevertheless, above manipulations help to roughly establish what corresponds to 100 % nanoparticle coverage. Thus throughout our experiments ~1.6 x 10^{-6} M concentration of DANS-thiol adsorbed to 15 nm gold nanoparticles actually corresponds to about 20 % coverage (not to 10 % coverage calculated initially using geometric considerations for 10 nm gold nanoparticles.)

4.1.3 Differential Raman Cross Sections and Raman Excitation Profiles for the SERS Enhancements

Raman spectra were obtained for DANS-thiol and gold nanoparticles in MeOH and in 50:50 MeOH:H$_2$O using different excitation wavelengths. Differential Raman cross sections for 1334 and 1584 cm^{-1} DANS-thiol peaks (Figure 4-4) were

calculated using MeOH peaks and MeOH as an internal standard. Differential Raman cross sections for DANS-thiol on Au nanoparticles in MeOH and for DANS-thiol on Au nanoparticles in 50:50 MeOH:H_2O are presented in Table 4-1 and in Table 4-2 correspondingly. From the differential Raman cross sections at different excitation wavelengths excitation profiles were constructed (Figure 4-9 and Figure 4-10).

Table 4-1: Differential cross section for DANS-thiol on Au nanoparticles in MeOH at different excitation wavelengths

Peaks, cm^{-1}	Differential cross section	457.9 nm	465.8 nm	476.5 nm	488 nm	496.5 nm	514.5 nm
1338	$(d\sigma_R/d\Omega)_u$, 10^{-8} A^2sr^{-1}	6.01	5.41	8.15	7.65	1.13	1.53

The excitation profile for DANS-thiol and gold nanoparticles in MeOH seems to simply follow the absorption spectrum of gold nanoparticles and does not reflect features of DANS-thiol absorption. From Raman spectra of DANS-thiol with gold nanoparticles in both solvents represented in Figure 4-4, it was clear that chromophore with gold in MeOH had very strong Raman peaks compared to MeOH peaks; on the other hand, the chromophore with gold nanoparticles in the mixed solvent had much weaker chromophore peaks compared to MeOH peaks. Since chromophore to MeOH and to gold nanoparticles ratio was held constant in both solvents, then what must have changed is the environment of the dye molecules adsorbed on to the gold surface. If the nanoparticles did aggregate more in MeOH, then chromophores adsorbed in the sites where aggregated nanoparticles joined together felt much stronger enhanced electromagnetic field and their Raman

scattering was enhanced much more than Raman scattering from adsorbate on unaggregated surfaces. Therefore, the excitation profile presented in Figure 4-9 represents mostly adsorbates in aggregated areas of gold nanoparticles. This means that in the absorption spectrum of the "difference" in Figure 4-3 Left a negative peak at around 505 nm and a positive peak at about 555 nm were more than likely due to nanoparticle aggregation as discussed earlier.
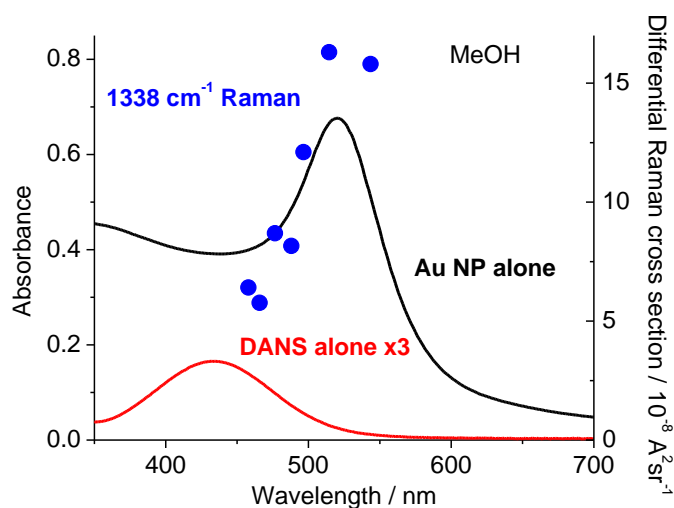
Figure 4-9. Excitation profile of DANS-thiol on gold nanoparticles in MeOH for the 1338 cm^{-1} line (blue circles); and absorption spectra of Au nanoparticles alone and of DANS-thiol alone times 3.

Raman cross sections for DANS-thiol and gold nanoparticles in the mixed MeOH and H$_2$O solvent were three times smaller than the corresponding cross sections in MeOH solvent (Table 3-2). Smaller in magnitude differential Raman cross sections were encouraging because that could have meant that there were no aggregated nanoparticles in the solution, and we can not only study the chromophore-

nanoparticle systems experimentally, but later we can model the chromophore-nanosphere system, and then assume that all other chromophore-nanoparticle systems are quite similar and extrapolate the model to the ensemble of the systems.

Table 4-2: Differential cross section for DANS-thiol on Au nanoparticles in 50:50 MeOH:H₂O at different excitation wavelengths

Peaks, cm^{-1}	Differential cross section	457.9 nm	465.8 nm	476.5 nm	488 nm	496.5 nm	514.5 nm
1338	$(d\sigma R/d\Omega)u$, 10^{-08} A^{2}sr^{-1}	0.94	0.75	1.37	3.03	2.94	4.79

However, the excitation profile for DANS-thiol and gold nanoparticles in the mixed solvent (Figure 4-10) qualitatively looks like the excitation profile for the chromophore and nanoparticle in the MeOH solvent-- it follows the absorption spectrum of gold nanoparticles and does not reflect features of DANS-thiol absorption. Since nanoparticles were clearly aggregated in MeOH and since excitation profiles look qualitatively the same for both MeOH and the mixed solvent, then the excitation profile of DANS-thiol and gold nanoparticles in 50:50 MeOH:H$_2$O is also a representation of mostly chromophores in the hot spots of the aggregated nanoparticles. Aggregation of gold nanoparticles in the mixed solvent is also consistent with why there are similar features in "difference" absorption spectra for the chromophore and gold in MeOH (where we know nanoparticles have aggregated) and in "difference" absorption spectra for the chromophore and gold in the mixed solvent (negative peaks at around 505 nm and positive peaks at about 555 nm in Figure 4-3 Left and Right).
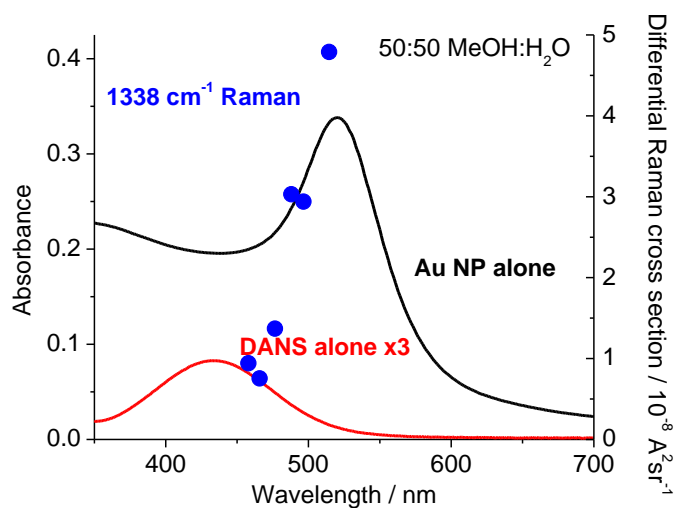
Figure 4-10. Excitation profile of DANS-thiol on gold nanoparticles in MeOH:
H2O for the 1338 cm^{-1}(blue circles); and absorption spectra of Au nanoparticles
alone and of DANS-thiol alone times 3.

Furthermore, an attempt was made to replicate the results for DANS-thiol and gold nanoparticles in the mixed in 50:50 MeOH:H_2O solvent that presented in Table 3-2 and Figure 4-10. However, the absorption spectrum for the same conditions was not the same; and magnitudes for Raman differential cross sections were also different. The key to the irreproducibility could be that nanoparticles are happy in water (they do not aggregate in water) and the chromophore is happy in MeOH (DANS-thiol is not soluble in water only). This could result in non-reproducible inhomogeneous environment around the nanoparticles and in the solution, and therefore in different degrees of nanoparticle aggregation from run to run.

4.1.4 DANS-thiol and Au NPs in Organic Solvents

Alkanethiol protected gold nanoparticles in ethanol were prepared. After DANS-thiol was added to these nanoparticles the solution was centrifuged and the supernatant was found to contain all of the initially added DANS-thiol, indicating that none of the DANS-thiol could displace the alkanethiols on the surface of the nanoparticles.

Organoamine-protected gold nanoparticles were prepared and resuspended in chloroform or in toluene. DANS-thiol was added, absorption spectrum and Raman spectrum was taken of DANS-thiol alone and of DANS-thiol with gold nanoparticles. Adsorption of the chromophore to the nanoparticles could not have been carried out with a use of the centrifugation method since the centrifugation vials would have been dissolved by the solvents. However from taking Raman spectra, Raman cross sections for DANS-thiol alone and for DANS-thiol with gold nanoparticles appeared to be the same, indicating that there was no SERS for DANS-thiol around organoamine-protected gold nanoparticles, which means that DANS-thiol failed to attach to these nanoparticles.

4.2 Wu176, JM, SY41, DA+, FITC

Other cyano-substituted chromophores were used next. All of them are expected to bind to gold nanoparticles through the CN groups.
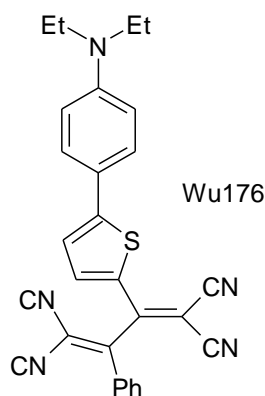
Figure 4-11. Structure of Wu176.

Wu176 molecule is uncharged and weakly water soluble with absorption maximum at about 580 nm. It is expected to bind to gold through the CN groups. Centrifugation experiments showed that it did bind to gold, but only at a very low concentrations (around 0.3 μM). At these low concentrations, it does not appear to aggregate the nanoparticles; however, no SERS spectrum could be measured, either near the molecular resonance or near the gold plasmon resonance. Apparently, the enhancement is simply too weak. Usually a pretty decent Raman spectrum can be obtained from a strong Raman scatterer in water at a concentration of about 1 μM, even without surface enhancement. So it is a little surprising that no Raman signal at all could be seen from Wu176 on gold at 0.3 μM. It may just not be a very strong Raman scatterer, although it has a fairly large extinction coefficient. The next step was to look at chromophores that should have been better scatterers.

Julolidinemalononitrile (JM) is also known as va138. It proved to be very slightly water soluble. JM has stronger absorbance than Wu176 and its absorption maximum is at about 467 nm (see JM alone in Figure 4-13). Since JM's extinction coefficient is larger, then it should be a better Raman scatterer. And it should show

better SERS enhancements because the CN groups that bind to the metal may be closer to the main conjugated π system of the chromophore. However, JM absorption spectrum changed dramatically upon addition to gold colloid. More specifically, when JM was added to gold nanoparticles, no apparent increase in absorption was seen at characteristic ~ 467 nm; however, absorption around 375 nm was increased (Au and JM spectrum on Figure 4-13). Furthermore, when Au and JM was centrifuged down, JM in supernatant clearly had very different absorption spectrum compared to JM alone in water. This new peak at ~ 375 nm suggests that JM is undergoing some kind of chemical reaction when added to the gold solution. This would have not worked for our study since we need to study one molecule at a time and not a mixture of JM species.

julolidinemalononitrile
(JM) = va138
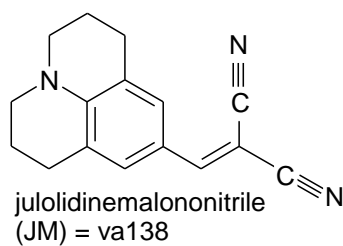
Figure 4-12. Structure of JM.
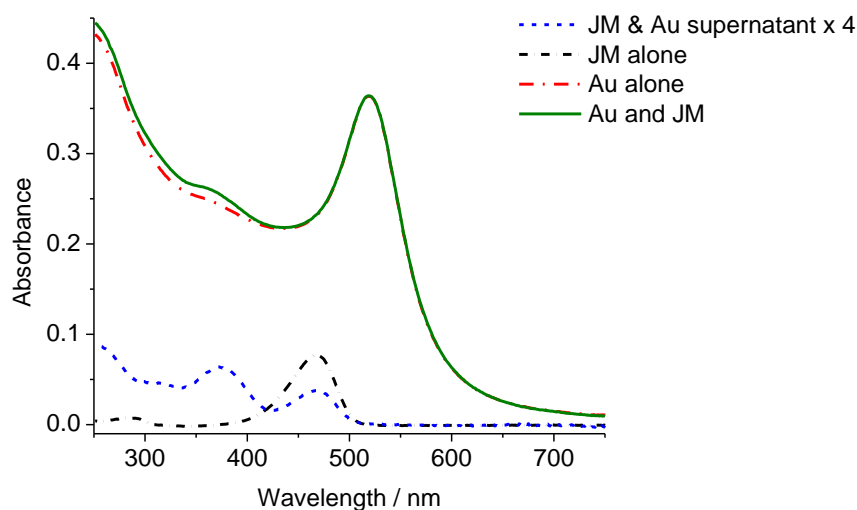
Figure 4-13. Absorption spectrum of JM alone, Au alone, Au and JM solution,

and JM in an Au and JM supernatant times four.

SY41 (also called IDMN) is slightly water soluble. It has absorption maximum around 440 nm. JM's extinction coefficient is also larger, then it should be a better Raman scatterer than Wu176; in fact, Raman spectrum of SY41 in water at concentrations less than micromolar was decent. JM should also show better SERS enhancements because the binding CN groups are closer to the main conjugated π system of the chromophore.
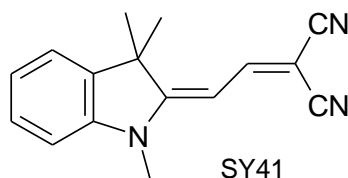
Figure 4-14. Structure of SY41.

However, SY41 did not seem to attach to gold nanoparticles at these small concentration (concentrations corresponding to less than 100 % gold nanoparticle coverage) as judged by the absorption spectrum of the supernatant of the centrifuged SY41 and gold versus absorption spectrum of SY41 alone: at low SY41 concentrations, amount of SY41 in gold-SY41 supernatant appeared to be almost the same as amount of SY41 in a solution of SY41 alone. At higher concentration, SY41 amount in supernatant was considerably smaller than amount of SY 41 in corresponding solution of SY41 alone, suggesting that larger concentrations of SY41 kinetically force it to bind to gold nanoparticles, and then presence of SY41 on gold surface possibly changes the chromophore adsorption to the gold surface. This binding complication would have made our study much more convoluted and, therefore, would have not worked.
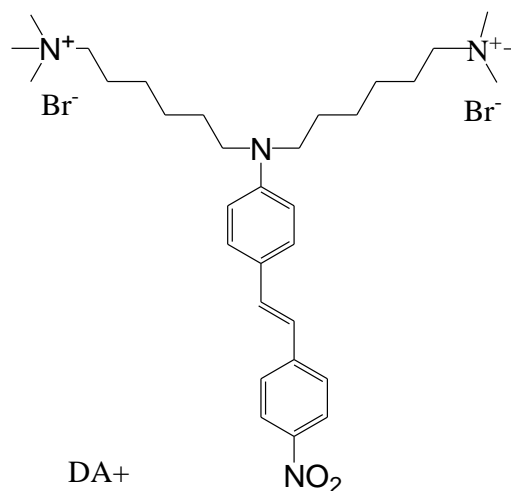
Figure 4-15. Structure of DA+.

DA+ is water soluble. It has a broad absorption maximum around 440 nm. Addition of even small amount of DA+ aggregated the nanoparticles probably due to

two charged groups. This makes DA+ and citrate reduced gold nanoparticle system not suitable for our study.
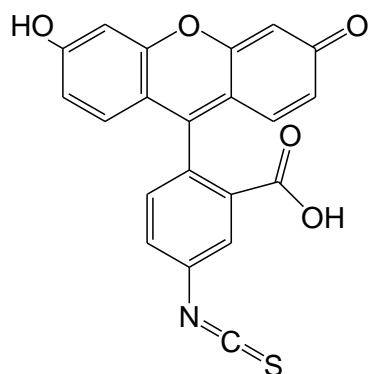
Figure 4-16. Structure of FITC.
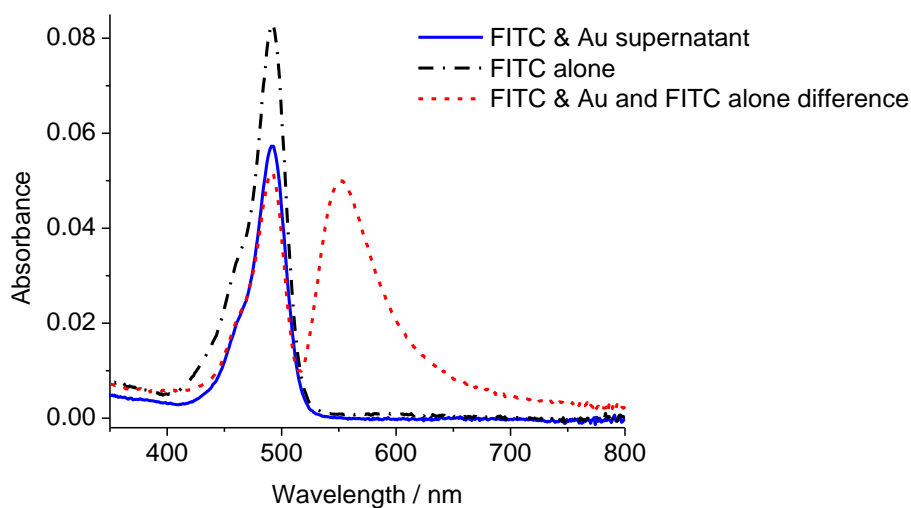
Figure 4-17. FITC alone, supernatant of FITC and Au, and FITC & Au and Au difference.

Fluorescein isothiocyanate (FITC) is an uncharged molecule that adsorbs to gold through the SCN group; therefore, it is less likely to aggregate gold nanoparticles than the cationic dyes. It was found to be water soluble. Its absorption

maximum is around 490 nm. The chromophore did adsorb to the gold nanoparticles at concentrations of 5.5×10^{-7} M as judged from FITC absorption in Au and FITC supernatant versus absorption of FITC alone (Figure 4-17). Interestingly, when Au alone absorption spectrum was subtracted from an absorption spectrum of Au with FITC (FITC & Au and FITC alone difference trace in Figure 4-17), a peak at about 550 nm appeared. In the literature there were two contradicting studies: one reporting that the absorption spectrum of the FITC on silver or gold is almost exactly the sum of the FITC spectra and nanoparticle spectra separately,[60] and one reporting that the sum of the FITC spectra and nanoparticle spectra separately is different than the absorption spectrum of the FITC on nanoparticles.[87] Our results support the latter of the two. The new feature could be due to the chromophore and nanoparticle dipole interactions, to gold nanoparticle aggregation, or to formation of new dye species due to interaction of the chromophore with citrate reduced nanoparticles in the solution. The last is unlikely since collective absorption at 490 nm and 550 nm is larger than the absorption of FITC alone at a corresponding concentration. Also one would expect that if nanoparticle aggregation is occurring, then SERRS signal from a chromophore should be significant. However, when the Raman spectrum of the chromophore alone at these concentrations was taken, no Raman lines were seen. Similarly, when the surface enhanced Raman spectrum of the chromophore at the same concentrations with gold nanoparticles was taken, no Raman lines were seen either. This might suggest that not the aggregation of FITC, but the chromophore and nanoparticle dipole interactions were responsible for the perturbation of the FITC absorption spectrum in the nanoparticle presence. To make the last statement with

certainty, theoretical simulations of FITC dipole and gold nanoparticle dipole interactions are called for. Since we can not get Raman or SERS spectra for FITC and FITC with gold, we needed to look for a better nanoparticle-chromophore system.

4.3 CV
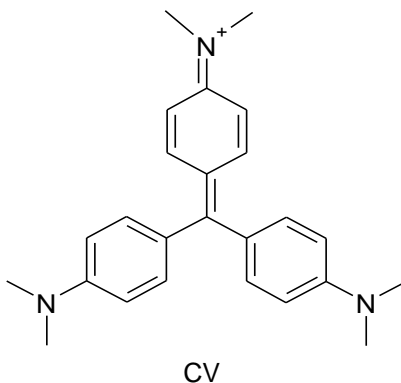
Figure 4-18. Structure of CV.

Crystal violet (CV), a charged, water-soluble chromophore widely used in SERS studies, was tried next. Since it has large molar extinction coefficient of 112,000 $M^{-1}cm^{-1}$ at 590.5 nm in water[78], it is a very good Raman scatterer. Since it is a charged molecule, it should bind to gold surface that is protected by negative citrate ions very strongly. It can be checked by centrifuging down the nanoparticles-chromophore solution and checking the absorption spectrum of the supernatant. As it was described in the DANS-thiol section, if adsorption of the chromophores is strongly favored, than there should be an upper limit of a chromophore concentration under which no chromophores are present in the supernatant, and above which chromophores appears in the supernatant and can be identified by the absorption

spectrum. This concentration, 1.1 µM, was found for CV and was equated to 100 %

gold coverage.
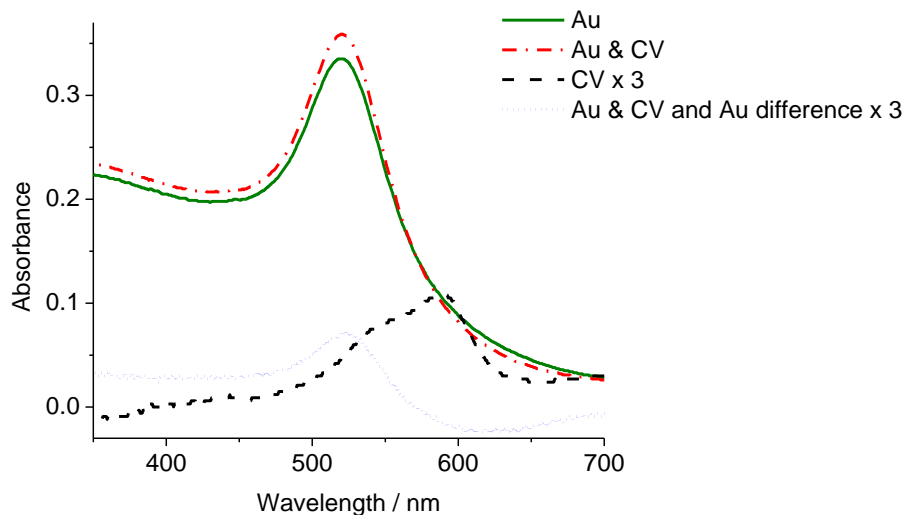
Figure 4-19. Absorption spectrum of Au alone, CV alone times three, Au and CV

solution, and difference of Au & CV and Au alone times three. CV concentration

is 0.3 µM.

As was the case with FITC, spectrum of CV (0.3 µM) in water alone was very

different than the difference of gold nanoparticle & CV solution absorption spectrum

and absorption spectrum of the gold nanoparticles alone (Figure 4-19). Change of the

absorption spectrum of CV in water to the spectrum of the difference could be due to

the chromophore and nanoparticle dipole interactions, to gold nanoparticle

aggregation, or formation of a new dye species. This change of the absorption

spectrum being due to nanoparticle aggregation is unlikely as it would have resulted

in an absorption's red shift instead of the blue shift seen in the difference spectrum

versus CV alone spectrum. Absorption red shift is a well known feature of aggregated

nanoparticles, and it is illustrated in Figure 4-20: progressively more NaCl is added to initially non-aggregated citrate reduced nanoparticles; NaCl disturbs citrate ion layer that protects nanoparticles from coalescing together resulting in reduction of absorption maxima at around 520 nm and a formation of a new feature corresponding aggregated gold nanoparticles at around 680 nm and then progressively at a more red shifted wavelength.
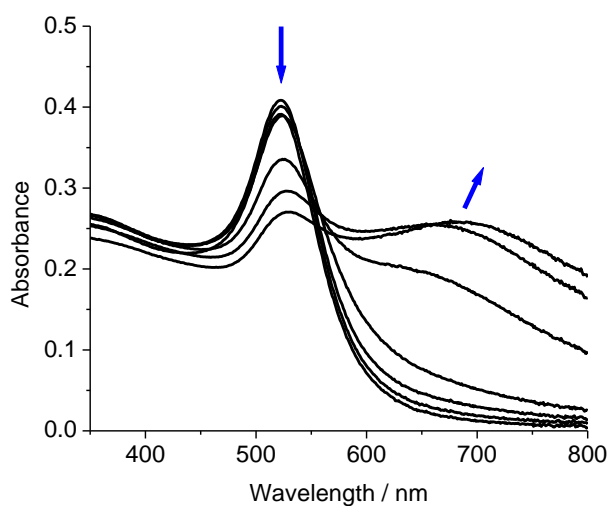
Figure 4-20. Absorption red shift associated with aggregation of nanoparticles.

This same addition of NaCl to initially unaggregated gold nanoparticles can be also followed with dynamic light scattering. The results are shown in Figure 4-21: the chart at the top represents unaggregated citrate reduced nanoparticles and the chart at the bottom represents nanoparticles after NaCl addition.
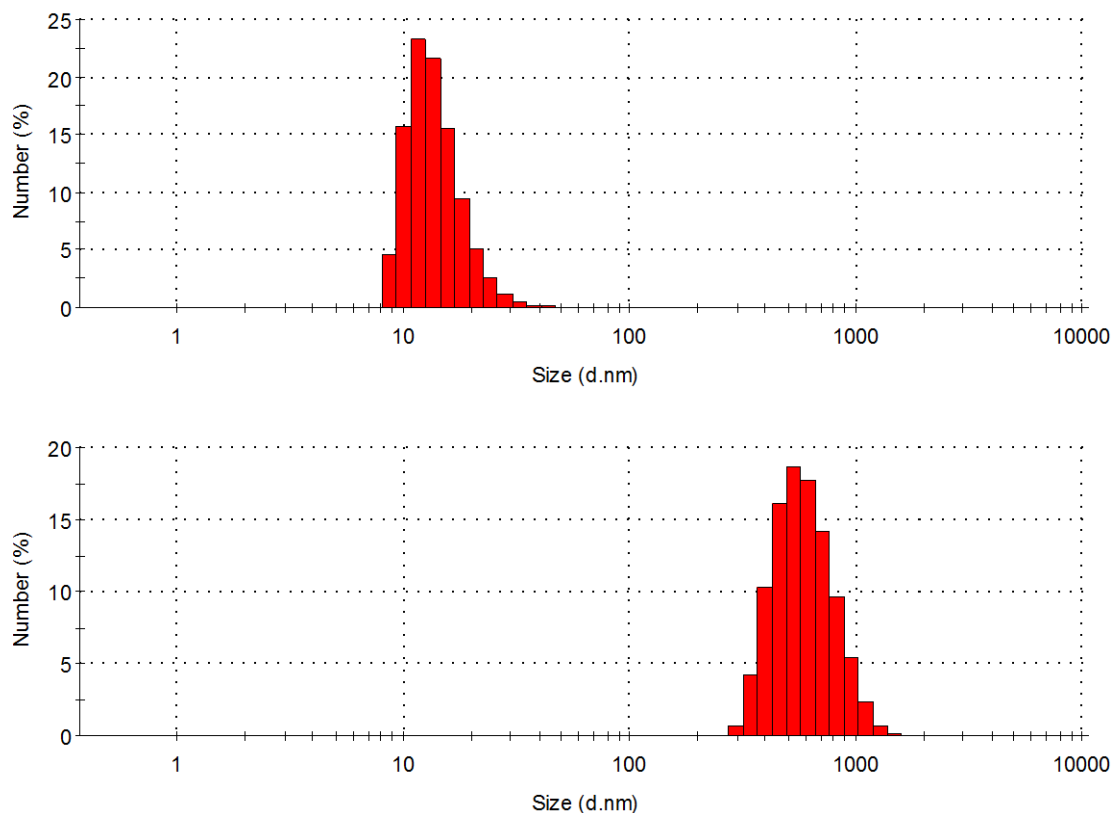
Figure 4-21. Dynamic light scattering results for unaggregated citrate reduced nanoparticles (top) and for aggregated nanoparticles after NaCl addition (bottom).

Due to a charge on the CV molecule, it has a strong tendency to aggregate the nanoparticles. It was possible to find a range of concentrations in which no aggregation was apparent from the absorption spectrum as judged by no appearance of a red shifted difference spectrum after CV addition to the nanoparticles (Figure 4-22). With addition of more CV the characteristic for the "difference" spectrum absorption maximum diminished and was replaced by the absorption maximum at around 600 nm resembling aggregation more than CV only absorption spectrum (CV only spectrum has two of the more narrow distinguishable absorption maxima). The color change due to the suspected aggregation of the nanoparticles was not visible by

eye, but the absorption spectrum suggests the aggregation. The "difference" spectra at the same CV concentrations did slightly vary from run to run, perhaps because it is hard to control the degrees of aggregation once the aggregation starts or because absorbances measured are so minute and are, therefore, somewhat unreliable, but the general trend of ~ 520 nm peak going down and being replaced by ~ 600 nm peak was reproducible.
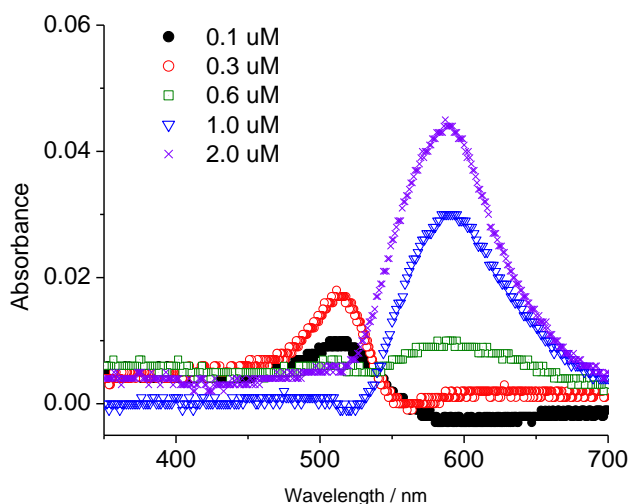
Figure 4-22. Absorption spectra corresponding to "difference" spectra of Au & CV and CV with CV concentrations label on the figure.

SERS spectra could be measured at these concentrations (0.2 to 0.5 μM). If Raman spectra of dye and nanoparticle solution were measured with dye concentrations above this range, then intensity of SERS spectra was not linear with CV concentration. Figure 4-23 illustrates the above statement showing that the intensity of SERS spectra is linear while CV concentrations are under 0.82 μM (referred to as 73 % coverage on the plot). This further suggests that the positive-

going peak at ~ 600 nm in the "difference" spectra with CV concentrations above 0.5 µM was probably due to nanoparticle aggregation. Therefore, further experiments were carried out in the 0.2 to 0.5 µM CV range in attempts to measure SERRS enhancements on unaggregated nanoparticles.
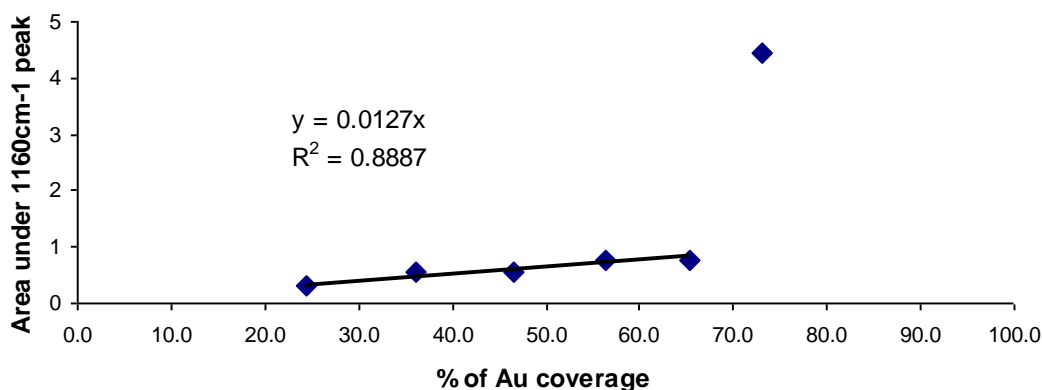
Figure 4-23. Change of area under a CV peak (ratio of area under the 1160cm-1 CV peak to the 1035cm-1 MeOH peak) with the change of percent coverage of Au nanoparticles.

Raman and SERS spectra were collected as a function of excitation wavelength as two different trials (Figure 4-24). Raman cross sections at different excitation wavelengths were calculated using MeOH lines from the internal standard, MeOH, as a reference, and thus excitation profiles were constructed. On the Figure 4-24, unconnected blue circles correspond to the CV in water excitation; red connected circles correspond to the CV & Au nanoparticle solution excitation profile; absorption spectra of Au nanoparticles and CV alone multiplied by 3 for easier viewing are also presented. However, again, as in the case with DANS-thiol, the enhancement factors continued to increase to the red instead of peaking anywhere

near the gold plasmon resonance during the two trials, suggesting aggregation. The aforementioned red shifted peaking of the enhancements, that is usually due to nanoparticle aggregation, was slightly different for the two trials probably due to different extents of nanoparticle aggregation (similar to what have been shown in Figure 4-20 where different amounts of NaCl were added to simulate different extents of nanoparticle aggregation resulting in a formation of a progressively more and more red shifted absorbance).

TEM images (Figure 4-25) also suggest that the crystal violet-bound nanoparticles are more aggregated than the same nanoparticles without chromophores. Obviously TEM images are made of the solutions that have been dried out on the TEM grids and there is an assumption that the substances arrange themselves on the TEM grid in the same way they exists in the solutions. If something appears aggregated on the TEM grids, then there is always a possibility that it was not aggregated in a solution, but probably not the other way around. Therefore, TEM images can not be sole evidence for nanoparticle aggregation, but they could be analyzed in conjunction with other data. In our case, a majority of nanoparticles appear to be unaggregated on the TEM grid; however, there are very few nanoparticles that seem to exist as an aggregated dimer of spheres. One possibility is that CV "arms" attach to two different nanoparticles and bring them close together aggregating the nanoparticles in the process.
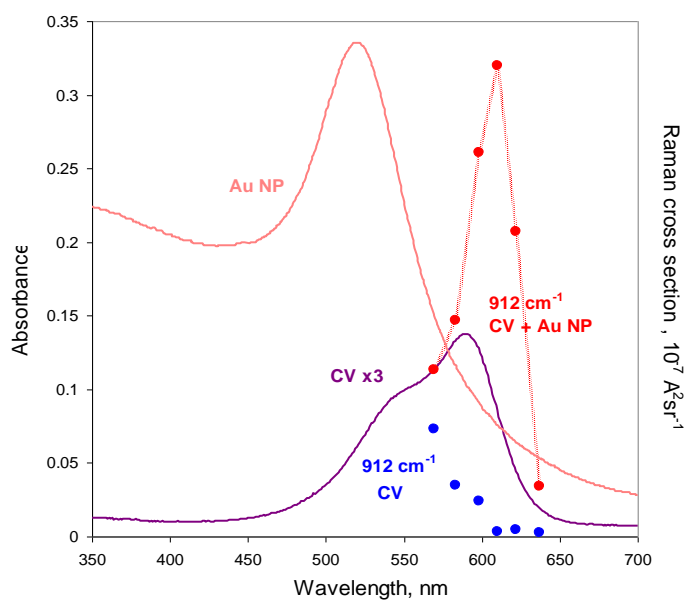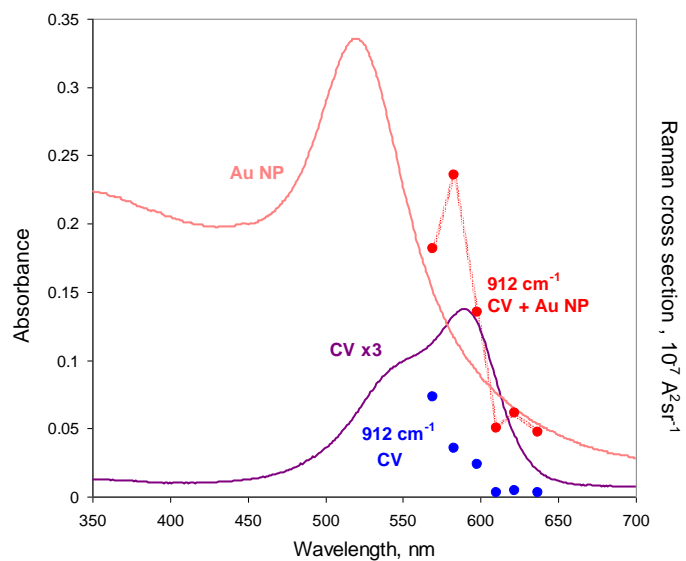
Figure 4-24. Excitation profile of CV alone (blue unconnected circles) and of CV on gold nanoparticles (red connected circles) for the 912 cm⁻¹ peak; and absorption spectra of Au nanoparticles alone and of CV alone times 3. Trial one is above and trial two is below.
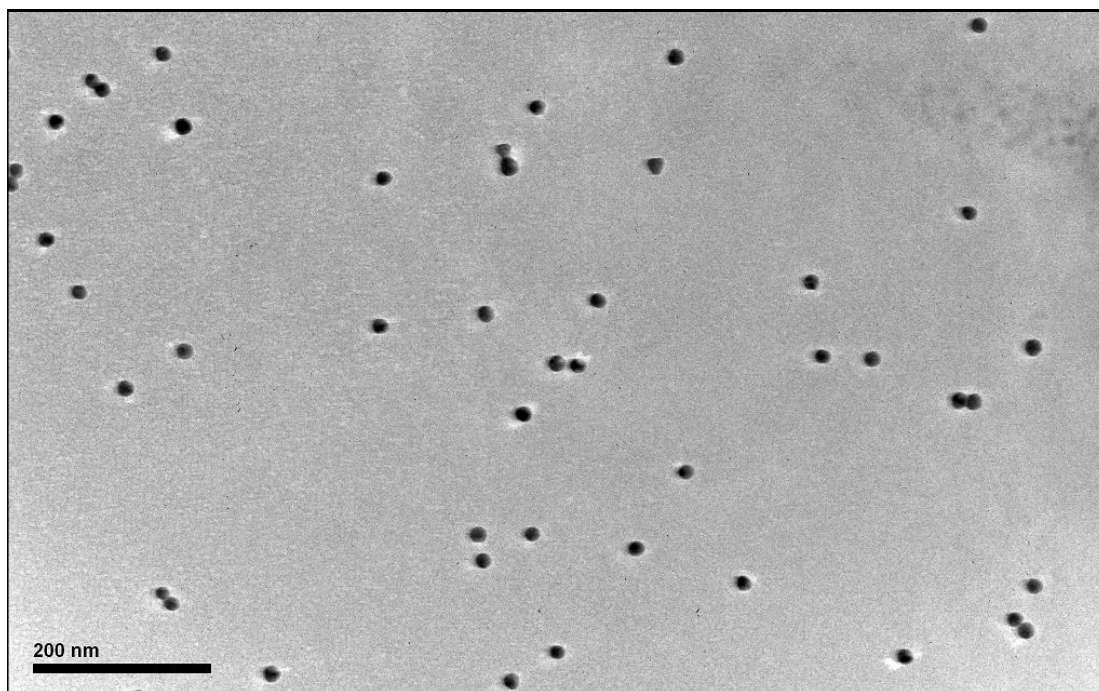
Figure 4-25. TEM images of gold nanoparticles with CV.

5 Summary and Conclusion

The experiment was initially attempted with DANS-thiol bound to citrate-coated gold nanoparticles resuspended in MeOH which caused nanoparticle aggregation. Since DANS-thiol is not soluble in water and the citrate-coated nanoparticles were found to not be stable in methanol, the experiments were done in a 50:50 MeOH:H_2O mixture in which the nanoparticles alone appeared stable and the DANS-thiol bound well to the nanoparticles. However, the chromophore appeared to aggregate the nanoparticles and the absorption difference spectra were not reproducible from run to run. SERS spectra could be measured at surface coverages well under 100%, but the enhancement factors simply increased as the excitation frequency was tuned redder, suggesting aggregation.

We also tried to synthesize organic-soluble nanoparticles and do the experiments in a solvent in which the chromophore was happier, but could not find any combination of preparation method and solvent in which stable nanoparticles could be made and the DANS-thiol would bind to them. We guess that the capping agents used to produce organic solubility bound too tightly to the metal for the DANS-thiol to displace them.

Many dye-nanoparticle systems we tried did not work either due to dyes not adsorbing to nanoparticles, dyes changing to different species in nanoparticle presence, strong dyes' tendency to aggregate the nanoparticles, dyes being not soluble in aqueous solutions and/or presence of a few aggregated nanoparticles (which is too many for our purposes) in colloids of nanoparticles in organic solvents, or because a dye is not a strong Raman scatterer and, therefore, no observable Raman spectrum.

Lastly crystal violet adsorbed to citrate reduced nanoparticles was examined. Crystal violet has a strong tendency to aggregate the nanoparticles. Even though it was possible to find a range of concentrations where absorption spectra did not suggest any nanoparticle aggregation, and where Raman intensities were linear with CV concentrations, Raman excitation profiles do suggest that aggregation of nanoparticles was occurring in the CV and Au solution. Perhaps, aggregation was happening on a very small scale, so it was not distinguishable by straightforward spectroscopic observations. Even though the CV results fell short from what we wanted to accomplish (studying an adsorbed chromophore on a spherical nanoparticle system with no aggregation), there have been very few if any attempts to measure SERRS enhancements on unaggregated nanoparticles. Moreover, there has not been a

study of electronically resonant chromophores and nanoparticles looking at optical absorption, SERRS and resonant Raman spectra concurrently under identical conditions. Our work outlines potential challenges one might face attempting to measure SERRS enhancements on unaggregated nanoparticles and potential ways to deal with some of them.

References

(1) Myers, A. B. Excited Electronic State Properties from Ground-State Resonance Raman Intensities. In *Laser Techniques in Chemistry*; Myers, A. B., Rizzo, T. R., Eds.; Wiley: New York, **1995**; pp 325-384.

(2) Myers, A. B. Resonance Raman Intensity Analysis of Excited-State Dynamics. *Acc. Chem. Res.* **1997**, *30*, 519-527.

(3) Myers, A. B. 'Time-Dependent' Resonance Raman Theory. *J. Raman Spectrosc.* **1997**, *28*, 389-401.

(4) Kelley, A. M. Resonance Raman Intensity Analysis of Vibrational and Solvent Reorganization in Photoinduced Charge Transfer. *J. Phys. Chem. A* **1999**, *103*, 6891-6903.

(5) Myers, A. B. Molecular Electronic Spectral Broadening in Liquids and Glasses. *Ann. Rev. Phys. Chem.* **1998**, *49*, 267-295.

(6) Aroca, R. *Surface-Enhanced Vibrational Spectroscopy;* John Wiley and Sons: West Sussex, England, **2006**.

(7) Atkins, P.; de Paula, J.; Friedman, R. *Quanta, Matter and Change: A Molecular Approach to Physical Change;* Macmillan: **2008**.

(8) Myers, A. B.; Mathies, R. A. Biological Applications of Raman Spectroscopy. In *Resonance Raman Intensities: a Probe of Excited State Structure and Dynamics;* Spiro, T. G., Ed.; Wiley: New York, **1987**; Vol. 2, pp 1-58.

(9) Le Ru, E. C.; Etchegoin, P. G. *Principles of Surface-Enhanced Raman Spectroscopy and Related Plasmonic Effects;* Elsevier: Amsterdam; Boston; Paris [etc.], **2009**.

(10) Stallard, B. R.; Callis, P. R.; Champion, P. M.; Albrecht, A. C. Application of the Transform Theory to Resonance Raman Excitation Profiles in the Soret Region of Cytochrome-c. *J. Chem. Phys.* **1984**, *80*, 70-82.

(11) H. A. Kramers; W. Heisenberg Über Die Streuung Von Strahlung Durch Atome. *Z. Phys* **1925**, *31*, 681.

(12) P. A. M. Dirac The Quantum Theory of Dispersion. *Proc. Roy. Soc.* **1927**, *114*, 710.

(13) Myers, A. B. Resonance Raman Intensities and Charge-Transfer Reorganization Energies. *Chem. Rev.* **1996**, *96*, 911-926.

(14) Myers, A. B.; Mathies, R. A.; Tannor, D. J.; Heller, E. J. Excited State Geometry Changes from Preresonance Raman Intensities: Isoprene and Hexatriene. *J. Chem. Phys.* **1982**, *77*, 3857-3866.

(15) A. Ron Theory of Fluorescence and Raman Near Resonance. *Chem. Phys. Lett.* **1978**, *58*, 329.

(16) Brandsden, B. H.; Joachain, C. J. *Physics of atoms and molecules;* Longman: New York, **1983**; , pp 686.

(17) Hollas, J. M. *Modern Spectroscopy.* John Wiley: Chichester, 1987; .

(18) Albrecht, A. C. On the Theory of Raman Intensities. *J. Chem. Phys.* **1961**, *34*, 1476-1484.

(19) Mortensen, O. S.; Hassing, S. Polarization and Interference Phenomena in Resonance Raman Scattering. *Adv. Infrared Raman Spectrosc.* **1980**, *6*, 1-60.

(20) Champion, P. M.; Albrecht, A. C. On Band Shapes of Electronic Transitions in the Multimode Weak Coupling Limit. *J. Chem. Phys.* **1980**, *72*, 6498-6506.

(21) Tannor, D. J.; Heller, E. J. Polyatomic Raman Scattering for General Harmonic Potentials. *J. Chem. Phys.* **1982**, *77*, 202-218.

(22) Lee, S.; Heller, E. J. Time-Dependent Theory of Raman Scattering. *J. Chem. Phys.* **1979**, *71*, 4777-4787.

(23) Myers, A. B.; Mathies, R. A. Biological Applications of Raman Spectroscopy. In *Resonance Raman Intensities: A Probe of Excited-State Structure and Dynamics;* Spiro, T. G., Ed.; Wiley: New York, **1987**; Vol. 2, pp 1-58.

(24) Sue, J.; Yan, Y. J.; Mukamel, S. Raman Excitation Profiles of Polyatomic Molecules in Condensed Phases. A Stochastic Theory. *J. Chem. Phys.* **1986**, *85*, 462-474.

(25) Heller, E. J.; Sundberg, R. L.; Tannor, D. Simple Aspects of Raman Scattering. *J. Phys. Chem.* **1982**, *86*, 1822-1833.

(26) Moskovits, M. Surface-Enhanced Spectroscopy. *Rev. Mod. Phys.* **1985**, *57*, 783-826.

(27) Kambhampati, P.; Child, C. M.; Foster, M. C.; Campion, A. On the Chemical Mechanism of Surface Enhanced Raman Scattering: Experiment and Theory. *J. Chem. Phys.* **1998**, *108*, 5013-5026.

(28) Moskovits, M. Surface-Enhanced Raman Spectroscopy: A Brief Retrospective. *J. Raman Spectrosc.* **2005**, *36*, 485-496.

(29) Raether, H. *Surface plasmons on smooth and rough surfaces and on gratings.* Springer: Berlin, **1988**.

(30) Kretschmann, E. The Angular Dependence and the Polarisation of Light Emitted by Surface Plasmons on Metals due to Roughness. *Opt. Commun.* **1972**, *5*, 331-336.

(31) Jiang, J.; Bosnick, K.; Maillard, M.; Brus, L. Single Molecule Raman Spectroscopy at the Junctions of Large Ag Nanocrystals. *J. Phys. Chem. B* **2003**, *107*, 9964-9972.

(32) Xu H; Käll M Polarization-Dependent Surface-Enhanced Raman Spectroscopy of Isolated Silver Nanoaggregates. *ChemPhysChem* **2003**, *4*, 1001-5.

(33) Xu, H.; Aizpurua, J.; Käll, M.; Apell, P. Electromagnetic Contributions to Single-Molecule Sensitivity in Surface-Enhanced Raman Scattering. *Phys. Rev. E* **2000**, *62*, 4318-4324.

(34) Brus L. Noble Metal Nanocrystals: Plasmon Electron Transfer Photochemistry and Single-Molecule Raman Spectroscopy. *Acc.Chem.Res.* **2008**, *41*, 1742-1749.

(35) Xu, H.; Aizpurua, J.; Kall, M.; Apell, P. Electromagnetic Contributions to Single-Molecule Sensitivity in Surface-Enhanced Raman Scattering. *Phys. Rev. E-* **2000**, *62*, 4318-4324.

(36) Albrecht, M. G.; Creighton, J. A. Anomalously Intense Raman Spectra of Pyridine at a Silver Electrode. *J. Am. Chem Soc.* **1977**, *99*, 5215-5217.

(37) Fleischmann, M.; Hendra, P. J.; McQuillan, A. J. Raman Spectra of Pyridine Adsorbed at a Silver Electrode. *Chem. Phys. Lett.* **1974**, *26*, 163-166.

(38) Jeanmaire, D. L.; van Duyne, R. P. Surface Raman Spectroelectrochemistry. 1. Heterocyclic, Aromatic, and Aliphatic-Amines Adsorbed on Anodized Silver Electrode. *J. Electroanal. Chem.* **1977**, *84*, 1-20.

(39) Birke, R. L.; Lombardi, J. R. Surface-Enhanced Raman Scattering. Gale, J. D., Ed.; In *Spectroelectrochemistry: Theory and Practice*; Plenum Press: New York, **1988**.

(40) Adrian, F. J. Charge Transfer Effects in Surface-Enhanced Raman Scattering. *J. Chem. Phys* **1982**, *77*, 5302.

(41) Moskovits, M.; DiLella, D. P. In Chang, R. K., Furtak, T. E., Eds.; *Surface Enhanced Raman Scattering*; Plenum Press: New York, **1982**; pp 243.

(42) Creighton, J. A.; Blatchford, C. G.; Albrecht, M. G. Plasma Resonance Enhancement of Raman Scattering by Pyridine Adsorbed on Silver Or Gold Sol Particles of Size Comparable to the Excitation Wavelength. *J. Chem. Soc. Faraday Trans. 2* **1979**, *75*, 790-798.

(43) Jackson, J. D., *Classical Electrodynamics;* Wiley: New York, **1998**.

(44) Messinger, B. J.; von Raben, K. U.; Chang, R. K.; Barber, P. W. Local Fields at the Surface of Noble-Metal Microspheres. *Phys.Rev.B* **1981**, *24*, 649-657.

(45) Le Ru, E. C.; Grand, J.; Félidj, N.; Aubard, J.; Lévi, G.; Hohenau, A.; Krenn, J. R.; Blackie, E.; Etchegoin, P. G. Experimental Verification of the SERS Electromagnetic Model Beyond the $|E|^4$ Approximation: Polarization Effects. *J. Phys. Chem. C* **2008**, *112*, 8117-8121.

(46) Kerker, M. Estimation of Surface-Enhanced Raman Scattering from Surface-Averaged Electromagnetic Intensities. *J. Colloid Interface Sci.* **1987**, *118*.

(47) Yang, W.; Schatz, G. C.; Duyne, R. P. V. Discrete Dipole Approximation for Calculating Extinction and Raman Intensities for Small Particles with Arbitrary Shapes. *The Journal of chemical physics.* **1995**, *103*, 869.

(48) Taflove, A.; Hagness, S. C. In *Computational electrodynamics : the finite-difference time-domain method.* Artech House: Boston, **2005**.

(49) Yin, L.; Vlasko-Vlasov, V. K.; Rydh, A.; Pearson, J.; Welp, U.; Chang, S.; Gray, S. K.; Schatz, G. C.; Brown, D. B.; Kimball, C. W. Surface Plasmons at Single Nanoholes in Au Films. *Appl. Phys. Lett.* **2004**, *85*, 467.

(50) Zhao, L.; Jensen, L.; Schatz, G. C. Pyridine-Ag_{20} Cluster: A Model System for Studying Surface-Enhanced Raman Scattering. *J. Am. Chem. Soc.* **2006**, *128*, 2911-2919.

(51) Jensen, L.; Autschbach, J.; Schatz, G. C.; Finite Lifetime Effects on the Polarizability within Time-Dependent Density-Functional Theory. *J. Chem. Phys.* **2005**, *122:224115,* 1-11.

(52) Inoue, M.; Ohtaka, K. Enhanced Raman Scattering by Two-Dimensional Array of Polarizable Spheres. *J.Phys. Soc. Jpn.* **1983**, *52*, 1457-1468.

(53) Kottmann J; Martin O. Plasmon Resonant Coupling in Metallic Nanowires. *Optics Express* **2001**, *8*, 655-63.

(54) Kottmann J. P.; Martin O. J. Retardation-Induced Plasmon Resonances in Coupled Nanoparticles. *Opt. Lett.* **2001**, *26*, 1096-8.

(55) Aravind, P.; Nitzan, A.; Metiu, H. The Interaction between Electromagnetic Resonances and its Role in Spectroscopic Studies of Molecules Adsorbed on Colloidal Particles or Metal Spheres. *Surface Science* **1981**, *110*, 189-204.

(56) Hao, E.; Schatz, G. C. Electromagnetic Fields Around Silver Nanoparticles and Dimers. *J. Chem. Phys.* **2004**, *120*, 357-366.

(57) Kelley, A. M. A Molecular Spectroscopic View of Surface Plasmon Enhanced Resonance Raman Scattering. *J. Chem. Phys.* **2008**, *128*, 224702.

(58) Schaltz, G. C.; Young, M. A.; Van Duyne, R. P. Electromagnetic Mechanism of SERS*;* Kneipp, K., Moskovits, M. and Kneipp, H., Eds.; In *Surface-Enhanced Raman Scattering: Physics and Applications*; Springer: Berlin, New York **2006**; pp 19-46. http://public.eblib.com/EBLPublic/PublicView.do?ptiID=372829 (Accessed Jan. 4. **2012**)

(59) Liver, N.; Nitzan, A.; Gersten, J. I. Local Fields in Cavity Sites of Rough Dielectric Surfaces. *Chem. Phys. Lett.* **1984**, *111*, 449-454.

(60) Franzen, S.; Folmer, J. C. W.; Glomm, W. R.; O'Neal, R. Optical Properties of Dye Molecules Adsorbed on Single Gold and Silver Nanoparticles. *J. Phys. Chem. A* **2002**, *106*, 6533-6540.

(61) Ipe, B. I.; Thomas, K. G. Investigations on Nanoparticle-Chromophore and Interchromophore Interactions in Pyrene-Capped Gold Nanoparticles. *J. Phys. Chem. B* **2004**, *108*, 13265-13272.

(62) Wiederrecht, G. P.; Wurtz, G. A.; Hranisavljevic, J. Coherent Coupling of Molecular Excitons to Electronic Polarizations of Noble Metal Nanoparticles. *Nano Lett.* **2004**, *4*, 2121-2125.

(63) Kometani, N.; Tsubonishi, M.; Fujita, T.; Asami, K.; Yonezawa, Y. Preparation and Optical Absorption Spectra of Dye-Coated Au, Ag, and Au/Ag Colloidal Nanoparticles in Aqueous Solutions and in Alternate Assemblies. *Langmuir* **2001**, *17*, 578-580.

(64) Makarova, O. V.; Ostafin, A. E.; Miyoshi, H.; R., N. J.,Jr; Meisel, D. Adsorption and Encapsulation of Fluorescent Probes in Nanoparticles. *J. Phys. Chem. B* **1999**, *103*, 9080-9084.

(65) Lim, I. S.; Goroleski, F.; Mott, D.; Kariuki, N.; Ip, W.; Luo, J.; Zhong, C. Adsorption of Cyanine Dyes on Gold Nanoparticles and Formation of J-Aggregates in the Nanoparticle Assembly. *J. Phys. Chem. B* **2006**, *110*, 6673-6682.

(66) Kelley, A. M. A Molecular Spectroscopic Description of Optical Spectra of J-Aggregated Dyes on Gold Nanoparticles. *Nano Lett.* **2007**, *7*, 3235-3240.

(67) Franzen, S.; Folmer, J. C. W.; Glomm, W. R.; O Neal, R. Optical Properties of Dye Molecules Adsorbed on Single Gold and Silver Nanoparticles. *J. Phys. Chem. A* **2002**, *106*, 6533-6540.

(68) Marchi, M. C.; Bilmes, S. A.; Bilmes, G. M. Photophysics of Rhodamine B Interacting with Silver Spheroids. *J. Colloid Interface Sci.* **1999**, *218*, 112-117.

(69) Uwada, T.; Toyota, R.; Masuhara, H.; Asahi, T. Single Particle Spectroscopic Investigation on the Interaction between Exciton Transition of Cyanine Dye J-Aggregates and Localized Surface Plasmon Polarization of Gold Nanoparticles. *J. Phys. Chem. C* **2007**, *111*, 1549-1552.

(70) Wurtz, G. A.; Evans, P. R.; Hendren, W.; Atkinson, R.; Dickson, W.; Pollard, R. J.; Zayats, A. V.; Harrison, W.; Bower, C. Molecular Plasmonics with Tunable Exciton-Plasmon Coupling Strength in J-Aggregate Hybridized Au Nanorod Assemblies. *Nano Lett.* **2007**, *7*, 1297-1303.

(71) Zhao, J.; Jensen, L.; Sung, J.; Zou, S.; Schatz, G. C.; Van Duyne, R. P. Interaction of Plasmon and Molecular Resonances for Rhodamine 6G Adsorbed on Silver Nanoparticles. *J. Am. Chem. Soc.* **2007**, *129*, 7647-7656.

(72) Nerambourg, N.; Werts, M. H. V.; Charlot, M.; Blanchard-Desce, M. Quenching of Molecular Fluorescence on the Surface of Monolayer-Protected Gold Nanoparticles Investigated using Place Exchange Equilibria. *Langmuir* **2007**, *23*, 5563-5570.

(73) Lee, P. C.; Meisel, D. Adsorption and Surface-Enhanced Raman of Dyes on Silver and Gold Sols. *J. Phys. Chem.* **1982**, *86*, 3391-3395.

(74) Bryant, M. A.; Pemberton, J. E. Surface Raman Scattering of Self-Assembled Monolayers Formed from 1-Alkanethiols: Behavior of Films at Gold and Comparison to Films at Silver. *J. Am. Chem. Soc.* **1991**, *113*, 8284.

(75) Evans, S. D.; Ulman, A. Surface Potential Studies of Alkyl-Thiol Monolayers Adsorbed on Gold. *Chem. Phys. Lett.* **1990**, *170*, 462-466.

(76) Hiramatsu, H.; Osterloh, F. E. A Simple Large-Scale Synthesis of Nearly Monodisperse Gold and Silver Nanoparticles with Adjustable Sizes and with Exchangeable Surfactants. *Chem. Mater.* **2004**, *16*, 2509-2511.

(77) Haiss, W.; Thanh, N. T. K.; Aveyard, J.; Fernig, D. G. Determination of Size and Concentration of Gold Nanoparticles from UV-Vis Spectra. *Anal. Chem.* **2007**, *79*, 4215-4221.

(78) Zollinger, H. *Color Chemistry: Syntheses, Properties, and Applications of Organic Dyes and Pigments;* VCH Publications: Weinheim, Federal Republic of Germany; New York, NY, USA, **1987**.

(79) Shoute, L. C. T.; Bartholomew, G. P.; Bazan, G. C.; Kelley, A. M. Resonance Hyper-Raman Excitation Profiles of a Donor-Acceptor Substituted Distyrylbenzene: One-Photon and Two-Photon States. *J. Chem. Phys.* **2005**, *122*, 184508.

(80) Myers, A. B.; Li, B.; Ci, X. A Resonance Raman Intensity Study of Electronic Spectral Broadening Mechanisms in CS_2/cyclohexane. *J. Chem. Phys.* **1988**, *89*, 1876-1886.

(81) Myers, A. B.; Trulson, M. O.; Mathies, R. A. Quantitation of Homogeneous and Inhomogeneous Broadening Mechanisms in Trans-Stilbene using Absolute Resonance Raman Intensities. *J. Chem. Phys.* **1985**, *83*, 5000-5006.

(82) Nafie, L.; Stein, P.; Fanconi, B.; Peticolas, W. L. Angular Dependence of Raman Scattering Intensity. *J. Chem. Phys.* **1970**, *52*, 1584-1588.

(83) Moran, A. M.; Delbecque, C.; Kelley, A. M. Solvent Effects on Ground and Excited Electronic State Structures of the Push-Pull Chromophore Julolidinyl-*n*-N,N'-Diethylthiobarbituric Acid. *J. Phys. Chem. A* **2001**, *105*, 10208-10219.

(84) Haes, A. J.; Zou, S.; Zhao, J.; Schatz, G. C.; Van Duyne, R. P. Localized Surface Plasmon Resonance Spectroscopy Near Molecular Resonances. *J. Am. Chem. Soc.* **2006**, *128*, 10905-10914.

(85) Moran, A. M.; Bartholomew, G. P.; Bazan, G. C.; Kelley, A. M. Effects of a Paracyclophane Linker on the Charge Transfer Transition of 4-Dimethylamino-4'-Nitrostilbene. *J. Phys. Chem. A* **2002**, *106*, 4928-4937.

(86) McQuarrie, D. A.; Simon, J. D., *Physical Chemistry: a Molecular Approach;* University Science Book: Mill Valley, California, **1997**.

(87) Makarova, O. V.; Ostafin, A. E.; Miyoshi, H.; Norris, J. R.; Meisel, D.

Adsorption and Encapsulation of Fluorescent Probes in Nanoparticles. *J. Phys.*

Chem. B **1999**, *103*, 9080-9084.

Project 2:

**Surface-Enhanced Raman Study of the Interaction of
the PEDOT:PSS and P3HT/PCBM Components of
Organic Polymer Solar Cells
with Plasmonically Active Nanoparticles**

1 Theory and Background

The theory of UV-Vis, Raman, Resonant Raman, Surface Enhanced Raman and Surface Enhanced Resonant Raman spectroscopy was presented in the theory chapter for the first project. It is still relevant but will not be duplicated here.

1.1 Organic Polymer Solar Cells

Human-operated nuclear plants can make many people feel uneasy; however, a natural nuclear reactor located far away, the Sun, seems like a promising way to harvest energy for our ever-growing energy consumption needs. Lowering the costs of energy produced by solar photovoltaic cells can make them more mainstream. Lowering solar cell prices can be achieved either by keeping the cost of the existing photovoltaics the same and improving their efficiency or by creating cheaper photovoltaics which may have a lower solar light to electricity conversion efficiency. Currently solar panels on the commercial market have efficiencies between 7% and 18% for amorphous to mono-crystalline silicon technologies; they are rather expensive and many can not afford them. A promising type of low-cost solar cell is made with organic polymers. The production of such a photovoltaic device may be cheaper than existing commercial devices due to the lower costs for the materials and possibly due to a less expensive preparation technique such as "printing" polymers on a substrate in bulk and at room temperature. Another exciting possibility is if a substrate is flexible, like plastic, then such organic polymer solar cells can be affixed to curved surfaces, such as roofs of RVs. Such polymer based solar cells currently

have a maximum efficiency of only about 9% and that is in a lab environment (8.62% efficiency was announced by Konarka Technologies Inc. and an efficiency of 9.2% was reported by Mitsubishi Chemical).[1] An efficiency of 10.6% was reported for solar cells with organic polymers arranged in tandem by a Yang Yang group from UCLA in February 2012.[2]
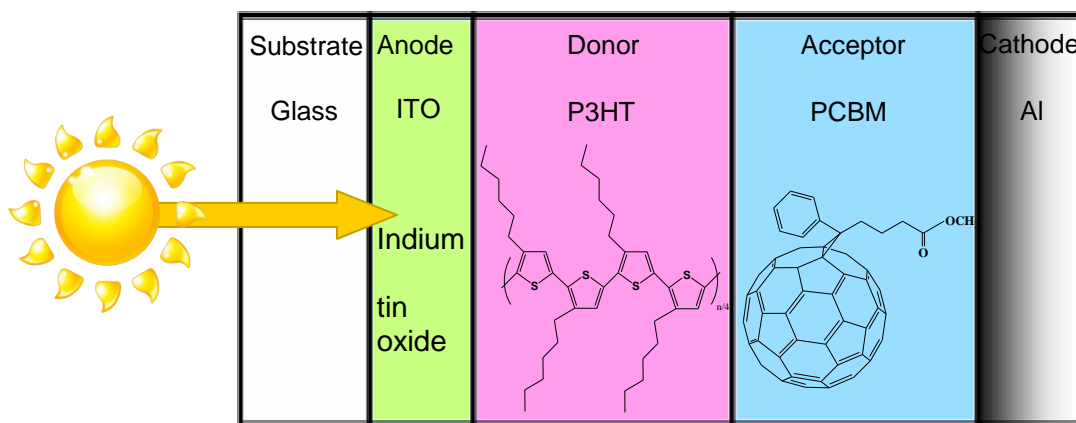
Figure 1-1. Schematic representation of a polymer based organic solar cell.

Typical solar cells consist of a substrate, an anode, an electron donor, an electron acceptor and a cathode (Figure 1-1). In commercial applications, glass or plastic substrates can be used. For spectroscopy, a better suited substrate is glass since it absorbs smaller range of the spectrum and for our studies it is much less Raman active than plastic. For an anode, transparent indium tin oxide (ITO) is used. Light enters through the plastic and through the transparent ITO, and it gets to an active layer, to an electron donor and acceptor. In organic polymer cells, a semiconducting conjugated electron donor, usually a poly(thiophene) or poly(phenylenevinylene) derivative, absorbs the light resulting in excitons, Coulomb-bound electron–hole pairs. The excitons diffuse to get to the electron acceptor. When the excitons gets to

the donor and acceptor interface, the excited polymer can transfer an electron to the electron acceptor, usually a fullerene derivative, and the hole stays behind. The electron acceptor transfers electrons to a cathode, such as aluminum or another low work function metal. A hole gets transferred to the ITO anode.
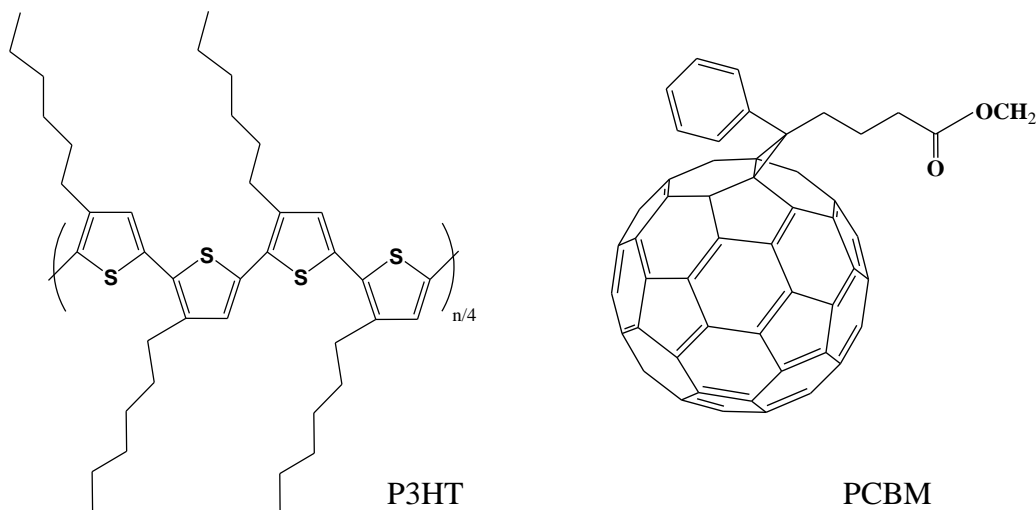
Figure 1-2. Structures of P3HT and PCBM.

We chose to focus our studies on an active layer that is based upon poly(3-hexylthiophene) (P3HT) conjugated polymer electron donor and (6,6)-phenyl-C_{61}-butyric acid methyl ester (PCBM) electron acceptor (Figure 1-2). PCBM is a water soluble fullerene derivative. A device with only one layer of a conjugated polymer would not make an efficient solar cell,[3] since separation of a Coulomb-bound electron-hole pair is inefficient at the conjugated polymer and cathode electrode. An exciton would dissociate more efficiently at the interface between donor and acceptor in a bilayer device (Figure 1-3). In addition, since the exciton diffusion length in conjugated polymers are only few nanometers,[4-6] more efficient organic solar cells have a bulk heterojunction geometry where electron donors and acceptors phase

separate and exist near each other as interpenetrating networks.[7-10] Power conversion efficiencies for such solar cells based on P3HT and PCBM were reported of about 5%.[11-14]
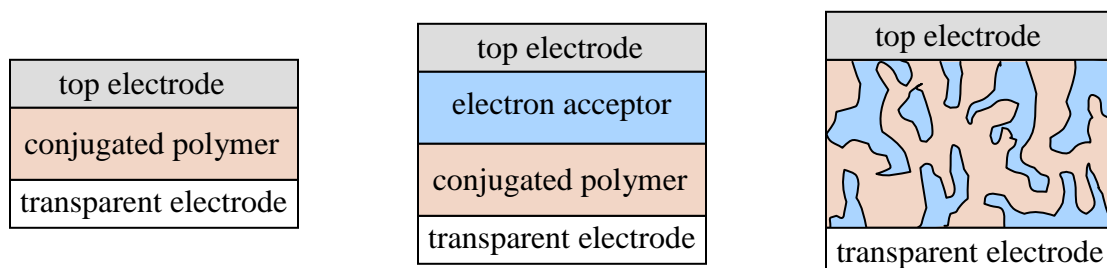
Figure 1-3. The device structures of OPV cells. Left: single layer OPV cell; middle: bilayer OPV cell; right: bulk heterojunction OPV cell.

Some of the better performing solar cells oftentimes have other additional components such as optical spacer layers between the anode and the active layer[11, 15] and a polyelectrolyte layer such as   poly(3,4-ethylenedioxythiophene):polystyrene-sulfonate (PEDOT:PSS) shown in the Figure 1-4.[16-18] The purpose of the PEDOT:PSS is to planarize the ITO surface, to improve the hole transfer from the electron donor to the ITO, and to prevent electron leakage from the electron acceptor to the ITO.

There are quite a few areas that need to be addressed with regards to making organic solar cells more efficient. These areas include: absorption of a wider part of the spectrum; improvement of exciton diffusion length; avoiding electron and hole recombination; hole mobility in the electron donor; charge transfers to the electrodes; and stability of organic materials.
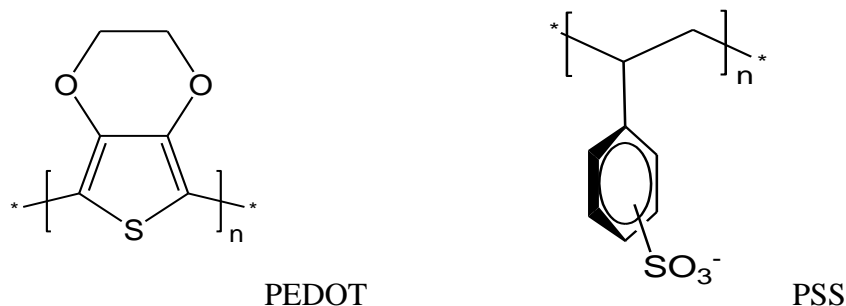
Figure 1-4. Structures of PEDOT and PSS.

There have been a large number of papers reporting solar cell efficiency improvements by 15-70% through incorporation of metals with nanoscale features that can support plasmon resonance.[19-38] However, there have been at least two papers reporting no such enhancement,[39, 40] and, probably, there is a large body of unpublished negative results out there. Plasmon resonance of nanoscale particles or features was discussed in the first project.

The most common explanation for solar cell efficiency enhancement by incorporation of nanoscale features is plasmonic enhancement of light absorption.[41-44] Large near fields can increase light absorption by the conjugated polymers if absorptions of a polymer and nanoparticles overlap.[19, 23, 24, 28, 31, 34, 36, 38] Nanoparticles' absorption band is wider than absorption band of conjugated polymers; therefore, nanoparticles collect wider ranges of light that result in surface plasmon resonance of the nanoparticles.[41] Surface plasmons can be thought of as oscillating multipoles that radiate energy nearby. Thus, one might picture nanoparticles as antenna, collecting greater fraction of solar spectrum and focusing radiation in nearby regions. Even if nanoparticle plasmon resonance is over a region that is broader than the conjugated

polymer's absorption band, as long as the conjugated polymer absorbs in that region just slightly, the conjugated polymer would be affected by the greatly increased electromagnetic radiation around the nanoparticles. In addition, optical effects of scattering nanoparticles can increase optical path length within the active layer giving greater probability for the exciton creation. Depending on nanofeatures and device geometry, metals can have a waveguiding effect.[45, 46] Large local near fields around the nanoparticles might improve exciton dissociation probability;[27, 28, 47] however, they can also increase electron and hole recombination, which is obviously not desired.

There are other roles that nanoparticles might play in increasing solar conversion efficiencies. Nanoparticles, possibly, can act as charge carriers, and, therefore, they might increase charge mobility through the active layer to corresponding electrons.[31, 32, 34, 48] Nanoparticles can improve charge transfer at the electrodes.[26, 35] Organic polymers can possibly chemisorb to nanoparticles, resulting in their excitonic interaction[49] or in, as discussed in SERRS theory, charge transfer interactions,[50-52] which can change polymer properties drastically by changing charge distributions on the molecule or by changing a molecule into a different species.[53] Also dipoles or multipoles on the nanofeatures can interact with dipole moments of surrounding molecules resulting in a change of optical properties of the molecules. This could result in short circuit current changes and in changes of fill factor for the solar cell. There have been reports that incorporation of magnetic nanoparticles could provide a weak magnetic field which could improve solar cell efficiencies by

improving diffusion length of the one type of excitons.[54, 55] Nanoparticles can have even indirect effects such as morphology change of the materials.

2 Motivation and Goals

As mentioned above, there are a lot of articles reporting solar cell efficiency improvements, and some papers disproving them. What is perplexing, is that different researchers working with promising organic polymer solar cells based on P3HT/PCBM reported that incorporation of metallic nanofeatures in various locations improve solar cell efficiencies: when the metal is on the other side of the substrate from ITO,[22] right next to ITO,[21, 27] spaced from the ITO by a polyelectrolyte layer,[23] mixed in with the PEDOT:PSS coating the ITO electrode,[28] used as a substitute for PEDOT with polystyrene,[26] mixed with the conducting polymer layer[25, 48] (no enhancement of efficiency was also reported for nanoparticles mixed with the conducting polymer layer)[39], or deposited between the conducting polymer and the cathode (Figure 2-1).[24] Also, both in situ deposited thin metal films and separately synthesized nanoparticles or fabricated nanostructures are reported to work. From the large quantity of papers each reporting incorporation of metal nanofeatures in different locations of the solar cell and reporting solar conversion efficiency enhancements (see schematic summary in Figure 2-1), it seems like nanoparticles can be incorporated virtually anywhere in the photovoltaic to achieve efficiency increase, which is very confounding. Strong near fields from surface plasmons extend only a few nanometers,[56, 57] and they drop one order of magnitude within 2-3 nm.[58] If these strong near fields are the key for the efficiency enhancement, then their influence

should not persist through the substrate and PEDOT:PSS to the active layer, or even just through the 20-40 nm PEDOT:PSS layer[21, 23, 59] to the active layer.
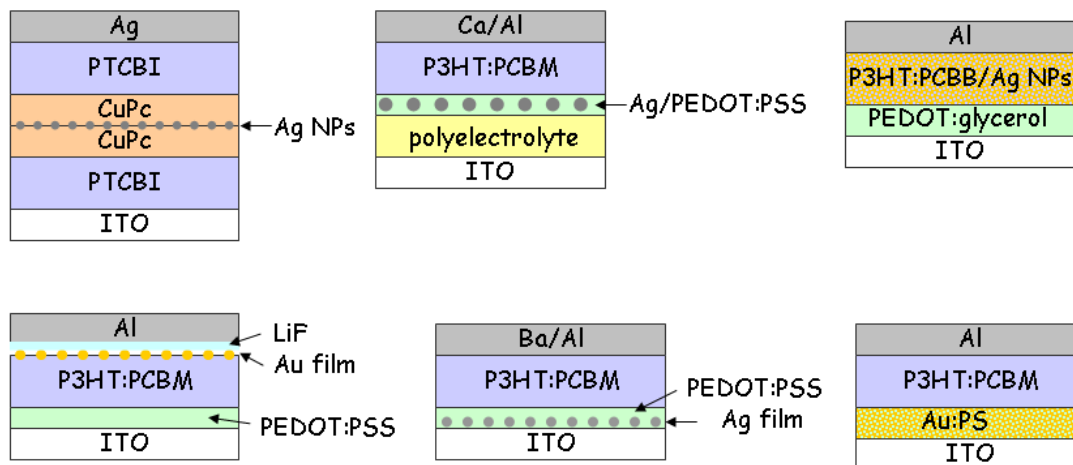
Figure 2-1. Cartoon representations (not drawn to scale) of some of the different geometries in which metal films or nanoparticles have been incorporated into organic solar cells to enhance efficiency. (Figure courtesy of A. M. Kelley)

Surface plasmons are also exploited in SERS, as was described in the theory chapter for the first project. Therefore, utilizing Raman, SERS and UV-Vis spectroscopies, we can study an organic polymer solar cell based on P3HT:PCBM bulk heterojunction layer and with incorporation of different kinds of nanoparticles in different areas of the cell where their incorporation was reported to enhance cell efficiencies. In the research literature, variations of basic layers with different thicknesses were used or additional layers were incorporated as summarized in Figure 2-1; we can study one system prepared consistently varying only types and positions of nanoparticles. Figure 2-2 schematically represents a solar cell and locations for

possible incorporation of nanoparticles somewhat comparable to locations in Figure 2-1.
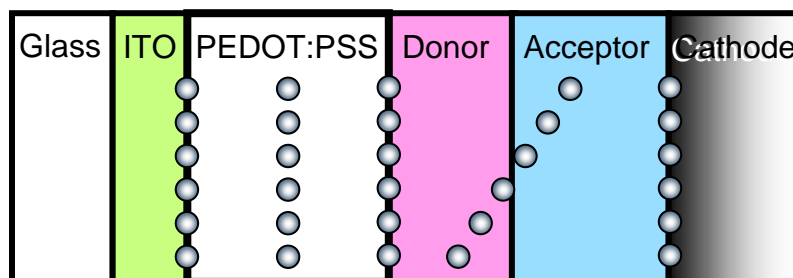
Figure 2-2. Cartoon representations (not drawn to scale) of where we can incorporate nanoparticles into an organic solar cell consistently.

UV-Vis spectroscopy can be used to study changes in organic materials' spectra with metal nanoparticles and without metal nanoparticles presence. Even this aspect seems to be ambiguous in the literature. There has been a report on P3HT and gold nanoparticles showing that the sum of the extinction spectra of P3HT and of gold is the same as the extinction spectrum of P3HT and gold nanoparticles blended together.[60] The last report makes sense since optical spectra of organic chromophores in nanoparticle presence was reported to not be greater than the sum of the absorbances of the chromophores and nanoparticles alone.[61-67] However, there are some articles that report enhancements of the optical absorption spectrum of organic component(s) in presence of metal nanoparticles.[19, 31] Thus we can use UV-Vis spectroscopy to study optical absorption of organic materials with and without metallic nanoparticles.

SERS studies have been performed on organic polymer solar cell components[68-71] and on other conjugated polymers,[72-75] however, associated enhancements of photovoltaics have not been considered. Since plasmon resonance

does not extend far, SERS can essentially zoom into the closest regions to the nanoparticles. P3HT, PCBM and PEDOT have rich Raman spectra with intensities and frequencies being sensitive to redox states, chain conformations and electron delocalization.[53, 69, 71, 74, 76-82] Thus we can use SERS to probe chemical structure and bonding of the organic materials that are closest to the nanoparticles, and we can place nanoparticles at different locations or interfaces within the solar cell or solar cell components so that we can work out if there is a selective segregation of a donor or an acceptor at the interfaces and to probe for chemical or morphological changes at the interfaces.

Moreover, we can employ resonant Raman spectroscopy by choosing excitation wavelengths near molecular resonance with allowed electronic transitions for the organic components of the solar cell. Resonance Raman spectroscopy could give an insight into excited-state molecular structure and photophysics. Since different organic components and their corresponding redox species have electronic resonances at different wavelengths, then this leads us to selectively study those molecules that absorb at chosen excitation wavelengths.

Finally, we can compare resonant or non-resonant Raman spectra with SERS or SERRS spectra to calculate Raman signal enhancements associated with proximity to metallic nanoparticles. We can collect SERS or SERRS data at different wavelengths, and then we can construct Raman excitation profiles as a function of excitation wavelength. We can do the same for the components without nanoparticles From the excitation profiles and extinction spectra we can calculate Raman enhancement factors as a function of excitation wavelength (Equation 1-32 in the first

project of this dissertation) which we can try to correlate with solar cell efficiency enhancements.

3 Experimental and Computational Methods

3.1 PEDOT:PSS

PEDOT:PSS was obtained from Clevios (type P VP AI 4083, OLED grade) and was deposited on either glass coverslips (Fisherbrand) or ITO-coated glass (Delta Technologies). All samples containing metal nanoparticles, and the metal-free samples used for determination of SERS enhancement factors, were prepared by spin-coating, 5 seconds at 500 rpm followed by 30 seconds at 1500 rpm. Two layers of PEDOT:PSS, each expected to have a thickness of 50-80 nm based on the conditions used,[83, 84] were spin-coated on top of each other to provide a thicker sample. PEDOT:PSS samples without metal nanoparticles were also prepared by drop-coating in order to produce thicker samples giving stronger Raman signals. All samples were then heated for 15 minutes at ~110°C. In place of the light-absorbing conducting polymer blend used in solar cells, the PEDOT:PSS was covered with a layer of polystyrene (PS; Sigma-Aldrich, average MW 35000) spin-coated from toluene. For experiments on PSS alone, poly(sodium 4-styrene sulfonate) was purchased from Sigma-Aldrich (MW 70,000, 30 wt. % solution in water) and was either spin-coated or drop-coated onto glass slides, with or without a covering layer of PS.
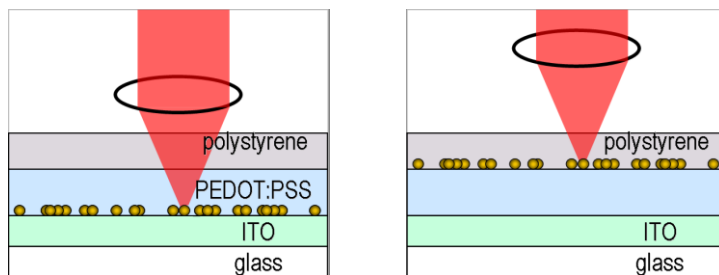
Figure 3-1. Left: silver or gold nanoparticles are incorporated between the ITO and the PEDOT:PSS layers. Right: silver or gold nanoparticles are deposited on top of the PEDOT:PSS.

Gold and silver nanoparticles were synthesized in aqueous solution through the standard citrate reduction method.[85] The gold particles had diameters of 15 ± 2 nm based on transmission electron microscopy (TEM) images, and an absorption maximum of 520 nm in water. The silver particles had diameters of 46 ± 11 nm by TEM and an absorption maximum of 416 nm. Note that aggregation shifts the plasmon resonances, and the optical properties of the dried nanoparticle films used in our experiments may be considerably different from those of the particles in aqueous suspension. Gold nanoparticles were centrifuged to concentrate them; silver nanoparticles were gravity concentrated. For the "metal on bottom" configuration the nanoparticles were applied to the substrate with a dropper, allowed to dry in air, and heated for 10 min at ~100°C. Then the PEDOT:PSS and PS layers were spin-coated as above. In a second preparation method, "metal on top", the PEDOT:PSS was spin-coated and annealed first, then the nanoparticles were applied to the surface of the PEDOT:PSS, dried and heated at ~100°C, and finally the PS layer was applied. Figure 3-1 illustrates the two sample configurations prepared.

Neutral PEDOT was generated by reduction of the as-received PEDOT:PSS with hydrazine as described in ref. 86, followed by spin-coating onto glass with or without nanoparticles in the same manner as for the as-received PEDOT:PSS.

Excitation for Raman spectroscopy was provided by either a Coherent Innova 90C-5 argon-ion laser (457.9 and 514.5 nm) or helium-neon lasers (543 and 632.8 nm). Excitation power at the sample was 0.2 - 0.3 mW. Two different Raman detection setups were employed. The majority of the data presented were obtained on a macro-sampling system[87] which uses a 20 mm focal length lens to focus the excitation light onto the sample and collects the scattering in a ~135° backscattering geometry with a condenser lens. The Raman scattering was passed through a long-pass filter, dispersed with a Spex 500M 0.5 m single spectrograph, and detected with a Roper Scientific Spec 10:100B liquid nitrogen cooled, back-illuminated CCD providing >50% quantum efficiency from 400-850 nm. At the slit width used (100 µm), spectral resolution was 3.4 cm^{-1} at 632.8 nm, 5.5 cm^{-1} at 514.5 nm, and 7.0 cm^{-1} at 457.9 nm. Some data were also obtained with a Jobin-Yvon T64000 Raman microscope system consisting of a 0.64-m triple spectrograph coupled to a confocal Raman microprobe based on an Olympus BX-41 microscope with an Olympus MPLFL100X objective. The much smaller focal volume of this system caused light-induced changes in the SERS spectra as discussed below. Spectra were corrected for the system sensitivity using a broadband light source.[88] Fluorescence backgrounds were removed using GRAMS/AI 7.02 (Thermo Galactic). The Raman spectra were calibrated in frequency by using the Raman bands of cyclohexane or polystyrene. Reported peak frequencies are the apparent maxima (or, for shoulders, inflection

points) of the spectra as obtained and were not determined through any peak-fitting algorithm. The reported frequencies may, therefore, be slightly distorted by peak overlap. Optical absorption spectra were obtained on a Cary 50 UV-VIS spectrophotometer.

Density functional theory calculations were performed using the B3LYP hybrid functional with the 6-311g(d,p) basis as implemented in Gaussian 03.[89] No scaling factor has been applied to the reported frequencies.

[The above section is reprinted with permission from Stavytska-Barba, M.; Kelley, A. M. Surface Enhanced Raman Study of the Interaction of PEDOT:PSS with Plasmonically Active Nanoparticles. *J. Phys. Chem. C* **2010**, *114*, 6822-6830. Copyright 2010 American Chemical Society.]

3.2 P3HT/PCBM

Samples with spherical citrate reduced metal nanoparticles. PEDOT:PSS was obtained from Clevios (type P VP AI 4083, OLED grade) and was deposited on either cleaned glass coverslips (Fisherbrand) or cleaned ITO-coated glass (Delta Technologies) by spin-coating at 500 rpm for 5 s followed by 1500 rpm for 30 s. In order to increase the weak Raman signals from the samples without metal nanoparticles, several layers of PEDOT:PSS were spin-coated on top of each other to provide a thicker sample. Under the conditions used, each layer of PEDOT:PSS is expected to be 50-80 nm thick.[83, 84] The samples were then heated for 15 minutes at ~110°C.

In samples not containing a PEDOT:PSS layer, P3HT/PCBM was deposited either on cleaned glass or on cleaned ITO-coated glass. P3HT and PCBM were obtained from Rieke Specialty Polymers and Aldrich, respectively. P3HT and PCBM were dissolved in chlorobenzene, each at 10 mg/mL, and spin cast at 2000 rpm for 60 seconds. The samples were thermally annealed on a digital hotplate at 140°C for 10 minutes.
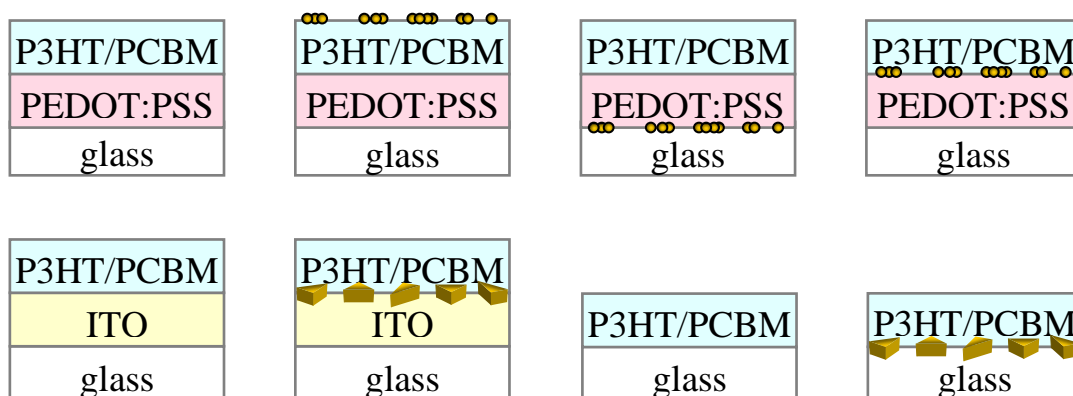
Figure 3-2. Top: Schematic of samples prepared with 15 nm spherical Au nanoparticles or 40-55 nm spherical Ag nanoparticles. Bottom: Schematic of samples prepared with silver nanoprisms.

Gold and silver nanoparticles were synthesized in aqueous solution through the standard citrate reduction method.[85] A TEM image of the resulting spherical gold nanoparticles is presented in Figure 3-3. The nanoparticles were centrifuged to concentrate them, resuspended in a minimum volume of water, applied with a dropper, allowed to dry in air, and then heated to 100°C for 10 minutes. The extinction spectra of the nanoparticles in colloidal suspension have maxima at about 416 nm for silver and 520 nm for gold. These spectra are greatly broadened and red-

shifted by aggregation in the dried films. Several different configurations of PEDOT:PSS, P3HT/PCBM, and nanoparticles were prepared as shown in Figure 3-2.
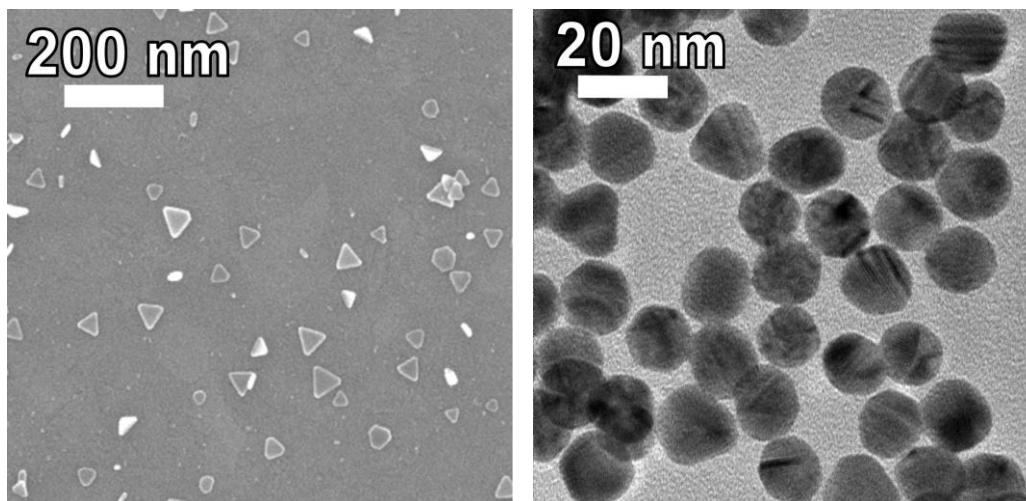
Figure 3-3. Left: SEM of representative Ag nanoprisms; Right: TEM of Au nanospheres.

Samples with silver nanoprisms. Silver nanoprisms were synthesized via photoinduced conversion with pH control.[90, 91] Figure 3-3 shows a representative SEM image. The nanoprisms were 11-12 nm thick with side lengths ranging from 27-40 nm; changing the length over this range shifts the plasmon resonance from about 440 to 550 nm. The nanoprisms were coated with a layer of 1:1 P3HT/PCBM having a thickness of about 35 nm. Self-assembly of the silver nanoprisms and polymer film processing were performed as described in ref. 30.

Optical absorption spectra were obtained on a Cary 50 UV-Vis spectrophotometer and an Agilent 8453 UV-Vis diode array spectrometer.

Nanoparticles were imaged on a JEOL JEM-2011 TEM and on a field emission scanning electron microscope (FEI Sirion SEM).

Excitation for Raman spectroscopy was provided by either a Coherent Innova 90C-5 CW argon-ion laser (363.8, 457.9, 488 and 514.5 nm) or helium-neon lasers (543.5, 612 and 632.8 nm). Two different Raman detection setups were employed.

Spectra of silver nanoprism samples were obtained with a Jobin-Yvon T64000 Raman microscope system consisting of a 0.64-m triple spectrograph coupled to a confocal Raman microprobe based on an Olympus BX-41 microscope with an Olympus MPLFL100X objective (for visible excitation) or 40X UV objective (for near-uv excitation). The detector was a UV coated, back illuminated, liquid nitrogen cooled CCD with > 50% quantum efficiency from 220-850 nm. Spectral resolution was better than 2 cm^{-1} for 632.8 nm excitation and about 4 cm^{-1} for 457.9 and 363.8 nm excitations. Excitation power at the sample was 0.2-0.3 mW and the microscope stage was used to translate the sample along a line during data collection to average over the heterogeneous distribution of nanoprisms and to avoid heating or photochemical damage. Both the Raman and the fluorescence intensities of stationary samples exposed to air decayed rapidly with time, but scanning the samples under the excitation beam prevented this decay. The measured SERS intensities were linear with laser power from 0.08 to 0.24 mW, indicating negligible photodegradation.

Spectra of samples with silver and gold nanospheres were obtained on a macro-sampling system which uses a 20 mm focal length lens to focus the excitation light onto the sample and collects the scattering in a ~135° backscattering geometry with a condenser lens. The Raman scattering was passed through a long-pass filter,

dispersed with a Spex 500M 0.5 m single spectrograph, and detected with a Roper Scientific Spec 10:100B liquid nitrogen cooled, back-illuminated CCD providing >50% quantum efficiency from 400-850 nm. At the slit widths used, spectral resolution was about 7 cm^{-1} at 632.8 nm excitation and 14 cm^{-1} at 457.9 nm.

For each sample and at each excitation wavelength, four to ten spectra with 60-360 s accumulation times were collected and averaged. The raw spectra were divided by the spectrum of a broadband light source to remove intensity fluctuations due to pixel-to-pixel sensitivity variations and etaloning of the CCD at longer wavelengths. Fluorescence backgrounds were removed using Microcal Origin 6.0. The Raman spectra were calibrated in frequency by using the Raman bands of cyclohexane. Areas under Raman peaks were determined using the GRAMS/32 (Galactic Industries) curve fitting algorithm to fit mixed Gaussian-Lorentzian peak profiles.

The experimental SERS enhancement for each line at each excitation wavelength was calculated as the integrated area for the P3HT (or PCBM) peak in the presence of nanoparticles divided by that in the absence of nanoparticles after correcting for any differences in accumulation time. The theoretical SERS enhancement F, is given by standard electromagnetic theory as it was discussed in theory portion of the first project:[92]

$$F \approx \left| E(\omega_{Laser}) / E_0(\omega_{Laser}) \right|^2 \left| E(\omega_{Scatt}) / E_0(\omega_{Scatt}) \right|^2 \qquad \textit{(3-1)}$$

where $E_0(\omega)$ is the incident electric field at ω and $E(\omega)$ is the field in the presence of the metal. F depends on the position and orientation of the scattering molecule relative to the metal surface and to the polarizations of the incident and scattered

photons. The expected frequency dependence of the enhancement may be approximated as[92]

$$F = G * A\left(\omega_{Laser}\right) A\left(\omega_{Scatt}\right) + 1 \qquad\qquad (3\text{-}2)$$

where $A\left(\omega_{Laser}\right)$ and $A\left(\omega_{Scatt}\right)$ are the measured plasmon extinction profiles at the excitation and emission frequencies, respectively, and G is a scaling factor. We have added the factor of 1 to the enhancement profile as it is usually defined in order to obtain the physically correct result that F approaches unity far from any plasmon resonance.

[Parts of the above section are reprinted with permission from Stavytska-Barba, M.; Kelley, A. M. Plasmonic Enhancement of Raman Scattering from the Organic Solar Cell Material P3HT/PCBM by Triangular Silver Nanoprisms. *J. Phys. Chem. C* **2011**, *115*, 20788-20794. Copyright 2011 American Chemical Society.]

4 Results and Discussion

4.1 PEDOT:PSS

In many studies that report the improvement of organic polymer solar cell efficiencies by incorporation of metal nanostructures, metal nanoparticles are in direct contact with the PEDOT:PSS supportive layer. Charges get created in the active layer and the PEDOT:PSS layer helps holes to get to the ITO anode. It is surprising that the presence of nanoparticles separated from the active layer would have an effect on the active layer thereby influencing the photovoltaic efficiency. Thus, the first part of this project focuses on incorporation of metal nanoparticles around the supportive

layer first to study possible effects of metal nanoparticles on PEDOT:PSS. Silver and gold nanoparticles influence is studied by incorporation of nanoparticles in two different geometries: between the ITO and the PEDOT:PSS layers; and on top of the PEDOT:PSS. To protect PEDOT:PSS from the environment, polystyrene (PS) is used instead of what would have been the light absorbing, charge transporting active layer and the cathode in a complete photovoltaic cell.

In the supportive layer PEDOT:PSS, PEDOT is the species that conducts the positive charges to the anode. PEDOT prepared by polymerization of EDOT monomers is a brittle solid and as such cannot be readily incorporated into solar cells as thin layers. PSS is used to stabilize and disperse PEDOT as an aqueous colloidal solution. Chemical structures of PSS and PEDOT are presented in Figure 1-4. This colloidal solution can be readily spin-coated and dried to form highly transparent insoluble thin films that are highly conductive.[93] The spin-coated film consists of 10-50 nm conductive PEDOT particles separated by insulating PSS layers.[16, 18, 94, 95] The PEDOT:PSS films are insoluble and are very stable in the atmosphere, however the conductivity of the films is degraded by the UV radiation due to photooxidation.[96]
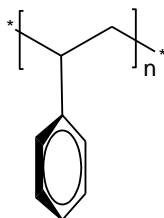
Figure 4-1. Structure of PS.

PS and PSS do not absorb much of the visible part of the electromagnetic spectrum, so they do not attenuate the light that is intended for the absorption in the active layer to ultimately create charges. At the same time, since PS and PSS do not absorb much of the visible light, neither would be on resonance with laser wavelengths that are employed in these experiments (457.9, 514, 543 and 632.8 nm), resulting in weak Raman lines. The structure of PS is shown in Figure 4-1. Raman spectra of PS and PSS thick films are presented in Figure 4-2; thick films were used to maximize the signal. The Raman frequencies of PS and PSS are very similar, with the exception of the S-O stretching vibration present in PSS and not in PS around 1135 cm^{-1}. Table 3-1 summarizes our observed values of the vibrational frequencies of PS and PSS with the literature values. The strong PS peak at around 1000 cm^{-1} could potentially interfere with spectra of studied PEDOT, however, there are no strong PS or PSS peaks at the 1400-1580 cm^{-1} region which corresponds to PEDOT main ring stretch vibrations, discussed below.
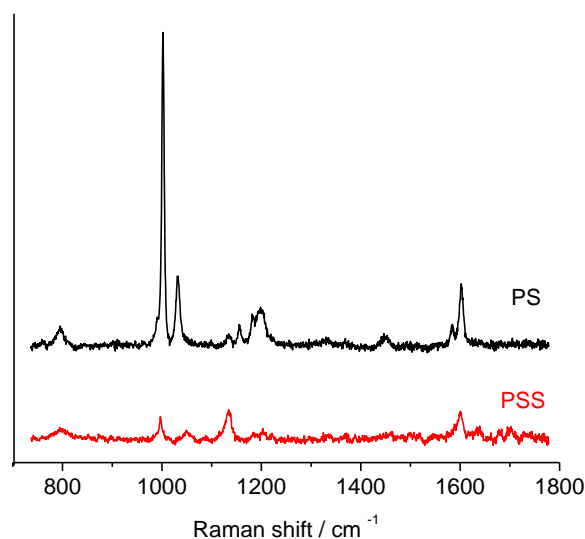
Figure 4-2. 632 nm excited Raman spectra of PS and PSS thick films.

PEDOT can exist in a neutral form or, through loss of electrons, it can become "singly oxidized" and "doubly oxidized" (Figure 4-3) . This oxidation readily happens in air, and thus as-received PEDOT is usually in the "doubly oxidized" form. The actual oxidation number for PEDOT polymer, the number of charges and unpaired spins on each monomeric unit of PEDOT, is continuously variable.[97]

Table 4-1 Raman frequencies of PS and PSS.

PSS gel[98]	PSS resin[99] (9% sulfonated)	PSS, this work	PS[100] (syndiotactic)	PS[101]	PS, this work
1627 (w)					
1600 (m)	1601 (m)	1600 (m)	1603 (m)	1603 (m)	1602 (m)
	1583 (m)		1583 (w)	1584 (w)	1583 (w)
	1449 (w)		1452 (w)	1449 (m)	1450 (w)
				1367 (w)	
	1326 (w)		1319 (w)	1306 (w)	
1197 (m)	1197 (w)		1204 (m)	1198 (m)	1196 (m)
	1182 (m)		1182 (m)	1182 (w)	1184 (w)
	1155 (w)		1156 (w)	1156 (w)	1154 (w)
1130 (s)	1126 (w)*	1135 (s)			
			1071 (w)		
1044 (m)	1031 (m)	1049 (w)	1028 (m)	1031 (m)	1030 (m)
	1001 (s)	998 (m)	1002 (s)	1002 (s)	999 (s)

*-SO_3 group vibration, weak in this spectrum because of low degree of sulfonation.

As-received oxidized PEDOT appears light blue in color and it has a broad absorption band at around 1200 nm. Neutral, reduced PEDOT has a strong absorption band in the visible around 580 nm. Spectra of spin-cast, as-received oxidized PEDOT

and of spin-cast PEDOT that has been chemically reduced with hydrazine are presented in Figure 4-4. Oxidized PEDOT absorbs mostly in the UV and near IR regions of the electromagnetic spectrum. PEDOT:PSS samples that are spin cast onto ITO and are protected from the air by the PS layer show different absorption spectra if they sit under the fluorescent room lights versus in the dark for 2 hours. This is not due to photodegradation, since the process is reversible and reproducible over and over with the same sample as evidenced by the absorption spectra. The observable spectral change of sample going from dark to light is very similar to what was observed by Garreau et al. during their spectroelectrochemical studies when they changed the potential from +600 mV to +1200 mV thereby oxidizing the sample.[102] The absorption spectrum of the PEDOT:PSS that was sitting in the dark for two hours has more absorbance in the UV region, and it has a well-pronounced peak at around 840 nm and apparently a second peak beyond 950 nm. PEDOT:PSS that is exposed to the room lights has a lesser absorption in the UV at about 390 nm and only one peak beyond 950 nm. The reduced form in Figure 4-4 on the right absorbs somewhat in the UV and mostly in the visible with the absorption maximum at around 580 nm.

The laser excitation wavelengths for Raman spectroscopy are superimposed with the absorption spectra of the as-received PEDOT:PSS and the reduced PEDOT:PSS films in Figure 4-4. Since the oxidized form of PEDOT does not absorb much at 400-600 nm, then for the 457.9 and 514.5 nm excitation wavelengths, there should be no resonance and the Raman signal from the samples should be weak. The 632.8 nm excitation wavelength should be weakly postresonant and the signal should be better but still weak. Since the reduced form does absorb in the visible region, then

the Raman signal at 632.8, 514.5 and 457.9 (at a lesser extent) nm should be stronger

and small accumulation times should be sufficient. Thus, we expect that the reduced

PEDOT will be preferentially enhanced over the as received oxidized PEDOT.
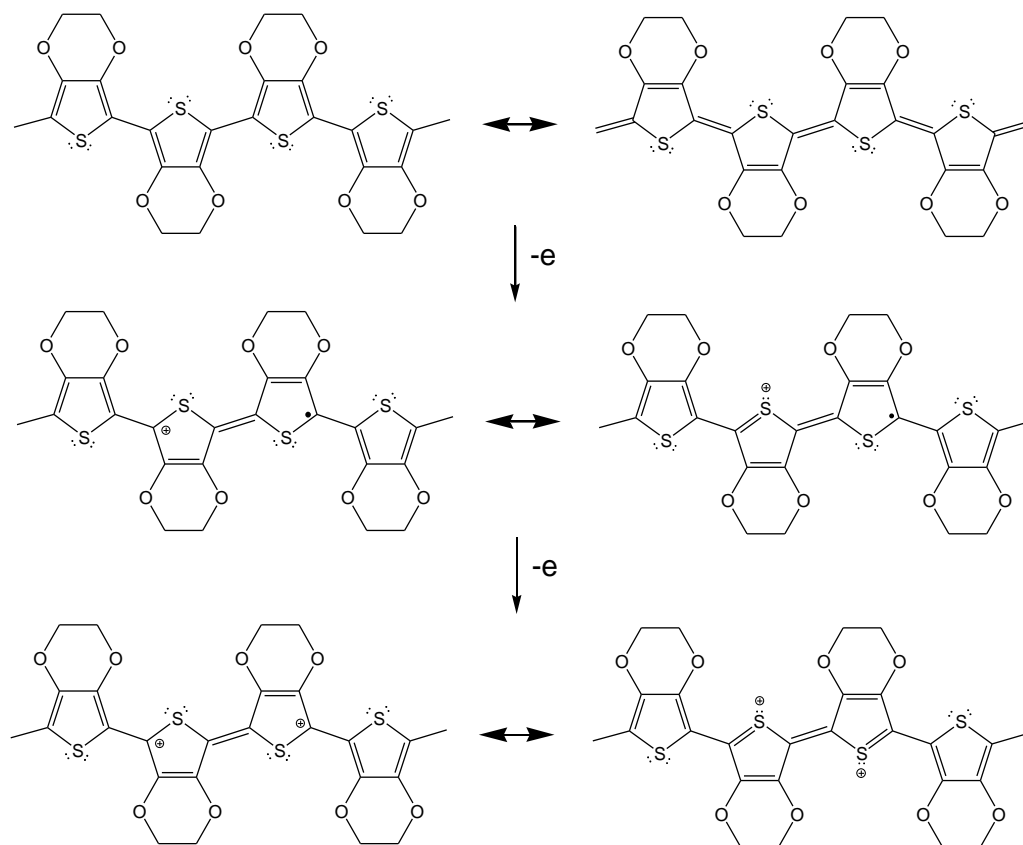
Figure 4-3. Representative resonance structures of PEDOT in its neutral and

successively oxidized forms.
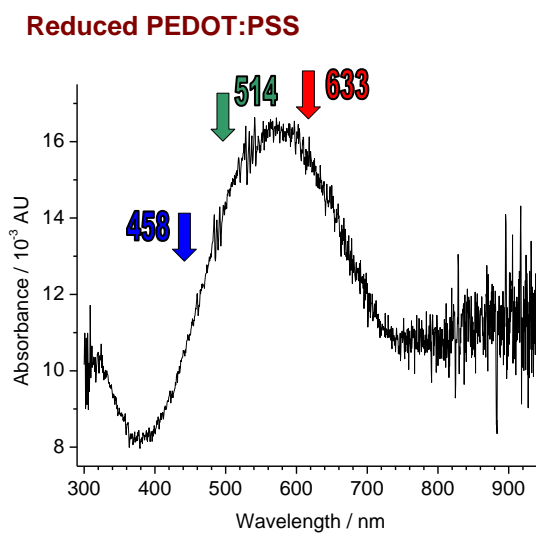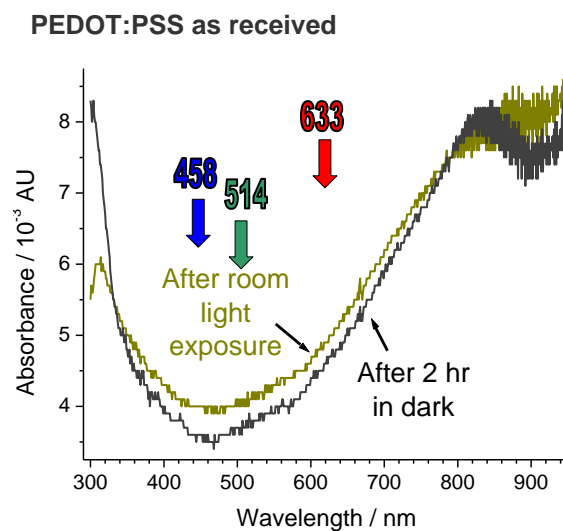
Figure 4-4. Above: Optical absorption spectra of a thin film of PEDOT:PSS on glass after preparation in ambient room light (black) and after sitting in the dark for 2 hours (grey). Below: Spectrum of PEDOT:PSS reduced with hydrazine prior to spin-coating on glass.

Vertically scaled and vertically shifted Raman spectra of oxidized and reduced PEDOT:PSS as a function of excitation wavelength are presented in Figure 4-5. Spectra of reduced PEDOT:PSS have their most prominent features in the 1400-1580 cm^{-1} region corresponding to the PEDOT main ring stretch vibrations as concluded from density functional theory calculations on dimers and trimers of EDOT and their sulfones. The most intense band in this region shifts and narrows with longer excitation wavelengths: it is at 1439 cm^{-1} with 457.9 nm excitation, at 1434 cm^{-1} with 514.5 nm excitation, and at 1427 cm^{-1} with 632.8 nm excitation. This makes sense in terms of resonance--progressively longer excitation wavelengths would resonate with molecules that have progressively longer effective conjugation lengths. The details of this principle for polymers are discussed elsewhere.[103] Bands in the 900-1400 cm^{-1} region are very similar at all three excitation wavelengths--peaks of moderate or low intensity around 993, 1269 and 1368 cm^{-1}.
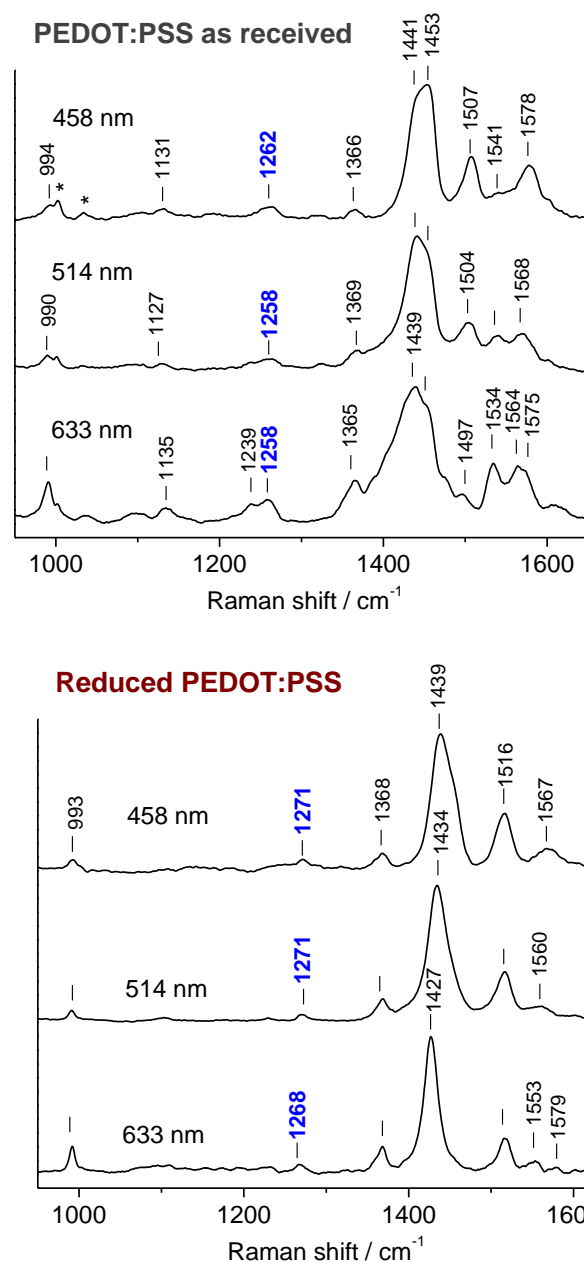
Figure 4-5. Above: Raman spectra of as-received PEDOT:PSS films, drop-coated onto glass and covered with a spin-coated layer of polystyrene, at three excitation wavelengths. Below: Corresponding spectra of PEDOT:PSS reduced with hydrazine. Asterisks mark peaks from the polystyrene overcoat. The spectra are scaled and vertically shifted. Peak positions labeled with a hash mark but no frequency are within ± 3 cm^{-1} of the spectrum immediately above.

Qualitatively, the less rich region of 950-1400 cm^{-1} is very similar between the oxidized and reduced PEDOT:PSS with peaks of moderate or low intensity around 991, 1262 and 1368 cm^{-1} with the exception of a new band at around 1131 cm^{-1} which is probably due to the S-O stretching vibration of PSS. Since the spectra in Figure 4-5 are vertically scaled for the ease of comparison, they do not show the relative intensities. Raman intensities from the reduced PEDOT:PSS are much larger than the Raman intensities from the oxidized PEDOT:PSS, therefore weak S-O stretching vibration of the non-resonant PSS are dwarfed by the reduced PEDOT:PSS Raman spectra but are visible in the oxidized PEDOT:PSS spectra at the 632.8, 514.5 and 457.9 nm excitation wavelengths. Also the 1258-1262 cm^{-1} peak present in the as received PEDOT:PSS spectra seems to consistently shift nine wavenumbers higher, and it exists at around 1268-1271 cm^{-1} in the spectra of the reduced PEDOT:PSS. This consistent shift by nine wavenumbers could be considered as a clear marker identifying whether a Raman spectrum corresponds to reduced or oxidized PEDOT:PSS. It could be not the 1258-1262 cm^{-1} mode shifting down, but some other mode that is shifting up.[102] Another suggestive marker for the oxidized form is the 1497-1507 cm^{-1} band versus a 1516 cm^{-1} band in the reduced form. In the literature, calculations on reduced PEDOT assign the 1270 cm^{-1} mode as the inter ring C-C stretch[102, 104] and the 1516 cm^{-1} mode as asymmetric C=C stretching of the sides of the thiophene ring.[102]

Table 4-2 Raman frequencies (cm^{-1}) of reduced PEDOT.

electrochemical reduction[102] (-1000 mV), 514 and 1064 nm	synthetic short oligomer,[103] 457-1064 nm	electrochemical reduction,[105] 785 and 1064 nm	chemical reduction,[106] 633 nm	chemical reduction, this work 458-633 nm
	1571 (w, 457) 1562 (w, 514)			1567 (w, 458) 1560 (w, 514) 1553 (w, 633)
1517 (m)	1514 (m, 457) 1508 (m, 514) 1506 (m, 676)	1516 (w, 785) 1520 (1064)	~1515 (m)	1516 (m)
	1458 (m, 457)			
1434 (s, 514) 1423 (s, 1064)	1440 (s, 457) 1434 (s, 514) 1423 (s, 676) 1427 (s, 1064)	1414 (s, 785) 1431 (1064)	~1422 (s)	1439 (s, 458) 1434 (s, 514) 1427 (s, 633)
1369 (m)	1369-1364 (m)	1370 (m)	~1370 (m)	1368 (m)
1270 (w)		1270 (1064)		1270 (w)
		1252 (m, 785)		
		1226 (1064)		
		1097 (w, 785) 1111 (1064)		
991 (w)		990 (m)		992 (w)

Table 4-3 Raman frequencies (cm^{-1}) of oxidized (doped) PEDOT.

PEDOT, +1000 mV[102] 1064 nm	PEDOT:PSS,[106] 633 nm	PEDOT:PSS, this work 458-633 nm	PEDOT:PSS,[107] on Si 633 nm
	~1570 (w)	1564-1578 (w)	1563 (w)
1546 (m)	~1530 (m)	1541 (w, 458) 1541 (w, 514) 1534 (m, 633)	1532 (w)
	~1490 (w)	1507 (w, 458) 1504 (w, 514) 1497 (w, 633)	1495 (m)
~1477 (s)			
~1454 (s)	~1450 (s)	1454 (m-s)	
~1430 (s)	~1438 (s)	1441 (sh, 458) 1442 (s, 514) 1439 (s, 633)	1421-1431 (s)
~1424 (m)	~1422 (s)		
~1369 (m)	~1365 (m)	1365-1369 (w-m)	1366 (m)
1295 (w)			
1268 (m)	~1260 (w)	1258-1262 (w)	1255 (m)
1239 (w)			
~1144 (m)		1127-1135 (w)	
			1093 (w)
~991 (m)		990-994 (w-m)	989 (m)

Table 4-2 and Table 4-3 summarize our observed values of the vibrational frequencies of reduced and oxidized PEDOT with the literature values. In general, our spectra are similar to those previously published in the literature[106, 102]; some of the differences in our spectra versus spectra in the literature could be due to different excitation wavelengths used;[105] our spectra on glass slides and on ITO covered glass slides are rather different from published spectra on Si wafers.[107]

Metal nanoparticles were deposited either on glass or ITO prior to spin-coating PEDOT:PSS or on top of the polymer as shown in Figure 3-1 and Raman spectra were collected as a function of excitation wavelength. The fluorescence backgrounds were subtracted and baselines were adjusted for ease of viewing, however the baseline-to-peak intensities are kept proportional to the measured signal strengths in counts per second. Figure 4-6 shows representative spectra at 632.8 nm excitation wavelength; however, the spectra from different parts of the sample were somewhat different in terms of overall intensity and variations of appearance due to non-uniform distribution of the drop-coated nanoparticles and therefore due to different environments around the polymers. The variation in nanoparticle density throughout the slide can be observed microscopically. This is why we did not attempt to quantitate the enhancements by silver or gold nanoparticles. The general trend was that the citrate reduced silver nanoparticles significantly enhanced the Raman signal from PEDOT, where gold nanoparticles enhanced the signal to a lesser degree.
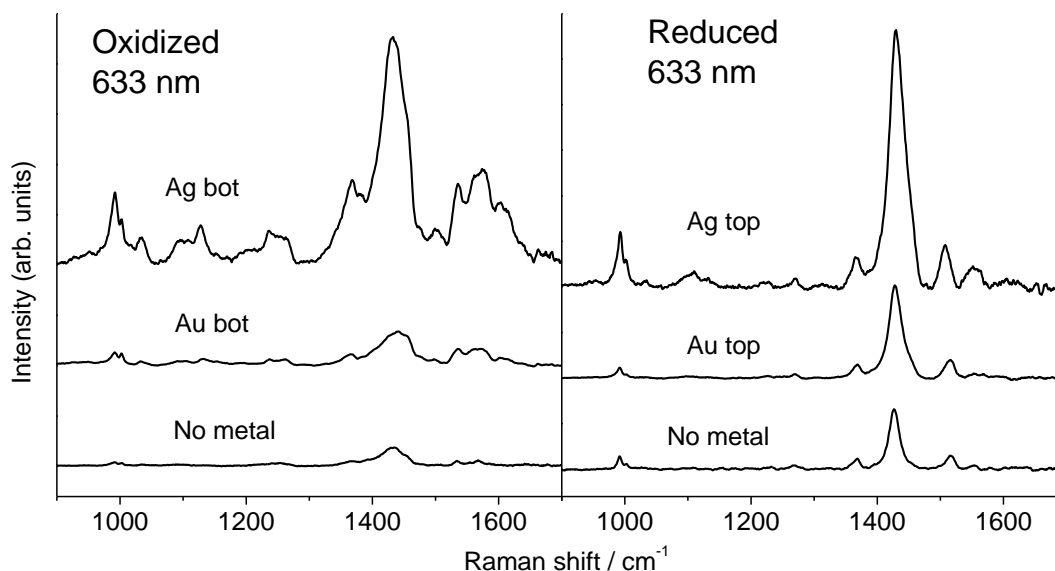
Figure 4-6. 632.8 nm excited Raman spectra of as-received ("oxidized") and chemically reduced ("reduced") PEDOT:PSS films in the absence of metal or with Au or Ag nanoparticles. All three spectra in each frame are plotted on the same scale in counts per second, and all samples consist of two spin-coated layers on glass.

Samples prepared with the incorporation of silver and gold nanoparticles exhibit not only the overall Raman intensity enhancements, but the relative intensities of some of the Raman lines exhibit changes. Interestingly, the changes depend on the location of nanoparticles--whether they are deposited under the PEDOT:PSS layer or on top of the polymer layer. See Figure 4-7 for vertically scaled spectra (for the ease of viewing and comparing) of as-received (top) and oxidized (bottom) PEDOT:PSS films on ITO-coated glass with or without Ag or Au nanoparticles, deposited either on the substrate prior to spin-coating the polymer ("bot") or on top of the PEDOT:PSS layer prior to overcoating with PS ("top"). Backgrounds have been

subtracted and spectra scaled and vertically shifted by arbitrary factors. Asterisks mark features from the PS overcoat. Peak positions labeled with a hash mark but no frequency are within $\pm$ 3 cm^{-1} of the spectrum immediately above. Figure 4-8 is the same kind of data but it is for the materials on the glass slides with no ITO coating. It seems that the presence or absence of ITO does not influence the spectra. From the spectra, it appears that when silver or gold nanoparticles are deposited on top, the lines in the 1530-1580 cm^{-1} region become deenhanced.

Using data in Figure 4-7 and Figure 4-8, we can talk about morphology of PEDOT and PSS components in the layer. It has been suggested that the aqueous emulsions of PEDOT:PSS are composed of PEDOT regions that are somewhat hydrophobic and PSS molecules surround the PEDOT grains, solubilizing them.[108] Many researchers propose that the same kind of morphology remains when the PEDOT:PSS is spin coated to form thin films.[16, 18, 108, 109] Since PEDOT grains are coated with PSS, then the PSS Raman signal should be enhanced to a greater degree by the proximity of metal nanoparticles than the PEDOT signal due to the plasmonic Raman enhancement falling rapidly with increasing distance. This is, in fact, what we see in both of the figures--the strongest Raman line of PSS, the SO$_3$ stretch at around 1133 cm^{-1}, is slightly stronger in reference to the PEDOT lines in the configurations where metal nanoparticles are deposited under the PEDOT:PSS layer. On the other hand, there is no such trend observed when the metal nanoparticles are deposited on top of the PEDOT:PSS layer. Another interesting observation into the morphology of the PEDOT:PSS layer is that when metal nanoparticles are deposited on the bottom, the thiophene ring stretching region at 1400-1600 cm^{-1} shifts to higher frequencies,

and, as discussed above, this can indicate shorter effective conjugation length and can imply less extended PEDOT chains. On the other hand, when metal nanoparticles are deposited on top of the PEDOT:PSS layer, the PEDOT chains seem to be more extended and seem to be closer to the metal nanoparticles.

Most apparent from Figure 4-7 and Figure 4-8 is that with incorporation of different metal nanoparticles either above or below the PEDOT:PSS layer, Raman spectra appears to be different. Samples prepared with as received oxidized PEDOT:PSS have different spectra when the nanoparticles are deposited and dried out on top of the spin-coated PEDOT:PSS ("top" in Figure 4-7 and Figure 4-8) versus the spectra of samples in which nanoparticles are deposited and dried out first and then the PEDOT:PSS layer is spin-cast ("bot" in Figure 4-7 and Figure 4-8). Spectra of PEDOT:PSS with no nanoparticles look very similar to spectra from samples in which silver or gold nanoparticles are deposited on the bottom. When the nanoparticles are deposited on top, the main thiophene stretching band shifts from about 1442 cm^{-1} down to about 1432 cm^{-1}, and the peak at about 1497 cm^{-1} shifts up to 1502-1506 cm^{-1}. Deposition of the two kinds of nanoparticles affects chemically reduced PEDOT:PSS differently. When gold nanoparticles are deposited either on the top or on the bottom, spectra of reduced PEDOT:PSS do not seem to change. However silver nanoparticles deposited on top of the polymer layer seem to produce a band at a higher wavenumber than the main thiophene stretching band. Silver nanoparticles deposited on the bottom under the reduced PEDOT:PSS layer produce spectra considerably different form the spectra of the polymer layer alone. In fact, the spectrum of reduced PEDOT:PSS with Ag on the bottom looks more like the

spectrum of oxidized PEDOT:PSS with silver on the bottom, suggesting that the chemically reduced PEDOT:PSS might have been reoxidized. Recalling identifying markers that have been noted from the examination of spectra presented in the Figure 4-5 (1258-1262 cm^{-1} peak of the as received oxidized PEDOT:PSS shifts to about 1268-1271 cm^{-1} in the spectra of the reduced PEDOT:PSS, and the 1497-1507 cm^{-1} band in the oxidized form versus a 1516 cm^{-1} band in the reduced form), these markers suggest that the chemically reduced PEDOT:PSS with Ag on the bottom gets reoxidized─ the 1268-1271 cm^{-1} band is shifted to about 1262 cm^{-1}, and the 1516 cm^{-1} band is replaced by the 1497-1507 cm^{-1} band. The oxidizing agent in this case is probably atmospheric oxygen: even though our samples are protected from the atmosphere by the PS layer, some of the oxygen might have been entrapped during the sample preparation in a regular lab atmosphere.

Light emitting diodes (LEDs) are basically photovoltaic devices working in reverse. Interestingly, organic polymer light emitting diodes based on polyfluorene with the incorporation of PEDOT layer exhibit nonemissive "black spots", and the formation of these nonemissive spots has been attributed to dedoping (reduction) of the PEDOT.[106, 110] Since from our data we see that citrate reduced silver nanoparticles deposited on the bottom reoxidize the PEDOT, then our results suggest that these silver nanoparticles in the bottom protect the PEDOT from the reduction type of damage thereby enhancing solar cell performance.
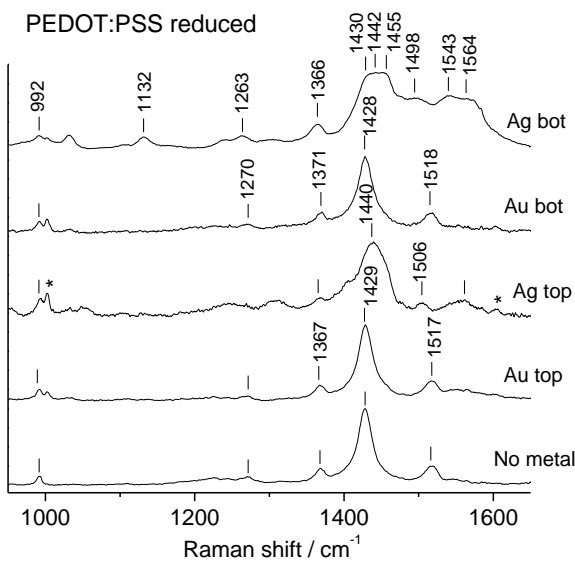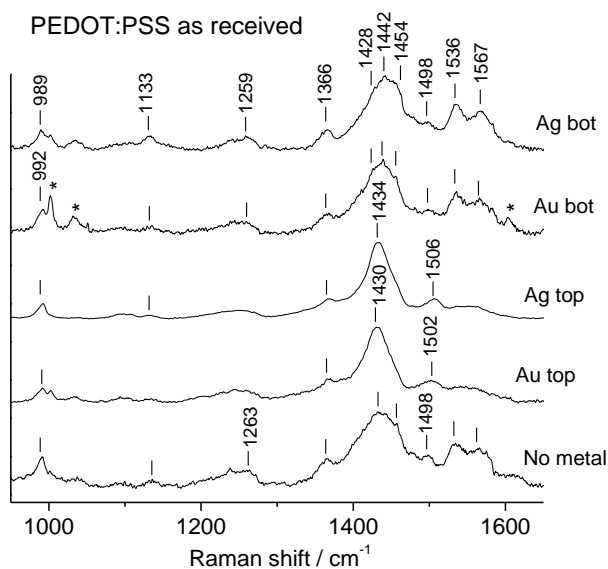
Figure 4-7. Above: 632.8 nm excited Raman spectra of as-received PEDOT:PSS films on ITO-coated glass with or without Ag or Au nanoparticles, deposited either on the substrate prior to spin-coating the polymer ("bot") or on top of the PEDOT:PSS layer prior to overcoating with PS ("top"). Backgrounds are subtracted, spectra is scaled and vertically shifted. Asterisks mark PS features. Peak positions labeled with a hash marks. Below: same for chemically reduced PEDOT:PSS.
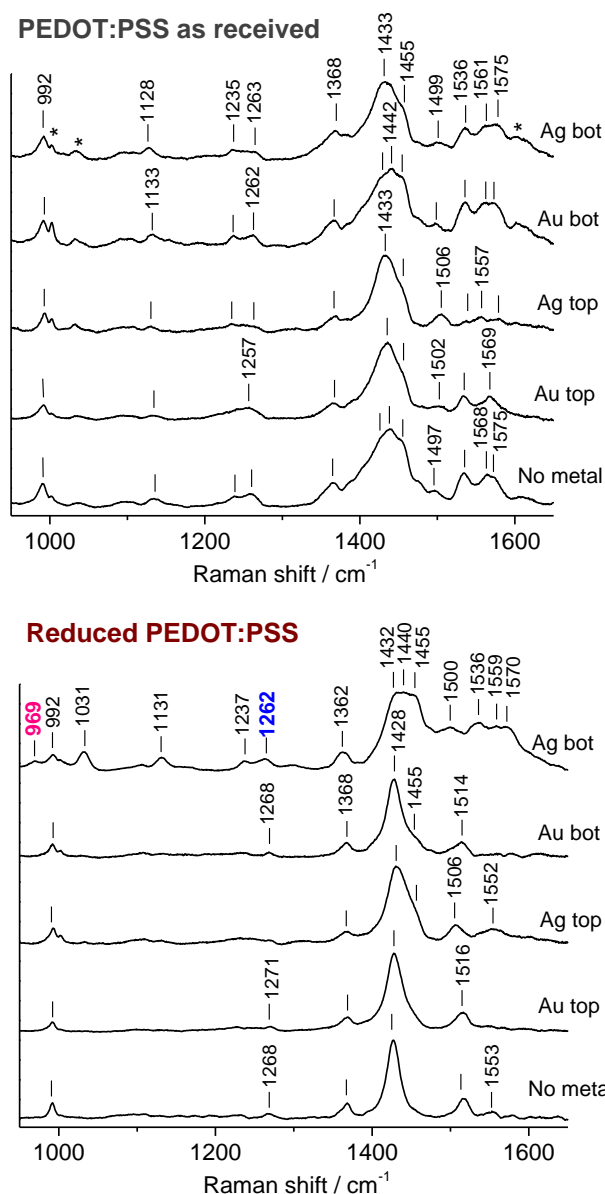
Figure 4-8. Above: 632.8 nm excited Raman spectra of as-received PEDOT:PSS films on glass with or without Ag or Au nanoparticles, deposited either on the glass prior to spin-coating the polymer ("bot") or on top of the PEDOT:PSS layer prior to overcoating with PS ("top"). Backgrounds are subtracted, spectra are scaled and vertically shifted. Asterisks mark PS features. Alike peak positions are labeled with hash marks. Below: same for chemically reduced PEDOT:PSS. Metal-free films were drop-coated, while metal-containing films were spin-coated.

Spectra of oxidized and reduced PEDOT:PSS are similar on glass slides and on ITO-coated glass slides. General trends of metal nanoparticle effects on the oxidized and reduced PEDOT:PSS that are observed with the use of 632.8 nm excitation are also present in the data obtained with 514.5 and 457.9 nm excitations; however, the effects of the metal nanoparticles are less pronounced. For example, reduced PEDOT:PSS with silver nanoparticles incorporated on the bottom seems to get reoxidized as judged by the 1268-1271 cm^{-1} band shifting to about 1262 cm^{-1}. At the shorter wavelengths, the fluorescence background is larger which reduces the signal-to-noise ratio. Also the SERS enhancement from gold nanoparticles is much weaker resulting in fewer counts per second.

When silver nanoparticles were incorporated on the bottom of the reduced PEDOT:PSS layer, other peaks appear: a weak one at around 969 cm^{-1} and stronger ones at 1031 cm^{-1} and 1131 cm^{-1} (Figure 4-8 for reduced PEDOT:PSS "Ag bot"). The 1131 cm^{-1} line could be, perhaps, attributed to PSS; however, reduced PEDOT is on resonance at 632.8 nm excitation wavelength and PSS is not, so PSS bands should not be as intense as PEDOT bands. PS does not have strong bands around 1131 cm^{-1} nor around 969 cm^{-1}. PS does have a line at 1030 cm^{-1}; however, the 999 cm^{-1} PS line is much stronger than the 1030 cm^{-1} line (Figure 4-2), and, therefore, it should be stronger than the observed 1031 cm^{-1} line in the "Ag bot" spectra of the reduced PEDOT:PSS. Since there is no 999 cm^{-1} line observed in the "Ag bot" spectra, then the 1031 cm^{-1} band is not due to PS. Spectra of the same samples taken with the Raman microscope system that focuses the excitation laser much tighter had the same lines plus many other new lines if the accumulation time was extended (Figure 4-9).

The new lines in the 950-110 cm^{-1} region were present in the spectra of the reduced PEDOT:PSS and to a lesser extent in the spectra of the oxidized PEDOT:PSS. These new lines at 960-980, 1052, and 1075 cm^{-1} sometimes appear in the presence of silver nanoparticles, and they do not appear in the presence of gold nanoparticles. The line in the 960-980 cm^{-1} region is not very sharp and can be found within a 20 cm^{-1} range, where the 1052 and 1075 cm^{-1} lines are sharper and their peak frequency does not vary much. Sometimes none of these lines are present at short accumulation times, and then the 960-980 cm^{-1} line grows in with time while the intensity of the thiophene ring stretching region decreases. In other cases the band at 960-980 cm^{-1} is present at very short accumulation times. Still other times the band at 960-980 cm^{-1} is not present, and it does not grow in with long accumulation times. 457.9 and 514.5 nm excitation spectra have similar features plus other new features like loss of intensity in the PEDOT ring stretch vibration region and increased intensity around 1585 cm^{-1}.

Since the new lines are more apparent when the Raman microscope is used to focus the excitation laser more tightly and since longer accumulation times can lead to greater spectral changes, we attribute these new lines to photodegradation. Photodegradation of PEDOT:PSS has been observed in previous studies and was attributed to different processes. As mentioned earlier, PEDOT dedoping (reduction) type of damage in polyfluorene/PEDOT:PSS during the LED operation was assumed based on Raman intensity changes;[110] however, the conclusion was not reinforced by Raman frequency changes. In another study, Raman spectral changes were observed indicative of PEDOT reduction in LEDs.[106] In other studies, X-ray photoelectron spectroscopy was used to characterize ultraviolet light-induced changes of doped

(oxidized) PEDOT and neutral and doped alkylated PEDOT;[108, 111] disruption of π-conjugation in the ring was observed either through chain scission that was accompanied by carbonyl/carboxyl groups addition or through addition of oxygen to the sulfur on the thiophene ring to produce sulfone groups R-SO$_2$-R. New features in the IR spectrum of poly(3-alkylthiophene) films upon visible or ultraviolet irradiation are assigned to ether, carbonyl, hydroxyl and to different sulfur-containing oxidative products.[112, 113]
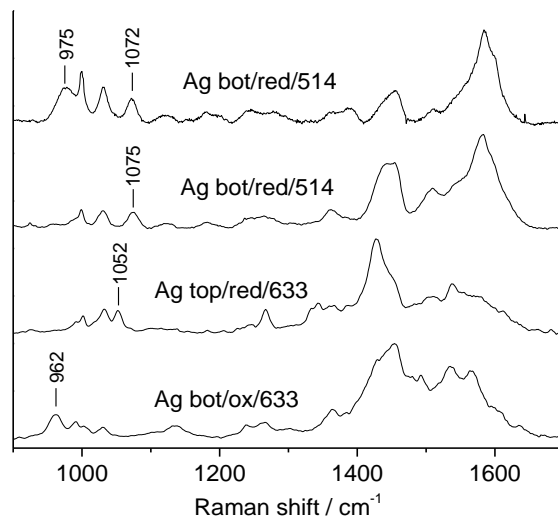
Figure 4-9. Raman spectra of as-received ("ox") and chemically reduced ("red") PEDOT:PSS films spin-coated on glass with Ag nanoparticles, obtained with the Raman microscope. New, presumably light-induced features are labeled.

It is common for organic molecules that are near SERS-active nanoparticles, in particular near silver nanoparticles, to exhibit rapid photochemical degradation.[70, 114-118] In numerous SERS experiments, broad bands at around 1590 cm^{-1} can be observed and are assigned to contaminants or photoproducts of amorphous

carbon,[70, 114-118] even though other molecules can also have Raman lines in this region. Thus the broad band at around 1590 cm^{-1} in Figure 4-9 could be assigned to photodegradation to amorphous carbon. However, the new lines in the 900-1100 cm^{-1} region of our PEDOT:PSS spectra seem to be more specific to PEDOT:PSS.

The new Raman lines appearing in presence of silver nanoparticles at 1075 cm^{-1}, 1052 cm^{-1} and in the 960-980 cm^{-1} region can be due to new oxygen containing structures that result from photodegradation and addition of oxygen to sulfur on the thiophene ring. However, reported Raman spectra of two different model compounds containing EDOT did not produce Raman peaks that can be clearly assigned to the SO_2 group.[119] On the other hand, IR spectra of photooxidized P3HT did show new lines at 1080 cm^{-1} and 1050 cm^{-1}; the second one was assigned to the S-O stretch of a sulfoxide group, R-SO-R.[112] Density functional theory calculations of PEDOT, performed by a former undergraduate student in our group, Brandon Hernandez, reveal the symmetric SO_2 stretch of EDOT sulfone at 1090 cm^{-1} and the S-O stretch of EDOT sulfoxide at 1031 cm^{-1}. On these bases we can tentatively assign the Raman line around 1075 cm^{-1} to sulfone stretching and the Raman line around 1052 cm^{-1} to sulfoxide stretching. Assigning of lines in the 960-980 cm^{-1} region is more vague; however, desulfonation damage to PSS promoted by light and heat have been observed;[108] additionally, the strongest Raman line of aqueous HSO_4^- is at 1040 cm^{-1} and the strongest Raman line of aqueous SO_4^{2-} is at 1040 cm^{-1}.[120]

As discussed above, silver nanoparticles can enhance solar cell performance by protecting PEDOT:PSS from the reduction type of the damage, however high light intensities or prolonged exposure to light can provoke photodegradation. Incoming

laser light hitting samples in our Raman microscope experiments were hundreds of MW/m^2, which is at least 5 orders of magnitude more than the solar flux. This means that the observed photodegradation that happens in our experiments and take seconds to minutes would take months to years during regular operation of the organic polymer solar cell, assuming that the process is linear in the photon flux.

4.2 P3HT/PCBM

4.2.1 P3HT/PCBM and nanospheres

Structures of P3HT and PCBM are presented in Figure 1-2. P3HT absorbs in the visible region of the electromagnetic spectrum at 400-650 nm (Figure 4-11); therefore, out of 7 excitation wavelengths used (363.8, 457.9, 488, 514.5, 543.5, 612 and 632.8 nm), 488, 514.5, 543.5 and 612 nm excitation wavelengths should be on resonance with P3HT resulting in a good Raman signal; 363.8 and 457.9 nm excitation wavelengths should be postresonant and the 632.8 nm excitation wavelength should be preresonant resulting in a weaker Raman signal. On the other hand, PCBM absorbs in the UV region; 363.8 nm excitation wavelength should be weakly preresonant resulting in a weak Raman signal and redder excitation wavelength should produce a very weak Raman signal. Based on the absorption spectrum of the P3HT/PCBM blend film, it seems that there might be some Raman signal due to PCBM at 363.8 nm excitation wavelength and not at other, redder wavelengths.
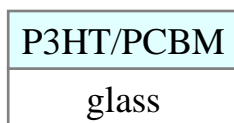
Figure 4-10. Schematic of a sample containing only a P3HT/PCBM film
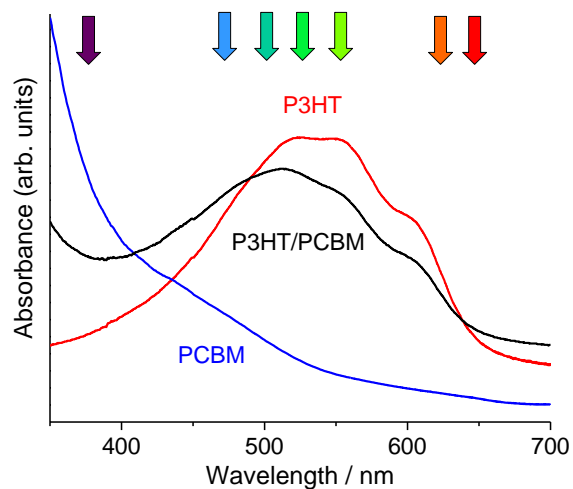
Figure 4-11. Absorption spectra of P3HT, of PCBM and of the P3HT/PCBM blend deposited as a thin film (Figure 4-10); arrows mark the excitation wavelengths used.

As expected, PCBM bands are observed in the Raman spectrum of the 1:1 blend of P3HT/PCBM film obtained with the 363.8 nm excitation wavelength (dashed lines in the Figure 4-12 A indicate positions of the PCBM bands). Sharp PCBM bands do not appear on spectra obtained with other excitation wavelengths that were used. For example, there are no observable PCBM lines in the spectrum of the 1:1 blend of P3HT/PCBM film obtained with the 514.5 nm excitation wavelength in Figure 4-12 B.
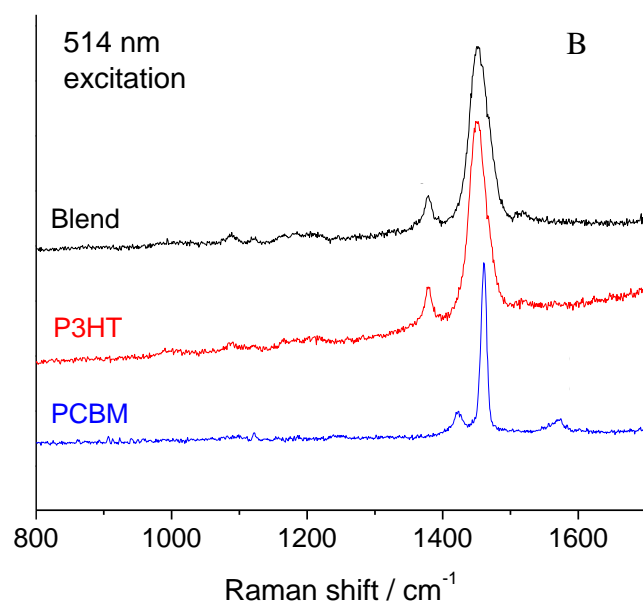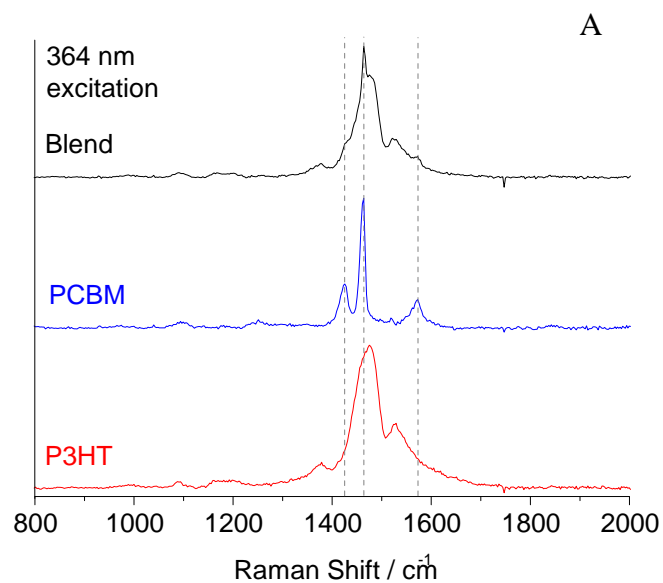
Figure 4-12. Raman spectra of P3HT, of PCBM and of the 1:1 blend of

P3HT/PCBM film obtained with the 363.8 nm (A) and 514.5 nm (B) excitation

wavelengths. Dashed lines in A indicate positions of three strongest lines of PCBM.

At first, incorporation of citrate-reduced silver and gold spherical nanoparticles was studied. Gold nanoparticles were prepared to be 15 nm in diameter as judged from TEM (Figure 3-3) and silver nanoparticles were less homogeneous with diameters ranging from 40 to 55 nm as judged by TEM. Drop-coating and drying these nanoparticles created microscopically inhomogeneous nanoparticle layers. While taking Raman spectra, samples containing the same nanoparticle densities were chosen as judged from nanoparticle layer extinctions in all three configurations: metal nanoparticles deposited on top of the P3HT/PCBM layer, in-between P3HT/PCBM and PEDOT:PSS layers, and on glass under the PEDOT:PSS layer. Spatially averaged nanoparticle film extinctions were above 1.0 absorbance units.

Representative Raman spectra at 514 nm excitation wavelength are given in Figure 4-13 for the three different geometries in which silver or gold nanoparticles were incorporated. Due to the high optical density of metal nanoparticles, when silver and gold were deposited on top of the active layer, Raman spectra were collected from the glass side (Figure 4-13 A). In this configuration of metal nanoparticles on top of the P3HT/PCBM, the P3HT Raman signal enhancements due to either silver or gold nanoparticle presence are about 3, which is very small by SERRS standards. This small enhancement could be due to polymers being further away from plasmon resonances on nanoparticles. As expected, when the active layer is separated from metal nanoparticles by a supportive PEDOT:PSS layer (in Figure 4-13 B), there is no P3HT Raman signal enhancement by the nanoparticles. This makes sense since plasmonic enhancement falls off very rapidly around the nanoparticles-- it falls off by

an order of magnitude within 2-3 nm of the nanoparticle surface.[58] In the configuration where the nanoparticles are deposited in-between PEDOT:PSS and P3HT/PCBM (Figure 4-13 C), Raman scattering is enhanced only in the presence of silver nanoparticles by a factor of two. In none of the three geometrical configurations used to incorporate metal nanoparticles were any bands that exhibited frequency shifts when metal nanoparticles were deposited nor were any of the band intensities surface enhanced more than others. This is very different than what has been observed for PEDOT:PSS with incorporation of nanoparticles-- Raman enhancement factors were much greater, bands were shifted in frequencies with nanoparticle incorporation, and intensities of some bands were enhanced more than others. In the case of P3HT/PCBM, this could mean that there are no significant changes in the ground-state structure of P3HT nor in the nature of the resonant excited state.

Small enhancements achieved with citrate reduced nanoparticles, difficulties with preparing samples with uniform films of metal nanoparticles by drop-coating and difficulties with reproducible metal optical densities makes citrate reduced nanoparticles not good candidates for quantitative studies of metal nanoparticle effects on P3HT/PCBM active layer. Better-fitted nanoparticles are nanoprisms since their plasmon resonance is much greater at the apexes, it's possible to have a better control of nanoprism sizes and, therefore, of associated plasmon resonance frequencies, and, finally, silver nanoprisms can be silanized on glass to better control nanoparticle density on a substrate.
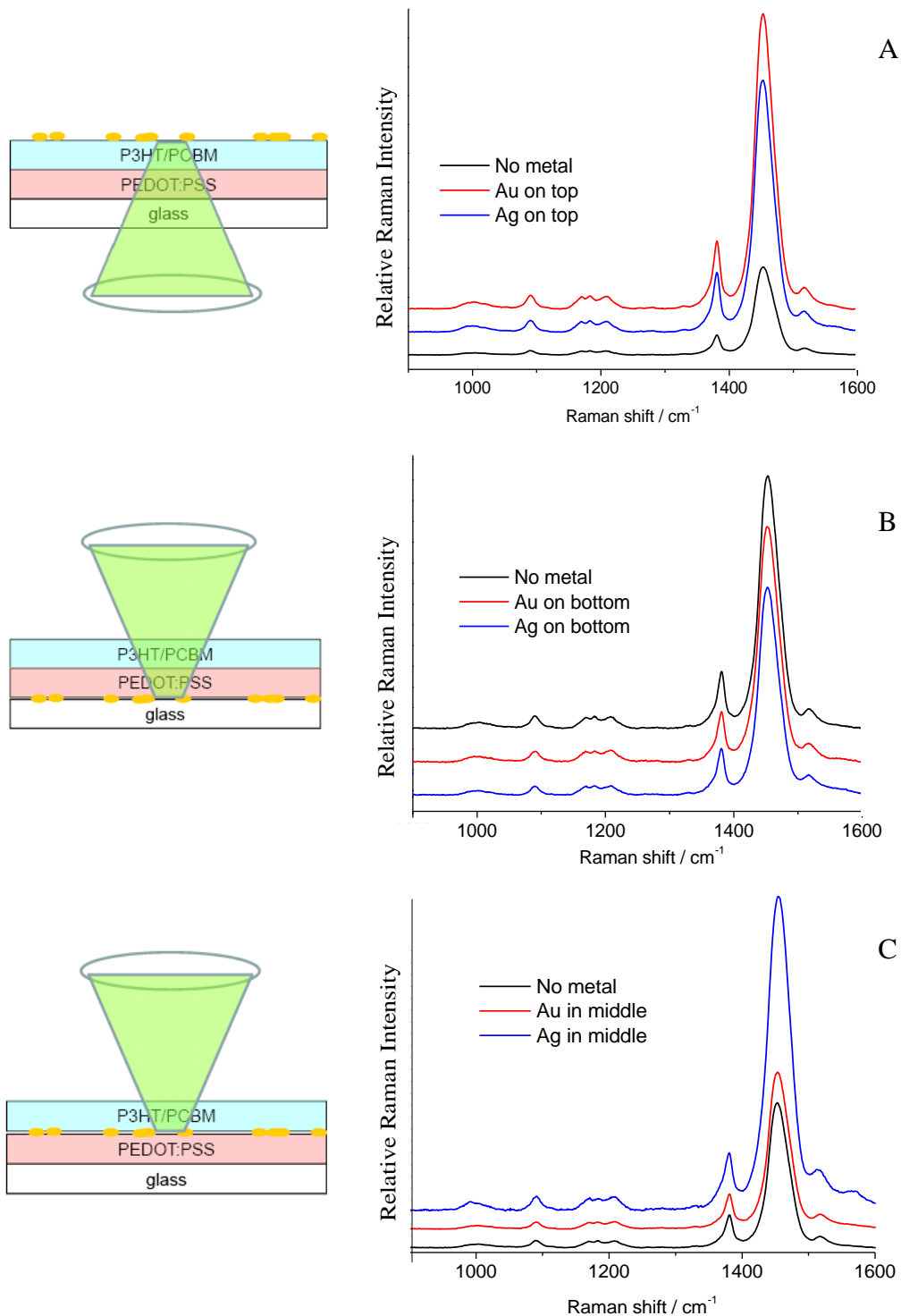
Figure 4-13. Raman spectra of P3HT:PCBM on Au and Ag citrate reduced NPs

in the indicated geometries with the 514.5 nm excitation wavelength.

4.2.2 P3HT/PCBM and nanoprisms
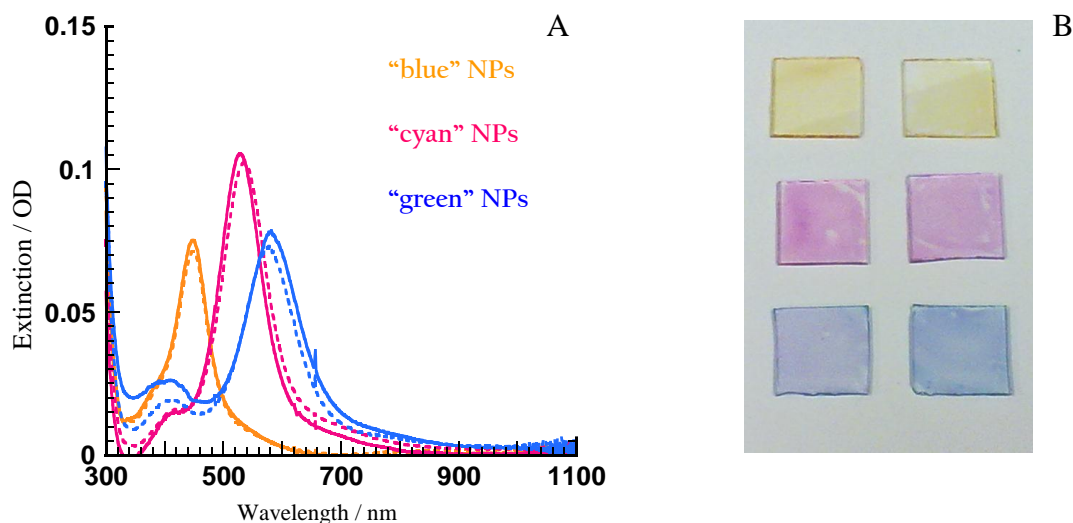
Figure 4-14. A: Raman spectra of P3HT:PCBM on Au and Ag citrate reduced NPs in the indicated geometries with the 514.5 nm excitation wavelength; B: Appearance of the 15 x 15 mm² slides covered by the NPs (Figures courtesy of A. Kulkarni).

Sizes of silver nanoprisms are better controlled than sizes of citrate reduced nanospheres and they can be silanized on a substrate with a greater control of the nanoparticle density. Nine nanoprisms with different average sizes corresponding to plasmon resonance maxima of 440-548 nm were prepared and later silanized by Abhishek Kulkarni and Michael Salvador, members of Professor David S. Ginger's group at the University of Washington. Representative spectra of three different sizes of nanoparticles in solution are given in Figure 4-14. The name of each nanoparticle type corresponds to the colors of the LED used to prepare it and roughly to the

plasmon resonance wavelength of the nanoparticles; for example, the plasmon resonance of "blue" NPs is in the blue region of the spectrum at around 450 nm. Shorter plasmon resonance wavelength indicates smaller nanoparticles, which is checked with TEM: "blue" nanoparticles are smaller than "cyan", and "cyan" nanoparticles are smaller than "green" ones.

When silanized nanoparticles were covered with P3HT/PCBM, the nanoparticle plasmon resonance was red-shifted. The modified extinction spectrum of the nanoparticles was found by subtracting the P3HT/PCBM alone spectrum from the spectrum of nanoparticles covered with P3HT/PCBM. Figure 4-15 A shows an extinction spectrum of one of the "green" nanoparticles alone with the plasmon resonance at 548 nm (blue curve) and an extinction spectrum of the same silanized nanoparticles modified by a spin-coated layer of P3HT/PCBM on top (red curve with plasmon resonance at 727 nm). The plasmon resonance of one of the "cyan" nanoprisms shown in Figure 3-3 shifts from 492 nm to 674 nm. The plasmon resonance of one of the "blue" nanoprisms exhibits a shift from 451 nm (blue curve in Figure 4-15 B) to 583 nm (red curve in Figure 4-15 B) upon incorporation of P3HT/PCBM. Samples with different plasmon resonances have different spectral overlap with P3HT/PCBM.
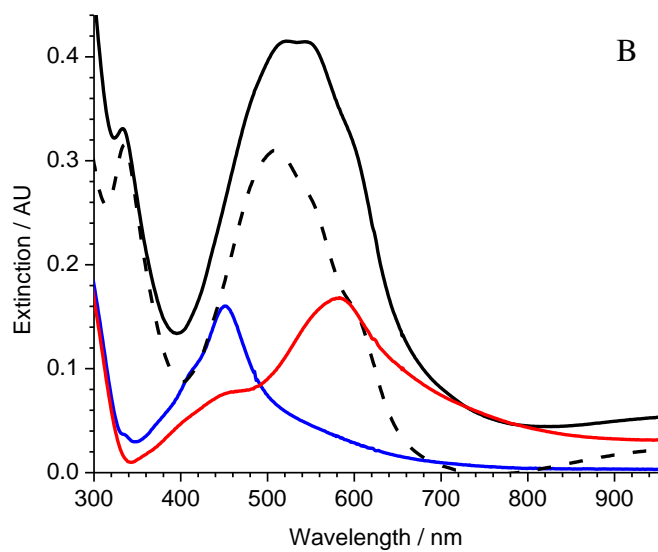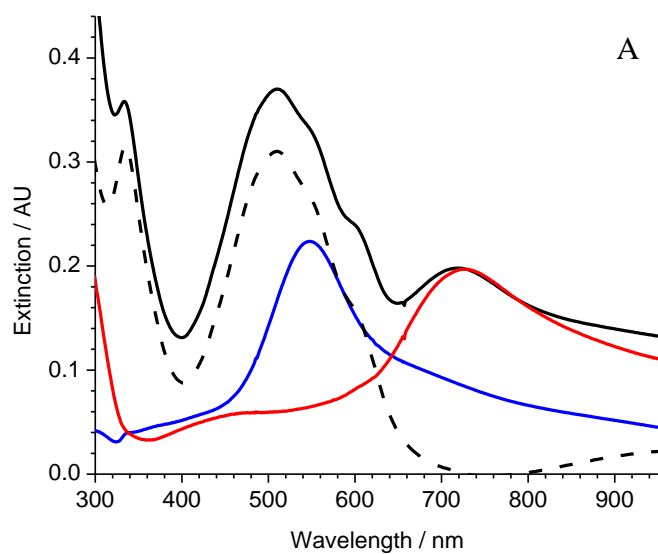
Figure 4-15. Measured extinction spectra for a "blue" type (A) and for a "green" type (B) of NPs silanized on a substrate is shown in blue color; red solid, the modified spectrum of the nanoparticles; black solid, nanoparticles with P3HT/PCBM; black dashed, P3HT/PCBM alone.

Raman spectra of P3HT/PCBM alone are presented in red in Figure 4-16 and spectra of P3HT/PCBM with "blue" nanoprisms from Figure 4-15A are presented in black for four out of seven excitation wavelengths. As mentioned in the discussion of Figure 4-12, only Raman spectra obtained with 363.8 nm show PCBM peaks at 1425, 1464, and 1573 cm^{-1}; these peaks are marked in Figure 4-16 with asterisks. P3HT peaks are present at all excitation wavelengths. The spectrum obtained with 363.8 nm is noisy at the P3HT/PCBM concentrations used and at thicknesses of the P3HT/PCBM layer that correspond to thickness used in operating organic polymer cells. Spectra obtained with 612 nm and with 632.8 nm (not shown in Figure 4-16) exhibit residual features that are due to very strong fluorescence background, pixel-to-pixel CCD sensitivity and etaloning of the back-illuminated CCD (unwanted features resulting from constructive and destructive interferences in a silicon optical cavity of the silicon chip) at red wavelengths. Features due to the wavelength dependent reflectivity of the spectrograph gratings and the wavelength dependent CCD throughput are usually corrected with the use of a broadband light source having a known, slowly varying, continuous spectrum. In our experiments, these features are not completely removed because the different spatial distributions of the broadband lamp source and the Raman scattering source illuminate the gratings and the detector somewhat differently.

Interestingly, fluorescence is enhanced by nearly the same amount due to presence of nanoprisms as the Raman scattering is increased (Figure 4-17); this was observed in different samples containing nanoparticles of different sizes and having different optical densities, and, therefore, having different enhancement factors. In the

first project of this dissertation, molecules were directly absorbed to nanoparticle surface resulting in surface enhanced Raman scattering and, if the molecule was fluorescent, in quenching of fluorescence by proximity of the nanoparticles. SERS enhancement decreases by an order of magnitude within a short distance of 2-3 nm from a nanoparticle surface,[1, 2] while fluorescence is quenched close to a nanoparticle but is enhanced at longer distances.[123-125] Fluorescence is quenched close to the metal because nonradiative decay rates are enhanced near metal nanoparticles.[126, 127] Modest SERS enhancements and fluorescence enhancement suggest that P3HT molecules are not on nanoparticle surfaces, but are rather separated from the nanoprisms perhaps due to ligands on nanoparticle surfaces. Excitation and radiative fluorescence rates might be sped up by metal nanoparticles, and faster radiative rates might decrease opportunities for the charge separation; however, the rate of charge transfer is much faster than the fluorescence.

Examining Figure 4-16, the greatest P3HT Raman signal enhancement achieved by incorporation of "green" metal nanoparticles happens at 612 nm excitation and the smallest enhancement is at 363.8 nm excitation. This makes sense since the greatest overlap of the modified nanoparticle extinction spectrum and spectrum of P3HT/PCBM happens at 612 nm (see the overlaps of the red curve and the dashed black curve on Figure 4-15A). At 364nm, PCBM and P3HT scattering is enhanced by the same amount.
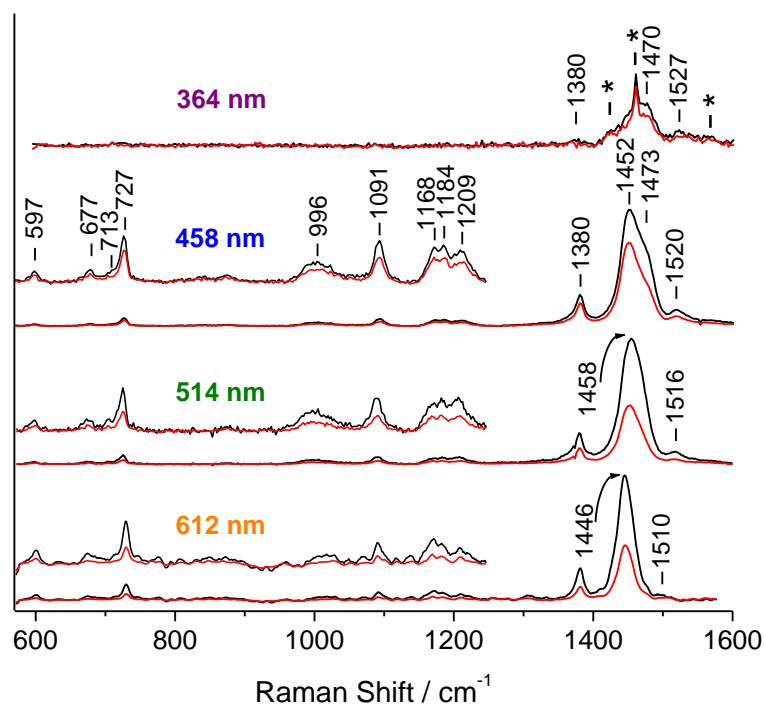
Figure 4-16. Raman spectra for the sample of Figure 4-15A at the indicated excitation wavelengths. Red, P3HT/PCBM alone; black, P3HT/PCBM with NP. Vertical scaling and offsets for the different excitation wavelengths are arbitrary. All labeled peaks belong to P3HT. The asterisks mark the PCBM peaks at 1425, 1464, and 1573 cm⁻¹.

Most of the P3HT bands appear at about the same frequencies at all seven excitation wavelengths, where, recalling effects of citrate reduced nanoparticles on PEDOT:PSS, there were a lot of bands in PEDOT Raman spectrum that were shifted in the presence of the metal. The only bands that change frequency with excitation wavelength are the bands that correspond to the thiophene ring in-phase stretching (see Supporting Information for the density functional theory calculations of the ground-state structure and vibrational frequencies of 3-ethylthiophene pentamer), and

the frequency changes are the same with and without silver nanoprisms. Figure 4-18 illustrates this shift for the most intense feature more clearly (intensities are scaled for ease of comparison): the band is at 1446 cm^{-1} with 612 nm excitation, it shifts to 1458 cm^{-1} with 514.5 nm excitation and to 1470 cm^{-1} with 457.9 and 363.8 nm excitations. The other shifting band is present at 1510 cm^{-1} with 612 nm excitation, at 1516 cm^{-1} with 514.5 nm excitation, at 1520 cm^{-1} with 457.9 nm excitation and at 1527 cm^{-1} with 363.8 nm excitation. The thiophene stretch band shift to higher frequency with lower excitation wavelength is the same phenomenon seen and discussed earlier for the PEDOT thiophene stretch band shift, and it is due to longer excitation wavelengths resonating with molecules that have progressively longer effective conjugation lengths. The aforementioned shift in a less intense thiophene ring stretch band is the most pronounced with 364 nm excitation wavelength; however, this could be due to excitation of shorter effective conjugation lengths as well as to change in resonance conditions-- the 364 nm excitation wavelength overlaps two strongly allowed electronic transitions. In contrast to PEDOT, though, the overall shift with the change of the excitation wavelength is exactly the same in the presence and in the absence of the nanoprisms, suggesting that presence of metal nanoparticles does not affect P3HT morphology.
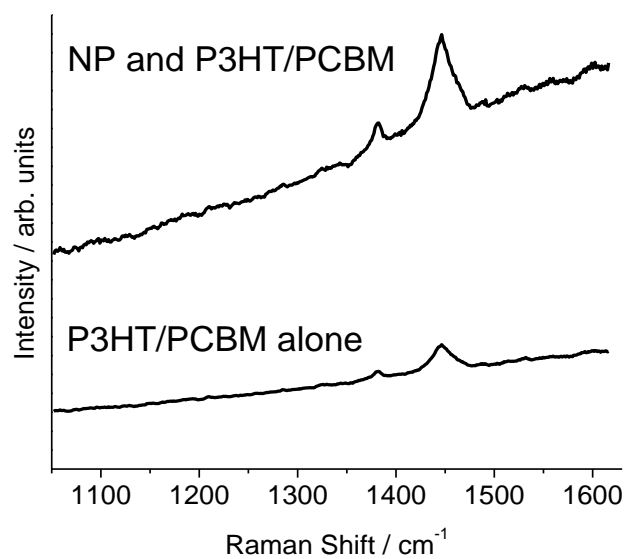
Figure 4-17. Total emission spectrum at 612 nm excitation for the sample

in Figure 4-15B.
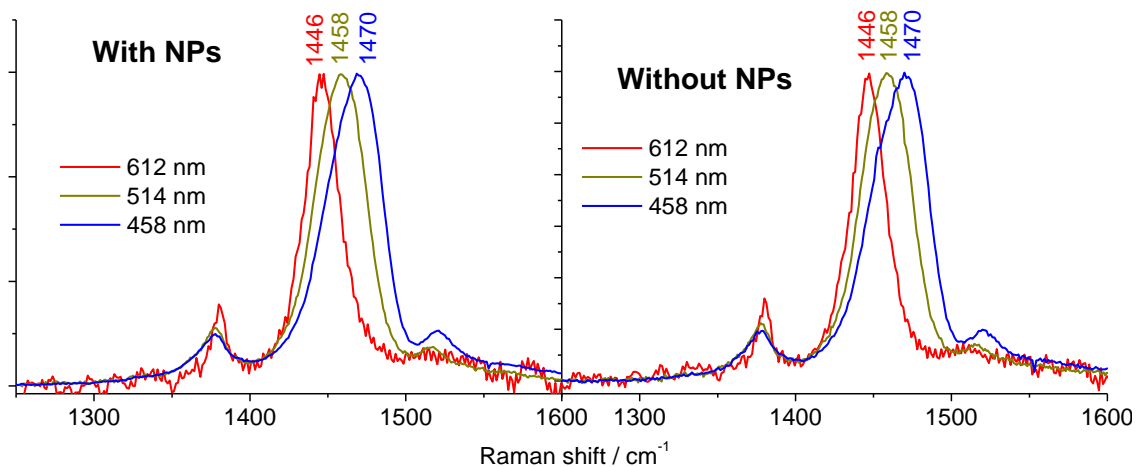
Figure 4-18. P3HT ring stretch shift in presence and in absence of nanoprisms.

Intensities are scaled for ease of comparison.

The long-lived charge carriers do not appear in our spectra since they absorb at longer wavelengths than the excitation wavelengths used for our steady-state experiments.[30, 128-129] Also, all bands seem to be enhanced to a similar degree with nanoprism presence at all excitation wavelengths, where in PEDOT:PSS metal nanospheres caused some bands to be enhanced more than others at certain wavelengths. No noticeable shift in band frequencies, as well as no bands being enhanced more than others with nanoparticle incorporation, means that there are no observable and significant changes in the ground-state structure nor in the nature of the resonant excited state of P3HT. Thus the SERS enhancement provided by the silver nanoprisms is electromagnetic in its nature, and chemical enhancement is either negligible or nonexistent.

SERS theoretical and experimental enhancement profiles as well as modified nanoparticle extinction spectra by P3HT/PCBM for five different kinds of nanoprisms are presented in Figures 4-19 A-D. Experimental enhancement profiles are constructed for the strongest P3HT line at ~ 1450 cm^{-1}; however, all P3HT Raman lines appear to be enhanced by the same factor at all wavelengths, and PCBM lines are also enhanced by the same degree at 363.8 nm excitation, within the measurement accuracy. Experimental enhancements are shown as points on the figures. Theoretical SERS enhancements are obtained using simple electromagnetic theory of SERS and equation 1-33 from project 1 in this dissertation using the modified (by P3HT/PCBM presence) nanoparticle extinction spectrum. Theoretical enhancements appear as dashed curves. "Modified" nanoparticle extinction spectra appear as solid curves. In Figure 4-19B, theoretical enhancements are also calculated using the extinction

spectrum of silanized nanoparticles before P3HT/PCBM is deposited on top; this is presented as a red short-dash curve. Experimental enhancements seem to be better portrayed by theoretical enhancements based on the modified nanoparticle extinction spectrum rather than on the extinction spectrum of nanoparticles alone. This makes sense, since it is known that when dielectric properties of the surrounding medium change, the plasmon resonance shifts.[122] Our assumption that the "modified" nanoparticle extinction spectrum can be estimated by the difference of nanoparticles with P3HT/PCBM and P3HT/PCBM is based on another assumption that the P3HT/PCBM spectrum is not changed by the presence of nanoparticles. In fact, we have seen how spectra of FITC change when FITC is adsorbed to gold nanoparticles (red dashed curve in Figure 4-17 in the first project of this dissertation). Similar to P3HT and silver nanoprisms, FITC and gold nanospheres had somewhat overlapping extinction spectra. However, FITC was adsorbed to the gold surface, where P3HT is not right next to the nanoparticle surface as judged by small SERS enhancement factors and not quenched fluorescence. P3HT not adsorbed directly to the silver surface should not undergo an extinction spectrum change that can be associated with chemical SERS enhancement mechanism. Furthermore, we have seen that the P3HT Raman bands did not undergo frequency changes in the presence of nanoprisms, indicating that the chemical SERS enhancement mechanism is negligible. Therefore, an assumption that we can use the "modified" nanoparticle extinction spectrum to model theoretical enhancements should be a justifiable one, and seems to be correct as the experimental enhancement points follow the theoretical enhancements rather nicely.
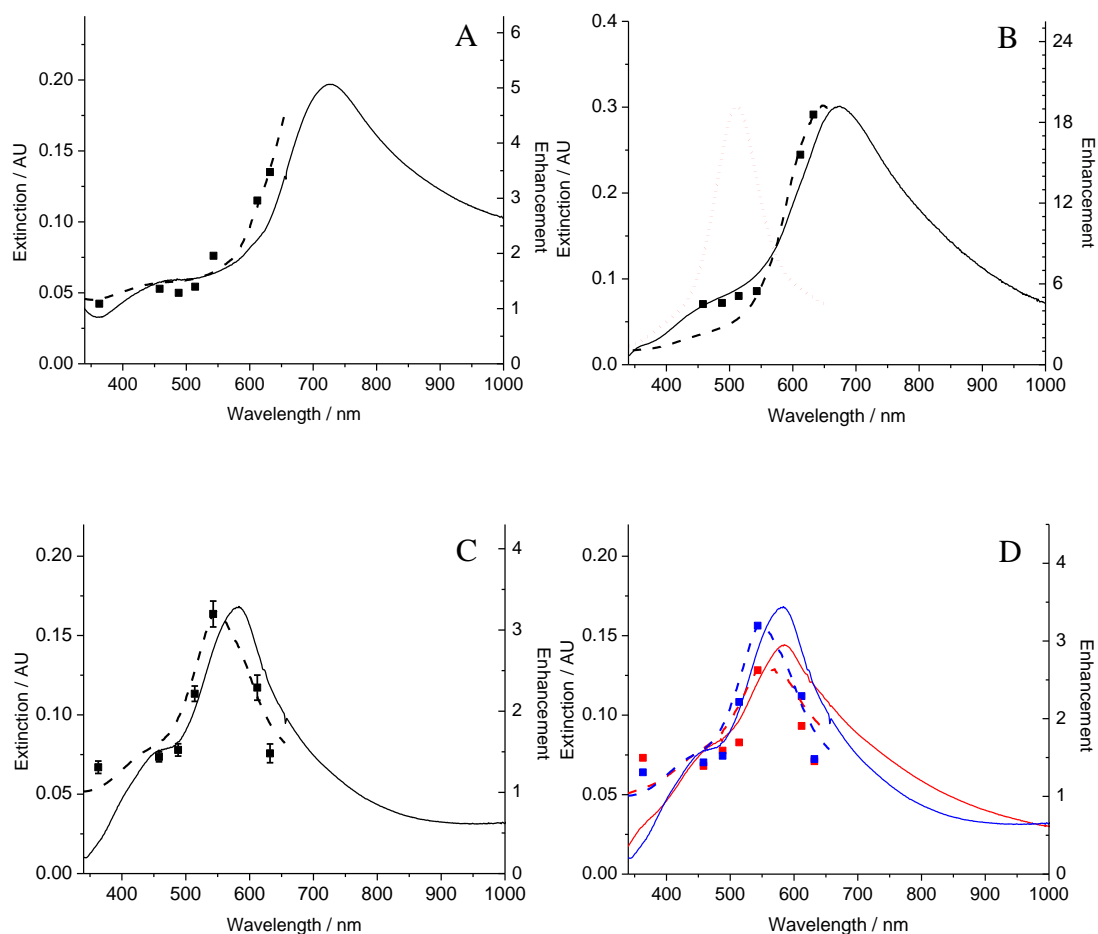
Figure 4-19. Experimental Raman enhancement factors for the ~1455 cm^{-1} P3HT band (points), modified NP extinction spectra (solid), and theoretical enhancements calculated from modified NP spectra using eq. (2) (dashed). Estimated uncertainties in the experimental enhancements are shown for one data set (C). The red dashed curve in (B) is the theoretical enhancement calculated from the unmodified NP extinction spectrum. The blue and red curves in (D) compare two samples with similar extinction spectra.

Estimated uncertainties in the experimental enhancements are shown in Figure 4-19C. Figure 4-19D compares experimental and theoretical SERS enhancements from two sets of nanoprisms with plasmon resonances at 583 nm, but with slightly different spectral band shapes. This slight difference in spectral band shapes impacts the theoretical and experimental SERS enhancements.

The maximum experimental Raman enhancements achieved by silver nanoprism incorporation are from about 2 to 20 depending on nanoparticle characteristics and nanoparticle density on the substrate. Typical SERS enhancements are in 10^4-10^6 orders of magnitude or higher, so our enhancements are very small in comparison to typical enhancements. If an experimental goal is to increase SERS enhancements, then it can be attempted by incorporation of greater number of nanoparticles and analytes, by increasing the path length of the excited light through the sample and collection of the signal, or by aggregating the nanoparticles, thereby creating "hot spots". In our experiments the nanoparticles are silanized on the surface; therefore, per about 35 nm thickness of the P3HT/PCBM layer, there is only one nanoprism available. In terms of the substrate plane, nanoprisms are distributed rather far from each other as seen on SEM images (Figure 3-3 Left). Therefore, most of P3HT and PCBM are not located near nanoprisms. Silanization provides random distribution of nanoprisms preventing aggregation caused by drop-coating method used earlier; therefore, with silanization nanoparticle distribution is not microscopically different from one region of the sample to another providing the same enhancement factors. (In the PEDOT:PSS study nanoparticles were drop coated providing non-uniform nanoparticle densities and therefore an attempt to quantitate

enhancement factors was not made.) The other factor that might have resulted in small enhancement factors is most of the P3HT and PCBM were a considerable distance away from the surface of nanoparticles, as was deduced from the fluorescence enhancement above (Figure 4-17 and accompanying discussion). P3HT and PCBM could also be separated from the nanoprism surface by organic ligands on the silver surface. From Michael Salvador's TEM images of silver nanoprism stacks and space between the nanoprisms (see supporting information for Ref. 121) the ligand shell is estimated to be ~0.41 nm. The ligands are believed to be citrate and/or bis(*p*-sulfonatophenyl)-phenylphosphine as both are used in nanoprism preparation. Bis(*p*-sulfonatophenyl)-phenylphosphine is a fairly large ligand and may not be readily displaced by P3HT or PCBM.

Electromagnetic enhancements approximated as $\left|E\right|^4$ at the nanoprism plasmon resonance wavelength were calculated by Michael Salvador with finite difference time domain simulations (see supporting information for Ref. 121) Briefly, a 22 nm side length and 13 nm thick nanoprism covered by a 1.9 nm thick ligand shell surrounded by 35 nm thick and 300 by 300 nm wide slab of P3HT/PCBM was calculated to give rise to electromagnetic enhancement of 60 averaged over the sample volume. The calculated plasmon resonance is much sharper and the electromagnetic enhancement larger than the experimental ones, which is probably due to the heterogeneity of actual silanized nanoprisms. Taking heterogeneity of nanoprisms, variations in actual spacing of the nanoparticles on the substrate and ambiguity of ligand shell thickness into consideration, our experimental enhancements are reasonable in comparison to theoretical magnitudes calculated by

Michael Salvador. Our SERS enhancements are consistent with silver nanoprisms under the P3HT/PCBM layer increasing polaron (a charge carrier) yield by as much as a factor of 3,[30] which was attributed to increased light absorption in the presence of silver nanoprisms.

5 Summary and Conclusion

5.1 PEDOT:PSS

Raman spectra of PEDOT:PSS are enhanced by presence of metal nanoparticles, intensities of some Raman bands are enhanced more than intensities of others and some bands are shifted in frequency while in proximity to metal nanoparticles, which suggests changes in PEDOT chain morphology. Our results suggest that silver nanoparticles can protect against reduction type of damage of PEDOT which can lead to enhancement of the organic solar cell efficiencies. On the other hand, at higher incident light intensities, silver nanoparticles promote photodegradation of PEDOT:PSS, which decreases the long-term stability of such solar cells.

5.2 P3HT/PCBM

Raman spectra of P3HT/PCBM are enhanced by presence of spherical silver and gold nanoparticles, and the signal is enhanced to a greater degree by incorporation of silver nanoprisms. In contrast with PEDOT:PSS studies, metal nanoparticles incorporated next to the P3HT/PCBM layer did not cause some Raman

bands to be enhanced more than others, nor did they cause shifts in band frequencies. The wavelength dependence of the experimental enhancements from silver nanoprisms agrees well with theoretical enhancements obtained using the electromagnetic theory of SERS and the extinction spectra of the silver nanoprisms as modified by the P3HT/PCBM layer. Therefore, metal nanoparticles seem to influence local electromagnetic fields and do not seem to change the morphology or chemical structure of P3HT and PCBM.

References

(1) Service R.F. Outlook Brightens for Plastic Solar Cells. *Science* **2011**, *332*, 293.

(2) Kromhout, W. W. UCLA Engineers Create Tandem Polymer Solar Cells that Set Record for Energy-Conversion. http://newsroom.ucla.edu/portal/ucla/ucla-engineers-create-tandem-polymer-228468.aspx (accessed 13 Feb., **2012**).

(3) Marks, R. N.; Halls, J. J. M.; Bradley, D. D. C.; Friend, R. H.; Holmes, A. B. The Photovoltaic Response in Poly(p-Phenylene Vinylene) Thin-Film Devices. *J. Phys.: Condens. Matter* **1994**, *6*, 1379.

(4) Markov, D. E.; Amsterdam, E.; Blom, P. W. M.; Sieval, A. B.; Hummelen, J. C. Accurate Measurement of the Exciton Diffusion Length in a Conjugated Polymer using a Heterostructure with a Side-Chain Cross-Linked Fullerene Layer. *J. Phys. Chem. A* **2005**, *109*, 5266-5274.

(5) Scully, S. R.; McGehee, M. D. Effects of Optical Interference and Energy Transfer on Exciton Diffusion Length Measurements in Organic Semiconductors. *J. Appl. Phys.* **2006**, *100*, 034907.

(6) Kim, Y.; Bradley, D. D. Bright Red Emission from Single Layer Polymer Light-Emitting Devices Based on Blends of Regioregular P3HT and F8BT. *Curr. Appl. Phys.* **2005**, *5*, 222-226.

(7) Brabec, C. J.; Sariciftci, N. S.; Hummelen, J. C. Plastic Solar Cells. *Adv. Funct. Mater.* **2001**, *11*, 15-26.

(8) Coakley, K. M.; McGehee, M. D. Conjugated Polymer Photovoltaic Cells. *Chem. Mater.* **2004**, *16*, 4533-4542.

(9) Yu, G.; Gao, J.; Hummelen, J. C.; Wudl, F.; Heeger, A. J. Polymer Photovoltaic Cells: Enhanced Efficiencies Via a Network of Internal Donor-Acceptor Heterojunctions. *Science* **1995**, *270*, 1789-1791.

(10) Shaheen, S. E.; Brabec, C. J.; Sariciftci, N. S.; Padinger, F.; Fromherz, T.; Hummelen, J. C. 2.5% Efficient Organic Plastic Solar Cells. *Appl. Phys. Lett.* **2001**, *78*, 841-843.

(11) Kim, J. Y.; Kim, S. H.; Lee, H.; Lee, K.; Ma, W.; Gong, X.; Heeger, A. J. New Architecture for High-Efficiency Polymer Photovoltaic Cells using Solution-Based Titanium Oxide as an Optical Spacer. *Adv. Mater.* **2006**, *18*, 572-576.

(12) Ma, W.; Yang, C.; Gong, X.; Lee, K.; Heeger, A. J. Thermally Stable, Efficient Polymer Solar Cells with Nanoscale Control of the Interpenetrating Network Morphology. *Adv. Funct. Mater.* **2005**, *15*, 1617-1622.

(13) Reyes-Reyes, M.; Kim, K.; Carroll, D. L. High-Efficiency Photovoltaic Devices Based on Annealed Poly(3-Hexylthiophene) and 1-(3-Methoxycarbonyl)-Propyl-1-Phenyl-(6,6)C_{61} Blends. *Appl. Phys. Lett.* **2005**, *87*, 083506.

(14) Lee, J. K.; Ma, W. L.; Brabec, C. J.; Yuen, J.; Moon, J. S.; Kim, J. Y.; Lee, K.; Bazan, G. C.; Heeger, A. J. Processing Additives for Improved Efficiency from Bulk Heterojunction Solar Cells. *J. Am. Chem. Soc.* **2008**, *130*, 3619-3623.

(15) Andersson, B. V.; Huang, D. M.; Moulé, A. J.; Inganäs, O. An Optical Spacer is no Panacea for Light Collection in Organic Solar Cells. *Appl. Phys. Lett.* **2009**, *94*, 043302.

(16) Nardes, A. M.; Janssen, R. A. J.; Kemerink, M. A Morphological Model for the Solvent-Enhanced Conductivity of PEDOT:PSS Thin Films. *Adv. Funct. Mater.* **2008**, *18*, 865-871.

(17) Dang, X.; Dante, M.; Nguyen, T. Morphology and Conductivity Modification of Poly(3,4-Ethylenedioxythiophene):Poly(Styrene Sulfonate) Films Induced by Conductive Atomic Force Microscopy Measurements. *Appl. Phys. Lett.* **2008**, *93*, 241911.

(18) Pingree, L. S. C.; MacLeod, B. A.; Ginger, D. S. The Changing Face of PEDOT : PSS Films: Substrate, Bias, and Processing Effects on Vertical Charge Transport. *J. Phys. Chem. C* **2008**, *112*, 7922-7927.

(19) Nah, Y.; Kim, S.; Park, J.; Park, H.; Jo, J.; Kim, D. Enhanced Electrochromic Absorption in Ag Nanoparticle Embedded Conjugated Polymer Composite Films. *Electrochem. Commun.* **2007**, *9*, 1542-1546.

(20) Tvingstedt, K.; Persson, N.; Inganas, O.; Rahachou, A.; Zozoulenko, I. V. Surface Plasmon Increase Absorption in Polymer Photovoltaic Cells. *Appl. Phys. Lett.* **2007**, *91*, 113514.

(21) Sue, C.; Hsieh, H.; Su, G. J. Enhanced Optical Absorption of Organic Materials Via Surface Plasmon Resonance in Gold Nanoparticles. *Proc. SPIE* **2007**, *6656*, 66561L.

(22) Chang, Y. C.; Chou, F. Y.; Yeh, P. H.; Chen, H. W.; Chang, S.; Lan, Y. C.; Guo, T. F.; Tsai, T. C.; Lee, C. T. Effects of Surface Plasmon Resonant Scattering on the Power Conversion Efficiency of Organic Thin-Film Solar Cells. *J. Vac. Sci. Technol. B* **2007**, *25*, 1899-1902.

(23) Kim, S.; Na, S.; Jo, J.; Kim, D.; Nah, Y. Plasmon Enhanced Performance of Organic Solar Cells using Electrodeposited Ag Nanoparticles. *Appl. Phys. Lett.* **2008**, *93*, 073307.

(24) Chen, X.; Zhao, C.; Rothberg, L.; Ng, M. Plasmon Enhancement of Bulk Heterojunction Organic Photovoltaic Devices by Electrode Modification. *Appl. Phys. Lett.* **2008**, *93*, 123302.

(25) Naidu, B. V. K.; Park, J. S.; Kim, S. C.; Park, S.; Lee, E.; Yoon, K.; Lee, S. J.; Lee, J. W.; Gal, Y.; Jin, S. Novel Hybrid Polymer Photovoltaics made by Generating Silver Nanoparticles in Polymer:Fullerene Bulk-Heterojunction Structures. *Solar Energy Materials & Solar Cells* **2008**, *92*, 397-401.

(26) Tong, S. W.; Zhang, C. F.; Jiang, C. Y.; Liu, G.; Ling, Q. D.; Kang, E. T.; Chan, D. S. H.; Zhu, C. Improvement in the Hole Collection of Polymer Solar Cells by Utilizing Gold Nanoparticle Buffer Layer. *Chem. Phys. Lett.* **2008**, *453*, 73-76.

(27) Morfa, A. J.; Rowlen, K. L.; III, R. T. H.; Romero, M. J.; van de Lagemaat, J. Plasmon-Enhanced Solar Energy Conversion in Organic Bulk Heterojunction Photovoltaics. *Appl. Phys. Lett.* **2008**, *92*, 013504.

(28) Chen, F.; Wu, J.; Lee, C.; Hong, Y.; Kuo, C.; Huang, M. H. Plasmonic-Enhanced Polymer Photovoltaic Devices Incorporating Solution-Processable Metal Nanoparticles. *Appl. Phys Lett.* **2009**, *95*, 013305.

(29) Yoon, W.; Jung, K.; Liu, J.; Duraisamy, T.; Revur, R.; Teixeira, F. L.; Sengupta, S.; Berger, P. R. Plasmon-Enhanced Optical Absorption and Photocurrent in Organic Bulk Heterojunction Photovoltaic Devices using Self-Assembled Layer

of Silver Nanoparticles. *Solar Energy Materials & Solar Cells* **2010**, *94*, 128-132.

(30) Kulkarni, A. P.; Noone, K. M.; Munechika, K.; Guyer, S. R.; Ginger, D. S. Plasmon-Enhanced Charge Carrier Generation in Organic Photovoltaic Films using Silver Nanoprisms. *Nano Lett.* **2010**, *10*, 1501-1505.

(31) Rand, B. P.; Peumans, P.; Forrest, S. R. Long-Range Absorption Enhancement in Organic Tandem Thin-Film Solar Cells Containing Silver Nanoclusters. *J. Appl. Phys.* **2004**, *96*, 7519-7526.

(32) Barazzouk, S.; Hotchandani, S. Enhanced Charge Separation in Chlorophyll a Solar Cell by Gold Nanoparticles. *J. Appl. Phys.* **2004**, *96*, 7744-7746.

(33) Heidel, T. D.; Mapel, J. K.; Singh, M.; Celebi, K.; Baldo, M. A. Surface Plasmon Polariton Mediated Energy Transfer in Organic Photovoltaic Devices. *Appl. Phys. Lett.* **2007**, *91*, 093506.

(34) Pan, S.; Rothberg, L. J. Plasmon Enhancement of Organic Photovoltaic Efficiency in Tandem Cells of pentacene/C$_{60}$. *Proc. SPIE* **2007**, *6641*, 664109.

(35) Park, J.; Ullah, M. H.; Park, S. S.; Ha, C. Organic Electroluminescent Devices using Quantum-Size Silver Nanoparticles. *J. Mater. Sci: Mater. Electron.* **2007**, *18*, S393-S397.

(36) Hägglund, C.; Zach, M.; Kasemo, B. Enhanced Charge Carrier Generation in Dye Sensitized Solar Cells by Nanoparticle Plasmons. *Appl. Phys. Lett.* **2008**, *92*, 013113.

(37) Yang, M. D.; Liu, Y. K.; Shen, J. L.; Wu, C. H.; Lin, C. A.; Chang, W. H.; Wang, H. H.; Yeh, H. I.; Chan, W. H.; Parak, W. J. Improvement of Conversion

Efficiency for Multi-Junction Solar Cells by Incorporation of Au Nanoclusters. *Opt. Express* **2008**, *16*, 15754-15758.

(38) Standridge, S. D.; Schatz, G. C.; Hupp, J. T. Distance Dependence of Plasmon-Enhanced Photocurrent in Dye-Sensitized Solar Cells. *J. Am. Chem. Soc.* **2009**, *131*, 8407–8409.

(39) Topp, K.; Borchert, H.; Johnen, F.; Tunc, A. V.; Knipper, M.; von Hauff, E.; Parisi, J.; Al-Shamery, K. Impact of the Incorporation of Au Nanoparticles into polymer/fullerene Solar Cells. *J. Phys. Chem. A* **2010**, *114*, 3981-3989.

(40) Xue, M.; Li, L.; Tremolet de Villers, B. J.; Shen, H.; Zhu, J.; Yu, Z.; Stieg, A. Z.; Pei, Q.; Schwartz, B. J.; Wang, K. L. Charge-Carrier Dynamics in Hybrid Plasmonic Organic Solar Cells with Ag Nanoparticles. *Appl. Phys. Lett.* **2011**, *98*, 253302.

(41) Cole, J. R.; Halas, N. J. Optimized Plasmonic Nanoparticle Distributions for Solar Spectrum Harvesting. *Appl. Phys. Lett.* **2006**, *89*, 153120.

(42) Catchpole, K. R.; Polman, A. Plasmonic Solar Cells. *Opt. Express* **2008**, *16*, 21793-21800.

(43) Pillai, S.; Catchpole, K. R.; Trupke, T.; Green, M. A. Surface Plasmon Enhanced Silicon Solar Cells. *J. Appl. Phys.* **2007**, *101*, 093105.

(44) Derkacs, D.; Lim, S. H.; Matheu, P.; Mar, W.; Yu, E. T. Improved Performance of Amorphous Silicon Solar Cells Via Scattering from Surface Plasmon Polaritons in Nearby Metallic Nanoparticles. *Appl. Phys. Lett.* **2006**, *89*, 093103.

(45) Tsai, S.; Ballarotto, M.; Romero, D. B.; Herman, W. N.; Kan, H.; Phaneuf, R. J. Effect of Gold Nanopillar Arrays on the Absorption Spectrum of a Bulk Heterojunction Organic Solar Cell. *Opt. Express* **2010**, *18*, A528-A535.

(46) Atwater, H. A.; Polman, A. Plasmonics for Improved Photovoltaic Devices. *Nat. Mater.* **2010**, *9*, 205-213.

(47) Wu, J.; Chen, F.; Hsiao, Y.; Chien, F.; Chen, P.; Kuo, C.; Huang, M. H.; Hsu, C. Surface Plasmonic Effects of Metallic Nanoparticles on the Performance of Polymer Bulk Heterojunction Solar Cells. *ACS Nano* **2011**, *5*, 959-967.

(48) Chang, M.; Chen, Y.; Tsai, Y.; Chi, K. Blending Platinum Nanoparticles into Poly(3-Hexylthiophene):[6,6]-Phenyl-C_{61}-Butyric Acid Methyl Ester Enhances the Efficiency of Polymer Solar Cells. *J. Electrochem. Soc.* **2009**, *156*, B234-B237.

(49) Kelley, A. M. A Molecular Spectroscopic Description of Optical Spectra of J-Aggregated Dyes on Gold Nanoparticles. *Nano Lett.* **200**7, *7*, 3235-3240.

(50) Otto, A. The "Chemical" (Electronic) Contribution to Surface-Enhanced Raman Scattering. *J. Raman Spectrosc.* **2005**, *36*, 497-509.

(51) Lombardi, J. R.; Birke, R. L. Time-Dependent Picture of the Charge-Transfer Contributions to Surface Enhanced Raman Spectroscopy. *J. Chem. Phys.* **2007**, *126*, 244709.

(52) Kambhampati, P.; Child, C. M.; Foster, M. C.; Campion, A. On the Chemical Mechanism of Surface Enhanced Raman Scattering: Experiment and Theory. *J. Chem. Phys.* **1998**, *108*, 5013-5026.

(53) Hawkridge, A. M.; Pemberton, J. E. Model Aluminum-Poly(p-Phenylenevinylene) Interfaces Studied by Surface Raman Spectroscopy. *J. Am. Chem. Soc.* **2003**, *125*, 624-625.

(54) Zhang, W.; Xu, Y.; Wang, H.; Xu, C.; Yang, S. Fe_3O_4 Nanoparticles Induced Magnetic Field Effect on Efficiency Enhancement of P3HT:PCBM Bulk Heterojunction Polymer Solar Cells. *Solar Energy Mater. Solar Cells* **2011**, *95*, 2880-2885.

(55) Shakya, P.; Desai, P.; Kreouzis, T.; Gillin, W. P.; Tuladhar, S. M.; Ballantyne, A. M.; Nelson, J. The Effect of Applied Magnetic Field on Photocurrent Generation in Poly-3-Hexylthiophene:[6,6]-Phenyl C61-Butyric Acid Methyl Ester Photovoltaic Devices. *Journal of Physics: Condensed* **2008**, *20*, 452203.

(56) Kelly, K. L.; Coronado, E.; Zhao, L. L.; Schatz, G. C. The Optical Properties of Metal Nanoparticles: The Influence of Size, Shape, and Dielectric Environment. *J. Phys. Chem. B* **2003**, *107*, 668-677.

(57) Hao E.; Schatz G. C. Electromagnetic Fields Around Silver Nanoparticles and Dimers. *J. Chem. Phys.* **2004**, *120*, 357-66.

(58) Stiles, P. L.; Dieringer, J. A.; Shah, N. C.; Van Duyne, R. P. Surface-Enhanced Raman Spectroscopy. *Ann. Rev. Anal. Chem.* **2008**, *1*, 601-626.

(59) Li, G.; Shrotriya, V.; Huang, J.; Yao, Y.; Moriarty, T.; Emery, K.; Yang, Y. High-Efficiency Solution Processable Polymer Photovoltaic Cells by Self-Organization of Polymer Blends. *Nat. Mater.* **2005**, *4*, 864-868.

(60) Nicholson, P. G.; Ruiz, V.; Macpherson, J. V.; Unwin, P. R. Enhanced Visible Photoluminescence in Ultrathin Poly(3-Hexylthiophene) Films by Incorporation of Au Nanoparticles. *Chem. Commun.* **2005**, , 1052-1054.

(61) Wiederrecht, G. P.; Wurtz, G. A.; Hranisavljevic, J. Coherent Coupling of Molecular Excitons to Electronic Polarizations of Noble Metal Nanoparticles. *Nano Lett.* **2004**, *4*, 2121-2125.

(62) Franzen, S.; Folmer, J. C. W.; Glomm, W. R.; O'Neal, R. Optical Properties of Dye Molecules Adsorbed on Single Gold and Silver Nanoparticles. *J. Phys. Chem. A* **2002**, *106*, 6533-6540.

(63) Nerambourg, N.; Werts, M. H. V.; Charlot, M.; Blanchard-Desce, M. Quenching of Molecular Fluorescence on the Surface of Monolayer-Protected Gold Nanoparticles Investigated using Place Exchange Equilibria. *Langmuir* **2007**, *23*, 5563-5570.

(64) Marchi, M. C.; Bilmes, S. A.; Bilmes, G. M. Photophysics of Rhodamine B Interacting with Silver Spheroids. *J. Colloid Interface Sci.* **1999**, *218*, 112-117.

(65) Ipe, B. I.; Thomas, K. G. Investigations on Nanoparticle-Chromophore and Interchromophore Interactions in Pyrene-Capped Gold Nanoparticles. *J. Phys. Chem. B* **2004**, *108*, 13265-13272.

(66) Zhao, J.; Jensen, L.; Sung, J.; Zou, S.; Schatz, G. C.; Van Duyne, R. P. Interaction of Plasmon and Molecular Resonances for Rhodamine 6G Adsorbed on Silver Nanoparticles. *J. Am. Chem. Soc.* **2007**, *129*, 7647-7656.

(67) Wurtz, G. A.; Evans, P. R.; Hendren, W.; Atkinson, R.; Dickson, W.; Pollard, R. J.; Zayats, A. V.; Harrison, W.; Bower, C. Molecular Plasmonics with Tunable

Exciton-Plasmon Coupling Strength in J-Aggregate Hybridized Au Nanorod Assemblies. *Nano Lett.* **2007**, *7*, 1297-1303.

(68) Niu, Z.; Fang, Y. A New Surface-Enhanced Raman Scattering System for C_{60} Fullerene: Silver Nano-particles/C_{60}/silver Film. *Vib. Spectrosc.* **2007**, *43*, 415-419.

(69) Lefrant, S.; Baltog, I.; de la Chappelle, M. L.; Baibarac, M.; Louarn, G.; Journet, C.; Bernier, P. Structural Properties of some Conducting Polymers and Carbon Nanotubes Investigated by SERS Spectroscopy. *Synth. Met.* **1999**, *100*, 13-27.

(70) Wang, Z.; Rothberg, L. J. Structure and Dynamics of Single Conjugated Polymer Chromophores by Surface-Enhanced Raman Spectroscopy. *ACS Nano* **2007**, *1*, 299-306.

(71) Baibarac, M.; Lapkowski, M.; Pron, A.; Lefrant, S.; Baltog, I. SERS Spectra of Poly(3-Hexylthiophene) in Oxidized and Unoxidized States. *J. Raman Spectrosc.* **1998**, *29*, 825-832.

(72) Giorgetti, E.; Margheri, G.; Delrosso, T.; Sottini, S.; Muniz-Miranda, M.; Innocenti, M. A Study of the Degradation of Poly(3-Octylthiophene)-Based Light Emitting Diodes by Surface Enhanced Raman Scattering. *Appl. Phys. B* **2004**, *79*, 603-609.

(73) Kocharova, N.; Lukkari, J.; Viinikanoja, A.; Aaritalo, T.; Kankare, J. Doping-Induced Structural Changes of Conducting Polyalkoxythiophene on the Chemically Modified Gold Surface: An in Situ Surface Enhanced Resonance Raman Spectroscopic Study. *J. Phys. Chem. B* **2002**, *106*, 10973-10981.

(74) Kocharova, N.; Lukkari, J.; Viinikanoja, A.; Aaritalo, T.; Kankare, J. Conformational Changes of a Self-Assembled Polyalkoxythiophene during Electrochemical Doping: An in Situ SERRS Study. *J. Mol. Struct.* **2003**, *651-653*, 75-83.

(75) Baibarac, M.; Mihut, L.; Louarn, G.; Mevellec, J. Y.; Wery, J.; Lefrant, S.; Baltog, I. Interfacial Chemical Effect Evidenced on SERS Spectra of Polyaniline Thin Films Deposited on Rough Metallic Supports. *J. Raman Spectrosc.* **1999**, *30*, 1105-1113.

(76) Casado, J.; Takimiya, K.; Otsubo, T.; Ramírez, F. J.; Quirante, J. J.; Ortiz, R. P.; González, S. R.; Oliva, M. M.; López Navarrete, J. T. Raman Spectroscopy shows Interchain through Space Charge Delocalization in a Mixed Valence Oligothiophene Cation and in its π-Dimeric Biradicaloid Dication. *J. Am. Chem. Soc.* **2008**, *130*, 14028–14029.

(77) Yun, J.; Peet, J.; Cho, N.; Bazan, G. C.; Lee, S. J.; Moskovits, M. Insight into the Raman Shifts and Optical Absorption Changes upon Annealing polymer/fullerene Solar Cells. *Appl. Phys. Lett.* **2008**, *92*, 251912.

(78) Casado, J.; Hernandez, V.; Ruiz Delgado, M. C.; Ortiz, R. P.; Lopez Navarrete, J. T.; Facchetti, A.; Marks, T. J. Incisive Structure-Spectroscopic Correlation in Oligothiophenes Functionalized with (±) inductive/mesomeric Fluorine Groups: Joint Raman and DFT Study. *J. Am. Chem. Soc.* **2005**, *127*, 13364-13372.

(79) Bazzaoui, E. A.; Aubard, J.; Elidrissi, A.; Ramdani, A.; Levi, G. Influence of the Working Electrode Metal on the Polythiophene Structure. Raman and x-Ray

Photoelectron Spectroscopic Investigations of the aluminium/polythiophene Interface. *J. Raman Spectrosc.* **1998**, *29*, 799-805.

(80) Louarn, G.; Buisson, J. P.; Lefrant, S.; Fichou, D. Vibrational Studies of a Series of a-Oligothiophenes as Model Systems of Polythiophene. *J. Phys. Chem.* **1995**, *99*, 11399-11404.

(81) Sauvajol, J. L.; Poussigue, G.; Benoit, C.; Lere-Porte, J. P.; Chorro, C. Sample Dependence of Raman Spectrum on Polythiophene Films. *Synth. Met.* **1991**, *41*, 1237-1242.

(82) Garrell, R. L.; Herne, T. M.; Szafranski, C. A.; Diederich, F.; Ettl, F.; Whetten, R. L. Surface-Enhanced Raman Spectroscopy of C_{60} on Gold: Evidence for Symmetry Reduction and Perturbation of Electronic Structure in the Adsorbed Molecule. *J. Am. Chem. Soc.* **1991**, *113*, 6302-6303.

(83) Kang, M.; Guo, L. J. Nanoimprinted Semitransparent Metal Electrodes and their Application in Organic Light-Emitting Diodes. *Adv. Mater.* **2007**, *19*, 1391-1396.

(84) Elschner, A.; Kirchmeyer, S. PEDOT-type materials in organic solar cell. Brabec, C., Dyakonov, V. and Scherf, U., Eds.; In *Organic Photovoltaics: Materials, Device Physics, and Manufacturing Technologies*; Wiley-VCH: Weinheim, 2008; pp 213-242; 7.

(85) Lee, P. C.; Meisel, D. Adsorption and Surface-Enhanced Raman of Dyes on Silver and Gold Sols. *J. Phys. Chem.* **1982**, *86*, 3391-3395.

(86) Ho, P. K. H.; Kim, J.; Burroughes, J. H.; Becker, H.; Li, S. F. Y.; Brown, T. M.; Cacialli, F.; Friend, R. H. Molecular-Scale Interface Engineering for Polymer Light-Emitting Diodes. *Nature* **2000**, *404*, 481-484.

(87) Shoute, L. C. T.; Bartholomew, G. P.; Bazan, G. C.; Kelley, A. M. Resonance Hyper-Raman Excitation Profiles of a Donor-Acceptor Substituted Distyrylbenzene: One-Photon and Two-Photon States. *J. Chem. Phys.* **2005**, *122*, 184508.

(88) Myers, A. B. Excited electronic state properties from ground-state resonance Raman intensities. Myers, A. B., Rizzo, T. R., Eds.; In *Laser Techniques in Chemistry*; Wiley: New York, **1995**; pp 325-384.

(89) Frisch, M. J., et al Gaussian 03. **2004**, *Rev. C.02*.

(90) Jin, R.; Cao, Y. C.; Hao, E.; Metraux, G. S.; Schatz, G. C.; Mirkin, C. A. Controlling Anisotropic Nanoparticle Growth through Plasmon Excitation. *Nature* **2003**, *425*, 487-490.

(91) Xue, C.; Mirkin, C. A. Ph-Switchable Silver Nanoprism Growth Pathways. *Ang. Chem. Int. Ed.* **2007**, *46*, 2036-2038.

(92) Le Ru, E. C.; Grand, J.; Félidj, N.; Aubard, J.; Lévi, G.; Hohenau, A.; Krenn, J. R.; Blackie, E.; Etchegoin, P. G. Experimental Verification of the SERS Electromagnetic Model Beyond the $|E|^4$ Approximation: Polarization Effects. *J. Phys. Chem. C* **2008**, *112*, 8117-8121.

(93) Groenendaal, L.; Jonas, F.; Freitag, D.; Pielartzik, H.; Reynolds, J. R. Poly(3,4-Ethylenedioxythiophene) and its Derivatives: Past, Present, and Future. *Adv. Mater.* **2000**, *12*, 481-494.

(94) Greczynski, G.; Kugler, T.; Keil, M.; Osikowicz, W.; Fahlman, M.; Salaneck, W. R. Photoelectron Spectroscopy of Thin Films of PEDOT-PSS Conjugated

Polymer Blend: A Mini-Review and Some New Results. *J. Electron Spectrosc. Relat. Phenom.* **2001**, *121*, 1-17.

(95) Lang, U.; Muller, E.; Naujoks, N.; Dual, J. Microscopical Investigations of PEDOT:PSS Thin Films. *Adv. Funct. Mater.* **2009**, *19*, 1215-1220.

(96) Duvail, J. L.; Retho, P.; Garreau, S.; Louarn, G.; Godon, C.; Demoustier-Champagne, S. Transport and Vibrational Properties of Poly(3,4-Ethylenedioxythiophene) Nanofibers. *Synth. Met.* **2002**, *131*, 123-128.

(97) Domagala, W.; Pilawa, B.; Lapkowski, M. Quantitative in-Situ EPR Spectroelectrochemical Studies of Doping Processes in Poly(3,4-Alkylenedioxythiophene)s: Part 1: PEDOT. *Electrochim. Acta* **2008**, *53*, 4580-4590.

(98) Rasmark, P. J.; Andersson M.; Lindgren J.; Elvingson C. Differences in Binding of a Cationic Surfactant to Cross-Linked Sodium Poly(Acrylate) and Sodium Poly(Styrene Sulfonate) Studied by Raman Spectroscopy. *Langmuir* **2005**, *21*, 2761-2765.

(99) Edwards, H. G. M.; Brown, D. R.; Dale, J. R.; Plant, S. Raman Spectroscopic Studies of Acid Dissociation in Sulfonated Polystyrene Resins. *J. Mol. Struct.* **2001**, *595*, 111-125.

(100) Zhang, S. L.; Pezzuti, J. A.; Morris, M. D.; Appadwedula, A.; Hsiung, C.; Leugers, M. A.; Bank, D. Hyperspectral Raman Line Imaging of Syndiotactic Polystyrene Crystallinity. *Appl. Spectrosc.* **1998**, *52*, 1264-1268.

(101) Sears, W. M.; Hunt, J. L.; Stevens, J. R. Raman Scattering from Polymerizing Styrene. I. Vibrational Mode Analysis. *J. Chem. Phys.* **1981**, *75*, 1589-1598.

(102) Garreau, S.; Louarn, G.; Buisson, J. P.; Froyer, G.; Lefrant, S. In Situ Spectroelectrochemical Raman Studies of Poly(3,4-Ethylenedioxythiophene) (PEDT). *Macromolecules* **1999**, *32*, 6807-6812.

(103) Tran-Van, F.; Garreau, S.; Louarn, G.; Froyer, G.; Chevrot, C. A Fully Undoped Oligo(3,4-Ethylenedioxythiophene): Spectroscopic Properties. *Synth. Met.* **2001**, *119*, 381-382.

(104) Dkhissi, A.; Louwet, F.; Groenendaal, L.; Beljonne, D.; Lazzaroni, R.; Bredas, J. L. Theoretical Investigation of the Nature of the Ground State in the Low-Bandgap Conjugated Polymer, Poly(3,4-Ethylenedioxythiophene). *Chem. Phys. Lett.* **2002**, *359*, 466-472.

(105) Chiu, W. W.; Travas-Sejdic, J.; Cooney, R. P.; Bowmaker, G. A. Studies of Dopant Effects in Poly(3,4-Ethylenedioxythiophene) using Raman Spectroscopy. *J. Raman Spectrosc.* **2006**, *37*, 1354-1361.

(106) Kim, J. -.; Ho, P. K. H.; Murphy, C. E.; Baynes, N.; Friend, R. H. Nature of Non-Emissive Black Spots in Polymer Light-Emitting Diodes by in-Situ Micro-Raman Spectroscopy. *Adv. Mater.* **2002**, *14*, 206-209.

(107) Schaarschmidt A.; Farah A. A.; Aby A.; Helmy A. S. Influence of Nonadiabatic Annealing on the Morphology and Molecular Structure of PEDOT-PSS Films. *J Phys Chem B* **2009**, *113*, 9352-9355.

(108) Crispin, X.; Marciniak, S.; Osikowicz, W.; Zotti, G.; Van der Gon, A. W. D.; Louwet, F.; Fahlman, M.; Groenendaal, L.; De Schryver, F.; Salaneck, W. R. Conductivity, Morphology, Interfacial Chemistry, and Stability of Poly(3,4-

Ethylene Dioxythiophene)-Poly(Styrene Sulfonate): A Photoelectron Spectroscopy Study. *J. Pol. Sci. B: Pol. Phys.* **2003**, *41*, 2561-2583.

(109) Jonsson, S. K. M.; Birgerson, J.; Crispin, X.; Greczynski, G.; Osikowicz, W.; Denier van der Gon, A. W.; Salaneck, W. R.; Fahlman, M. The Effects of Solvents on the Morphology and Sheet Resistance in Poly(3,4-Ethylenedioxythiophene)–polystyrenesulfonic Acid (PEDOT–PSS) Films. *Synth. Met.* **2003**, *139*.

(110) Sakamoto, S.; Okumura, M.; Zhao, Z.; Furukawa, Y. Raman Spectral Changes of PEDOT-PSS in Polymer Light-Emitting Diodes upon Operation. *Chem. Phys. Lett.* **2005**, *412*, 395-398.

(111) Marciniak, S.; Crispin, X.; Uvdal, K.; Trzcinski, M.; Birgerson, J.; Groenendaal, L.; Louwet, F.; Salaneck, W. R. Light Induced Damage in Poly(3,4-Ethylenedioxythiophene) and its Derivatives Studied by Photoelectron Spectroscopy. *Synth. Met.* **2004**, *141*, 67-73.

(112) Manceau, M.; Rivaton, A.; Gardette, J.; Guillerez, S.; Lemaitre, N. The Mechanism of Photo- and Thermooxidation of Poly(3-Hexylthiophene) (P3HT) Reconsidered. *Polymer Degradation and Stability* **2009**, *94*, 898-907.

(113) Abdou, M. S. A.; Holdcroft, S. Solid-State Photochemistry of p-Conjugated Poly(3-Alkylthiophenes). *Can. J. Chem.* **1995**, *73*, 1893-1901.

(114) Leng, W.; Woo, H. Y.; Vak, D.; Bazan, G. C.; Kelley, A. M. Surface-Enhanced Resonance Raman and Hyper-Raman Spectroscopy of Water-Soluble Substituted Stilbene and Distyrylbenzene Chromophores. *J. Raman Spectrosc.* **2006**, *37*, 132-141.

(115) Itoh, K.; Kudryashov, I.; Yamagata, J.; Nishizawa, T.; Fujii, M.; Osaka, N. Raman Microspectroscopic Study on Polymerization and Degradation Processes of a Diacetylene Derivative at Surface Enhanced Raman Scattering Active Substrates. 2. Confocal Raman Microscopic Observation of Polydiacetylene Adsorbed on Active Sites. *J. Phys. Chem. B.* **2005**, *109*, 271-276.

(116) Pieczonka, N. P. W.; Aroca, R. F. Inherent Complexities of Trace Detection by Surface-Enhanced Raman Scattering. *ChemPhysChem* **2005**, *6*, 2473-2484.

(117) Domke, K. F.; Zhang, D.; Pettinger, B. Enhanced Raman Spectroscopy: Single Molecules Or Carbon? *J. Phys. Chem. C* **2007**, *111*, 8611-8616.

(118) Yeo, B.; Schmid, T.; Zhang, W.; Zenobi, R. A Strategy to Prevent Signal Losses, Analyte Decomposition, and Fluctuating Carbon Contamination Bands in Surface-Enhanced Raman Spectroscopy. *Appl. Spectrosc.* **2008**, *62*, 708-713.

(119) Casado, J.; Zotti, G.; Berlin, A.; Hernández, V.; Ortiz, R. P.; López Navarrete, J. T. Combined Theoretical and Spectroscopic Raman Study of 3,4-Ethylenedioxy and S,S-Dioxide Substituted Terthiophenes and their Parent Polymers. *J. Mol. Struct.* **2005**, *744-747*, 551-556.

(120) Knopf; D. A.; Luo; B. P.; Krieger; U. K.; Koop; T. Thermodynamic Dissociation Constant of the Bisulfate Ion from Raman and Ion Interaction Modeling Studies of Aqueous Sulfuric Acid at Low Temperatures. *J. Phys. Chem. A* **2003**, *107*, 4322.

(121) Stavytska-Barba M.; Kelley A.M.; Salvador M.; Kulkarni A.; Ginger D.S. Plasmonic Enhancement of Raman Scattering from the Organic Solar Cell

Material P3HT/PCBM by Triangular Silver Nanoprisms. *J. Phys. Chem. C* **2011**, *115*, 20788-20794.

(122) Willets, K. A.; Van Duyne, R. P. Localized Surface Plasmon Resonance Spectroscopy and Sensing. *Ann. Rev. Phys. Chem.* **2007**, *58*, 267-297.

(123) Knobloch, H.; Brunner, H.; Leitner, A.; Aussenegg, F.; Knoll, W. Probing the Evanescent Field of Propagating Plasmon Surface Polaritons by Fluorescence and Raman Spectroscopies. *J. Chem. Phys.* **1993**, *98*, 10093-10095.

(124) Anger, P.; Bharadwaj, P.; Novotny, L. Enhancement and Quenching of Single-Molecule Fluorescence. *Phys. Rev. Lett.* **2006**, *96*, 113002.

(125) Tam, F.; Goodrich, G. P.; Johnson, B. R.; Halas, N. J. Plasmonic Enhancement of Molecular Fluorescence. *Nano Lett.* **2007**, *7*, 496-501.

(126) Galloway, C. M.; Etchegoin, P. G.; Le Ru, E. C. Ultrafast Nonradiative Decay Rates on Metallic Surfaces by Comparing Surface-Enhanced Raman and Fluorescence Signals of Single Molecules. *Phys. Rev. Lett*. **2009**, *103*, 063003.

(127) Johansson, P.; Xu, H.; Käll, M. Surface-Enhanced Raman Scattering and Fluorescence Near Metal Nanoparticles. *Phys. Rev. B* **2005**, *72*, 035427.

 (128) Guo, J.; Ohkita, H.; Benten, H.; Ito, S. Charge Generation and Recombination Dynamics in Poly(3-Hexylthiophene)/fullerene Blend Films with Different Regioregularities and Morphologies. *J. Am. Chem. Soc*. **2010**, *132*, 6154-6164.

(129) Piris, J.; Dykstra, T. E.; Bakulin, A. A.; van Loosdrecht, P. H. M.; Knulst, W.; Trinh, M. T.; Schins, J. M.; Siebbeles, L. D. A. Photogeneration and Ultrafast Dynamics of Excitons and Charges in P3HT/PCBM Blends. *J. Phys. Chem. C* **2009**, *113*, 14500-14506.